SIMULATION OF BRITTLE ROCK FAILURE USING 2D CONTINUUM-BASED VORONOI TESSELLATED MODELS

by

Soheil Sanipour

Submitted in partial fulfilment of the requirements
for the degree of Master of Applied Science

at

Dalhousie University
Halifax, Nova Scotia

TABLE OF CONTENTS

LIST OF TABLES

LIST OF FIGURES

viii

ABSTRACT

Micro-structural heterogeneities of brittle rocks govern their failure process, which involves crack initiation and propagation before the peak stress is reached. Voronoi tessellation is an approach, commonly used in discontinuum numerical programs to simulate brittle rocks by dividing the numerical specimen into several randomly generated polygonal blocks. In this study, a 2D Voronoi Tessellated Model (VTM) is developed in a continuum program to simulate the behavior of Lac du Bonnet (LdB) granite. The VTM is first calibrated to the laboratory properties of LdB granite. The calibrated VTM captures the damage evolution and failure mode transition from axial splitting to shear failure with increasing confinement. Next, v-shaped notch failure around a circular test tunnel is simulated by the VTM calibrated to the rock mass strength estimated based on the s-shaped failure criterion. It is concluded that the calibrated VTM realistically simulates the observed failure and damage zones around the tunnel.

LIST OF ABBREVIATIONS AND SYMBOLS

2D	Two Dimensional
3D	Three Dimensional
BTS	Brazilian Tensile Strength
CBF	Cohesive Brittle Frictional
CDZ	Construction Damage Zone
CS	Core Softening
CWFS	Cohesion Weakening Frictional Strengthening
DDA	Discontinuous Deformation Analysis
DEM	Distinct Element Method
DFN	Discrete Fracture Network
DGR	Deep Geological Repository
DISL	Damage Initiation Spalling Limit
DoF	Depth of Failure
DTS	Direct Tensile Strength
EDZ	Excavation Damage Zone
EIZ	Excavation Influence Zone
ESS	Excavation Stability Study
FDEM	Finite Discrete Element Method
FDM	Finite Difference Method
FEM	Finite Element Method
FS	Factor of Safety
GBM	Grain-Based Model
GSI	Geological Strength Index
HB	Hoek-Brown
HDZ	Highly Damage Zone
LdB	Lac du Bonnet
MBE	Mine-By Experiment
PFC	Particle Flow Code

SoF	Shape of Failure
UCS	Uniaxial Compressive Strength
UDEC	Universal Distinct Element Code
URL	Underground Research Laboratory
VTM	Voronoi Tessellated Model
c	Cohesion
c_{pb}	Peak block cohesion
c_{pbb}	Peak block boundary cohesion
c_{rb}	Residual block cohesion
c_{rbb}	Residual block boundary cohesion
D	Disturbance factor
E	Young's modulus
E_{rm}	Young's modulus of rock mass
k_n	Normal stiffness
k_s	Shear stiffness
a	Hoek-Brown parameter
m_b	Hoek-Brown parameter
m_i	Hoek-Brown parameter
s	Hoek-Brown parameter
υ	Poisson's ratio
σ_1	Major principal stress
σ_1'	Effective major principal stress
σ_3	Minor principal stress
σ_3'	Effective minor principal stress
σ_{cd}	Crack damage
σ_{ci}	Crack initiation
σ_{max}	Maximum tangential stress
σ_t	Tensile strength
σ_{tpb}	Peak block tensile strength
σ_{tpbb}	Peak block boundary tensile strength

σ_{trb}	Residual block tensile strength
σ_{trbb}	Residual block boundary tensile strength
ϕ	Friction angle
ϕ_{pb}	Peak block friction angle
ϕ_{pbb}	Peak block boundary friction angle
ϕ_{rb}	Residual block friction angle
ϕ_{rbbb}	Residual block boundary friction angle
ω	Normalized damage

ACKNOWLEDGMENTS

I would like to express my sincerest gratitude to my supervisors Dr. Navid Bahrani and Dr. Andrew Corkum, without whom, this work could have never been completed. I was fortunate enough to work under their supervision and learn from them in many aspects beyond numerical modeling and rock mechanics throughout this path. Their skillful guidance, aid, and constructive feedback toward the completion of my thesis will always be appreciated.

A special thanks to Dr. Navid Bahrani as a friend, who trusted me and provided this wonderful opportunity to start learning from him as early as several months before the official starting date of my MASc studies.

Another special thanks to Dr. Andrew Corkum as a mentor, who has shown me the importance of finding the limitations and potential applicability of numerical modeling, and above all, seeking the right answers for the right reasons.

I would like to thank the committee members Dr. Hany El Naggar and Dr. Dmitry Garagash for reviewing my research, attending my defence session and their technical advice.

I am grateful for my friends who stood beside me during two memorable years of my graduate studies. I also wish to acknowledge my friends and colleagues at Dalhousie University for their assistant in this period.

Finally, I would like to thank my parents whose continuous support, presence, and encouragement were great driving forces in the completion of my research.

Chapter 1 Introduction

1.1   Overview

Demand for global supply of minerals and energy resources dictates the development of underground excavations at great depths. There are various geomechanical challenges associated with deep underground excavations arising from complex and sometimes unexpected rock behavior due to high in situ stress conditions. Reliable designs of such excavations require detailed knowledge of in situ and induced stresses, progressive fracturing processes, strength and failure mechanism of rock mass surrounding these openings. A Deep Geological Repository (DGR), which consists of a network of tunnels constructed at a depth of several hundred meters below the ground surface, is an example of such excavations.

Excavation of an underground opening results in redistribution of stresses in the vicinity of the excavation boundary. In hard brittle rocks, failure occurs due to initiation, accumulation and propagation of damage resulting in spalling and slabbing of rock mass near the excavation boundary, which may evolve to form a v-shaped notch. Figure 1-1 shows an example of a v-shaped notch failure around a test tunnel constructed at 420 m Level of the Underground Research Laboratory (URL) in Manitoba, Canada.

Figure 1-1 An example of v-shaped notch failure around a circular test tunnel at the URL (after Read et al., 1998)

In permeability sensitive excavations such as DGRs, Depth of Failure (DoF) and extent of Excavation Damage Zone (EDZ) are two important design parameters. Additionally, Shape of Failure (SoF) provides useful information about the concentration of damage and failure around the excavation. These parameters are required for the design of excavation geometry, the long-term stability and post-closure safety of DGRs.

Two common approaches used to estimate the DoF in hard brittle rocks are empirical and numerical methods. Empirical methods provide a general guide in preliminary design stages of underground excavations. The relationship between the DoF and the maximum tangential stress at the excavation boundary proposed by Martin et al. (1999) is a well-known example of empirical methods used to predict the DoF around circular excavations in hard brittle rocks. This empirical method was developed based on several case studies and do not provide sufficient insights into the failure mechanism, EDZ and SoF around underground openings. Therefore, a robust design of DGRs should not be solely based on this approach.

Numerical modeling has been widely used in the past few decades for stability analysis and design of DGRs. In this research, a numerical modeling approach using a commercial software program based on the Finite Element Method (FEM) is proposed to capture all three design criteria (i.e., DoF, SoF and EDZ) around the URL's test tunnel shown in Figure 1-1.

1.2 Problem Statement

Numerical modeling is an important tool that is used to solve a wide range of rock engineering problems. Numerical methods used in geomechanics are typically classified into three broad categories: continuum, discontinuum and hybrid continuum-discontinuum (Li et al., 2019). The FEM and the Finite Difference Method (FDM) are two examples of continuum methods commonly used in rock engineering. Examples of discontinuum and hybrid continuum-discontinuum methods include the Distinct Element Method (DEM) and the hybrid Finite-Discrete Element Method (FDEM), respectively.

Two common constitutive laws used in conventional continuum methods to simulate the failure of hard brittle rocks around underground excavations are: Cohesion Weakening Frictional Strengthening (CWFS) (Hajiabdolmajid et al., 2002) and Damage Initiation and Spalling Limit (DISL) (Diederichs, 2003). These models have been demonstrated to be capable of simulating the DoF and SoF. However, the formation and emergent characteristics of the EDZ are not properly captured by these models. Furthermore, the simulated mode of failure is shear, which is not consistent with the failure mode of brittle rocks at low confinement observed in the laboratory (e.g., unconfined compression test) and field (e.g., failure around tunnels), which is usually associated with tensile mechanisms.

Discontinuum methods typically provide a better representation of the progressive failure process of brittle rocks compared to continuum methods. The DoF, EDZ and SoF with realistic failure modes have been captured using discontinuum methods (e.g., Potyondy & Cundall, 2004; Hazzard & Young, 2004; Vazaios et al., 2019). Nonetheless, the disadvantage of discontinuum methods is their high computational costs due in large part to the lack of reliable input parameters and complexity of model calibration. For these reasons, the discontinuum methods do not often meet practical requirements for conventional engineering analyses (Bahrani and Hadjigeorgiou, 2018).

It is generally known that heterogeneity in rock fabric results in the inducement of localized tensile stresses inside a specimen even under an overall compressive loading condition. At low confinement, such as the vicinity of underground openings, tensile damage occurs when the tensile stress exceeds the local tensile strength of the rock. In conventional continuum models, the rock is simulated as a homogeneous medium, and therefore the simulated failure mechanism of hard brittle rocks is often shear as the stresses are uniformly distributed throughout the numerical model. Therefore, in order to realistically simulate the brittle failure process, micro-structural heterogeneities need to be considered in the simulations. Preliminary investigations by Valley et al. (2009), Bewick et al. (2010) and Li and Bahrani (2021a and b) have demonstrated promising results in capturing the brittle rock failure process when heterogeneities are included in

continuum models. In this research, a two-dimensional (2D) heterogeneous continuum model is developed to simulate the failure process of hard brittle rocks under laboratory and field loading conditions.

1.3   Objectives

The central objective of this research is to simulate the progressive failure of hard brittle rocks using RS2, which is a 2D finite element program developed by Rocscience Inc. For this purpose, heterogeneous models are developed to replicate the laboratory and field-scale behavior of LdB granite. The detailed objectives of this research include:

- Capturing the failure mode of LdB granite observed in laboratory tests including the Brazilian Tensile Strength (BTS), Direct Tensile Strength (DTS), Uniaxial Compressive Strength (UCS) and confined compression tests.
- Developing a systematic procedure to calibrate the models to the laboratory and in situ strength of LdB granite.
- Simulating the DoF, EDZ and SoF with realistic failure modes around the URL's circular test tunnel shown in Figure 1-1 using the calibrated models.

1.4   Methodology

A Voronoi Tessellated Model (VTM) is an advanced modeling approach typically used in discontinuum numerical programs to simulate the heterogeneous nature of rocks (e.g., Lan et al., 2010; Bahrani et al., 2014; Ghazvinian et al., 2014). A VTM consists of several randomly generated polygonal blocks that are bonded together at their boundaries. This approach has been widely used by various researchers to simulate various types of rock heterogeneities at different scales. For example, at the laboratory scale, blocks and block boundaries can be used to simulate grains and grain boundaries (Li and Bahrani, 2021a), while at the rock mass scale, they could represent rock blocks and joints, respectively (Li and Bahrani, 2021b).

In this study, a 2D continuum-based VTM is developed to simulate the standard rock mechanics laboratory tests. The step before simulating large scale applications (i.e.,

tunnel) is to calibrate the VTM to a representative strength envelope for the rock. Typically, micro-mechanical modeling of intact rock is conducted using models calibrated to laboratory test results. The calibrated model is then upscaled and applied to excavation conditions with the objective that failure will be an emergent response of the micro-mechanical model (Dadashzadeh, 2020; Li and Bahrani, 2021b). In this study, the continuum-based micro-mechanical model is calibrated to failure envelopes derived specifically to capture brittle failure around excavations. Three strength envelopes are considered for this purpose: 1) laboratory peak strength of intact rock; 2) equivalent Hoek-Brown rock mass strength envelope; and 3) tri-linear (s-shaped) rock mass strength envelope.

First, the intact rock strength envelope obtained from laboratory tests is used for the model calibration. This is based on field observations at the URL that the rock mass is devoid of any strength dominating discontinuities and thus, the rock mass strength is assumed to be equal to the intact rock strength. The two other strength criteria investigated in this research are the tri-linear and its corresponding equivalent Hoek-Brown rock mass strength envelopes proposed by Bewick et al. (2019). The tri-linear criterion is fundamentally based on the s-shaped failure criterion developed for massive to moderately jointed rock masses by Diederichs (1999; 2003). The main assumption in these two criteria is that the rock mass strength under an unconfined condition is equal to the crack initiation threshold of intact rock obtained from laboratory uniaxial compression tests. Once the VTM is calibrated to the target strength envelopes mentioned above, it will be used to identify the most appropriate strength envelope that can capture all three design criteria, including the DoF, EDZ and SoF by simulating the URL test tunnel.

The advantage of the proposed continuum- over discontinuum-based VTMs (e.g., UDEC by Itasca Consulting Group Inc.) is its shorter computation time. Its advantage over other continuum modeling approaches, such as the CWFS and DISL models, is that it captures not only the DoF and SoF, but also the EDZ with realistic failure modes (i.e., tensile failure at low confinement and shear failure at high confinement). The contribution of this

research is the development of a modeling approach using an industry-standard software program based on the FEM, which can be used to design underground excavations in hard brittle rocks. It is expected that the outcome of this research will be beneficial for the designs of DGRs, deep underground mines and civil tunnels especially subjected to high stress conditions. Furthermore, it offers a potential tool for the back analysis of in situ stress magnitudes from the depth and shape of breakouts in deep boreholes.

1.5   Thesis Outline

The results of this research are described in five chapters:

The first chapter provides an overview of the research, problem statement and objectives in addition to the research methodology.

The second chapter presents a comprehensive literature review of Canada's URL. This is followed by reviewing previous attempts to simulate the failure around the URL test tunnel using continuum, discontinuum, and hybrid continuum-discontinuum methods.

In Chapter 3, a VTM is developed in the 2D FEM program RS2. Using this model, laboratory tests such as the BTS, DTS, UCS and confined compression tests are simulated. The model is first calibrated to the intact rock properties, and then used to simulate the URL test tunnel.

In Chapter 4, the results of numerical simulations of the URL test tunnel using the VTM calibrated to the rock mass strength envelopes are presented. To this end, the tri-linear and its corresponding equivalent Hoek-Brown rock mass strength envelopes are used as the target for model calibration.

Chapter 5 provides a summary of the results of this study, the major findings of this research in addition to recommendations for future work are also presented in this chapter.

Chapter 2 Literature Review

2.1   Introduction

The prediction of excavation-induced damage zone and failure around underground openings is one of the main concerns in safe and reliable design of underground excavations. Hence, a comprehensive design layout must provide sufficient information about the extent of EDZ and predict the DoF and SoF with realistic failure modes around an underground opening.

This chapter provides an overview of the URL located in Manitoba, Canada. The focus is on the well-known Mine-by Experiment (MBE) tunnel constructed at the URL to investigate the characteristics of the excavation-induced damage zone. The concentration of this chapter is to review pertinent literature, especially the previous numerical simulations of the MBE tunnel and the v-shaped notch failure that occurred around it.

2.2   Canada's Underground Research Laboratory (URL)

The URL was constructed within Lac du Bonnet (LdB) granite batholite, typical of the Canadian Shield, as a potential host rock for long-term waste disposal. The URL is located approximately 120 km northeast of Winnipeg, Manitoba, near the western edge of the Canadian Shield (Read and Martin, 1996).

According to Read and Martin (1991), amongst various experiments conducted at the URL, the MBE was focused on providing information on rock mass response due to excavation. The MBE consisted of three phases (Martin et al., 1997): 1) the excavation response; 2) the permeability studies; and 3) the thermally-induced failure. The first phase was to study the EDZ, which is defined as the damage zone around an opening as a result of stress redistribution. Tsang et al. (2005) defined EDZ as a region with hydromechanical and geochemical modifications, with no significant changes in flow and transport properties. The main excavations at the URL were on 240 m and 420 m Levels, as demonstrated in Figure 2-1.
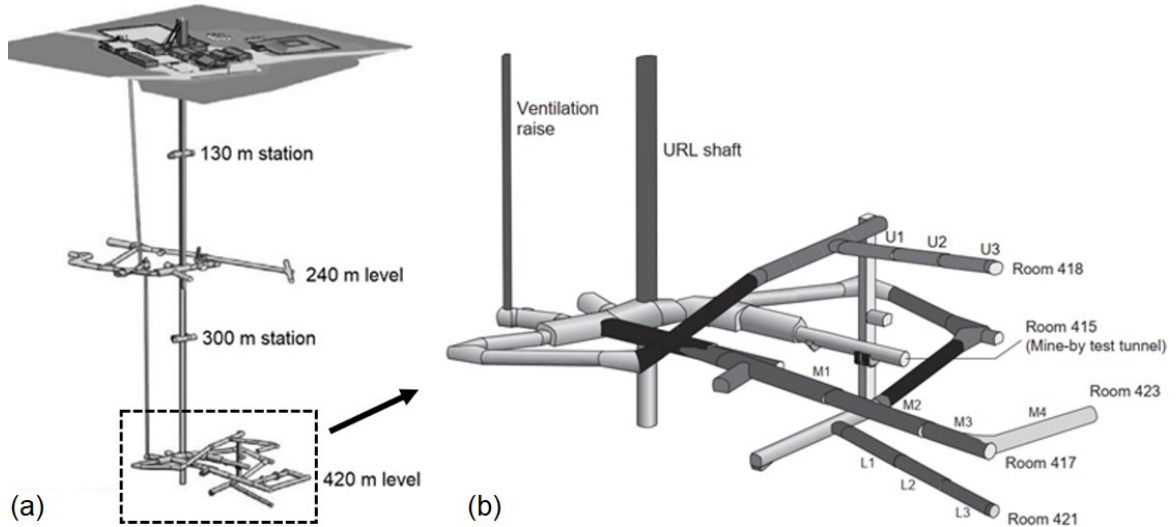
Figure 2-1 a) General layout of URL; b) 420 m Level excavations (after Chandler, 2003, and Read, 2004)

The excavation response phase of the MBE carried out at the 420 m Level of the URL (Figure 1b), was a 46 m long, 3.5 m diameter circular test tunnel. Using non-explosive excavation techniques, the target was to investigate of the progressive brittle failure regardless of the influence of the excavation method. A summary of the research conducted at the URL can be found in Chandler (2003).

2.3   Geotechnical Characterization at URL

2.3.1   Geology

According to Martin (1990), LdB granite is considered to be representative of many granite intrusions of the Precambrian Canadian Shield. Figure 2-2 illustrates the generalized geology of the URL; it can be observed that the host rock at the URL is a mixture of pink and grey porphyritic granite-granodiorite. The composition and texture of the massive, medium- to coarse-grained porphyritic granite is relatively uniform. Figure 2-2 shows the URL shaft intersected by two major thrust faults dipping from 25° to 30° southeast. The faults are referred to as Fracture Zone 3 and Fracture Zone 2.
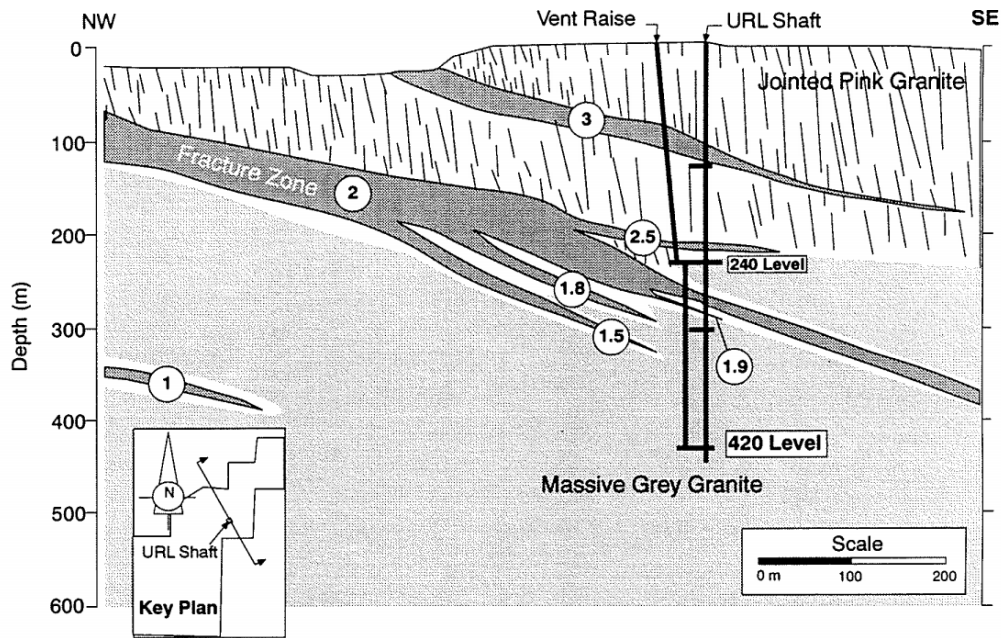
Figure 2-2 Generalized geology of URL (Martin, 1993)

The geological characterization of the URL based on extensive core-logging, geological mapping of surface and subsurface exposures shows that subvertical jointing stops at a depth of 220 m from the ground surface (Read & Martin, 1991; Martin et al., 1997). As shown in Figure 2-2, the rock mass below this depth is relatively massive, except for the illustrated fracture zones. A comprehensive report on the geology of LdB batholite within the URL can be found in Everitt et al. (1996) and Everitt and Lajtai (2004).

2.3.2   In Situ Stresses

The initial estimation of far-field in situ stresses at the URL was reported by Martin (1990) based on an extensive program conducted at this site. The program consisted of overcoring methods, i.e., USBM and CSIRO, hydraulic fracturing, convergence measurements, micro-seismic analyses, core disking and field observations. The in situ stresses at the 420 m and 240 m Levels at the URL are summarized in Table 2-1.

Table 2-1 In situ stresses at 420 m and 240 m Levels of URL (after Martin et al., 1997, after Martino & Chandler, 2004)

Excavation levels	σ_1	σ_2	σ_3
420 m Level			
Magnitudes (MPa)	60 ± 3	45 ± 4	11 ± 4
Trend/Plunge (°)	145/11	054/08	290/77
240 m Level			
Magnitudes (MPa)	26	16	12
Trend/Plunge (°)	228/8	135/28	335/65

2.3.3 Geotechnical Properties of Lac du Bonnet (LdB) Granite

Geotechnical properties of the pink and grey LdB granite are summarized in Table 2-2. The slight difference between the strength and stiffness properties of the pair is due to the presence of microcracks in the samples. As can be seen in Table 2-2, the pink granite has higher strength and elastic modulus in comparison to the grey granite.

Table 2-2 Summary of laboratory geotechnical properties of LdB granite (After Martin, 1990)

Parameters	Unit	Pink granite	Grey granite
Porosity			
Range (mean)	%	0.16 - 0.28 (0.24)	0.32 - 0.67 (0.5)
Density			
Mean	Mg/m^3	2.64	2.63
Uniaxial compressive strength			
Range (mean)	MPa	134 – 248 (200)	147 – 198 (167)
Brazilian tensile strength			
Range (mean)	MPa	6.17 - 12.07 (9.32)	6.22 - 11.52 (8.72)
Tangent Young's modulus			
Range (mean)	GPa	53 – 86 (69)	46 – 64 (55)
Poisson's ratio			
Range (mean)	-	0.18 - 0.44 (0.26)	0.13 - 0.43 (0.30)
Hoek-Brown parameters			
m	-	31.17	30.54
s	-	1	1

The results of laboratory tests on LdB granite along with the Hoek-Brown envelopes for the peak and long-term (crack damage) strengths are plotted in Figure 2-3a. This figure also includes the crack initiation threshold obtained from micro-seismic events monitored around the MBE tunnel and laboratory tests. The stress-strain curves obtained from the

UCS and confined compression tests are illustrated in Figure 2-3b. According to Martin (1997), the significant stress drops in the post-peak measured for LdB granite are associated with macro-scale failure of the specimens.
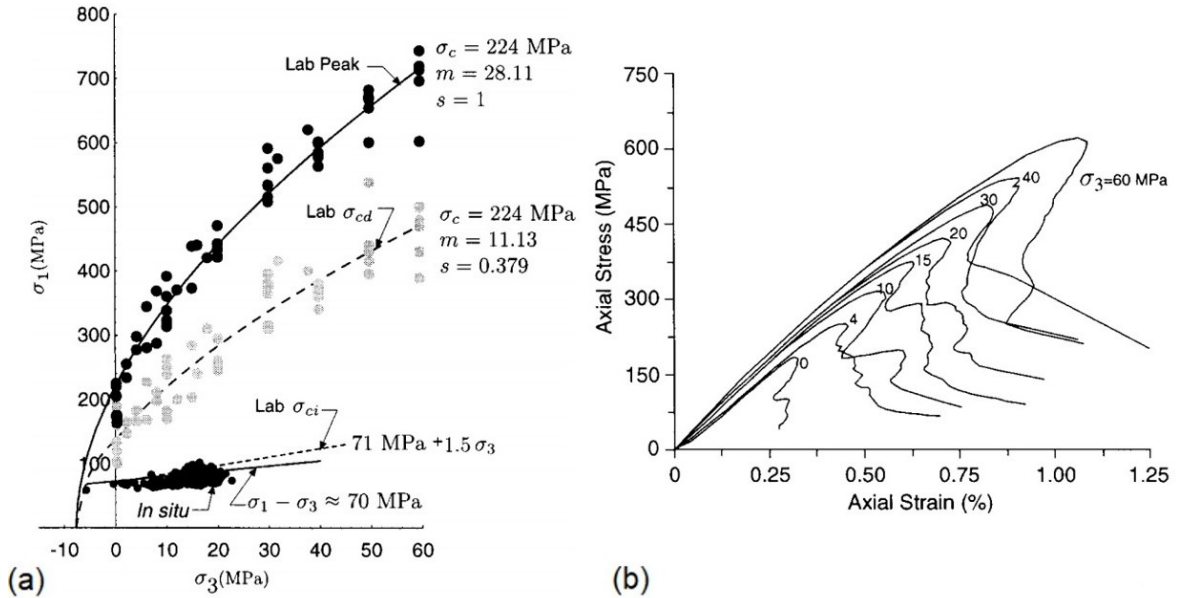
Figure 2-3 a) Hoek-Brown failure envelopes for intact rock and long-term strengths, and crack initiation threshold; b) stress-strain curves of LdB granite (Martin, 1997)

According to Martin and Chandler (1994), the stress-strain curve of a brittle rock can be divided into five regions: 1) crack closure; 2) elastic region; 3) stable crack growth; 4) unstable crack growth (crack damage, σ_{cd}); and 5) peak and post-peak. Read and Martin (1996) explained that the beginning of region 3 marks the onset of stable crack growth or dilation and usually occurs at about 30% to 50% of the peak stress. The crack damage occurrence is related to the reversal of the volumetric strain, thereafter, unstable cracks begin to grow. Based on Martin and Chandler (1994), the crack initiation threshold and σ_{cd} are true material parameters regardless of sample volume. The identification of the pair is studied by Martin and Chandler (1994), Eberhardt et al. (1997), and Martin (1997). Conversely, the peak stress, which is the onset of the post-peak region, is known to be a function of loading conditions and sample size.
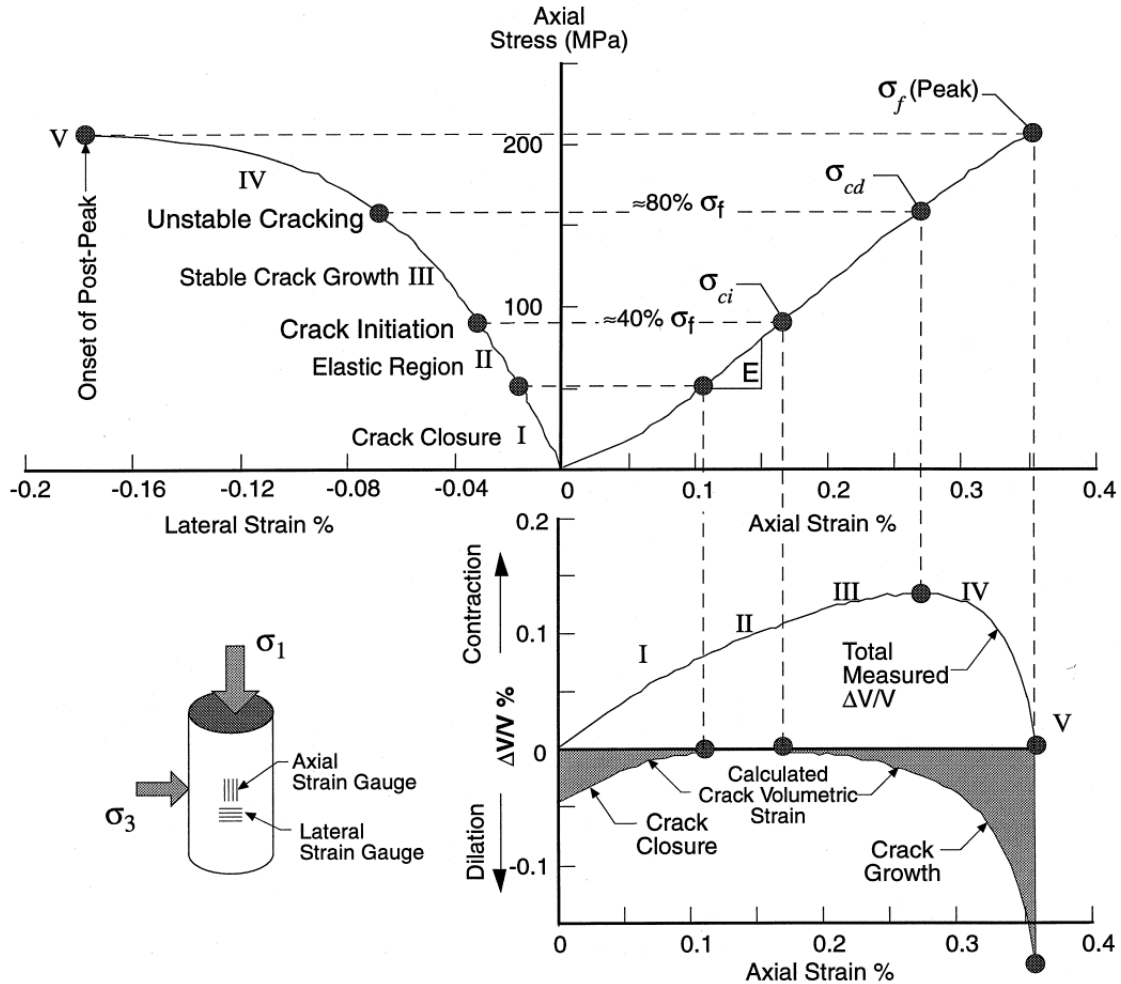
Figure 2-4 Stress-strain curves for a single UCS test of LdB granite showing: crack closure, elastic region, stable crack growth, unstable cracking, peak stress, and post-peak region (Martin, 1993)

The strength of intact rock is directly related to intrinsic cohesion and frictional strength components. Damage testing of LdB granite by Martin and Chandler (1994) showed that the assumption of considering cohesion and friction angle being mobilized at the same strain cannot realistically describe the behavior of the intact rock subjected to stresses. This study stated that the progression of fracturing in LdB granite is due to non-simultaneous loss of cohesion and mobilization of friction. Figure 2-5 illustrates the cohesion-loss and friction mobilization as a function of normalized damage (ω). It should be noted that the damage parameter is defined as the permanent volumetric strain resulting from a single damage increment.
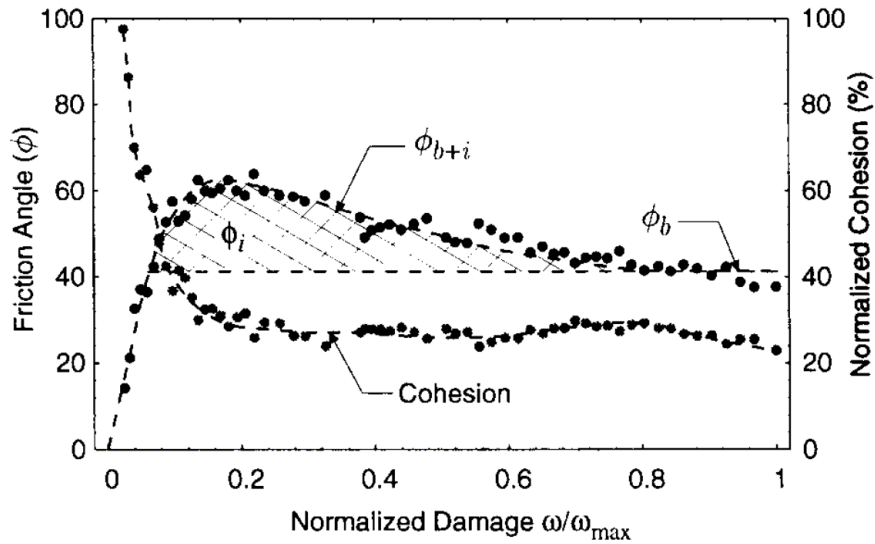
Figure 2-5 Mobilization of cohesion and friction as functions of damage (after Martin and Chandler, 1994)

2.4 Characterization of Excavation Damage Zone at URL

In order to investigate the formation, characteristics and extent of the EDZ, various excavation response studies were conducted at the URL. The experiments were focused mainly on the URL shaft and the 240 m Level in moderately to sparsely fractured rock within moderate in situ stresses, in addition to in situ experiments carried out in the 420-m Level.

According to Read (2004), the objectives of these investigations were to: 1) achieve fundamental understanding of rock mass behavior around underground spaces; 2) develop proper engineering tools to characterize rock mass behavior subjected to different in situ conditions; 3) propose a suitable design approach that combines characterization, monitoring and numerical modeling to predict rock mass behavior in both short- and long-term periods; and 4) provide data useful for designing repositories in deep geological environments (Martino & Chandler, 2004). The following sections in this chapter are focused on Room 415. Furthermore, comprehensive reports on the URL shaft and 240 m Level experiments can be found in Read (2004) and Martino and Chandler (2004).

2.4.1 Mine-By Experiment (MBE) Tunnel (Room 415)

To investigate the excavation-induced rock mass response, a 3.5 m circular test tunnel was excavated using a non-explosive technique (Read & Martin, 1996). The layout of the MBE including the type of instrumentations at the 420 m Level of the URL is illustrated in Figure 2-6. The main focus of this experiment was to delve into the mechanism of progressive failure, the development of excavation-induced damage and to explore the formation and characteristics of the disturbed zone around an underground opening in crystalline rocks (Read & Martin, 1996; Martin et al., 1997).
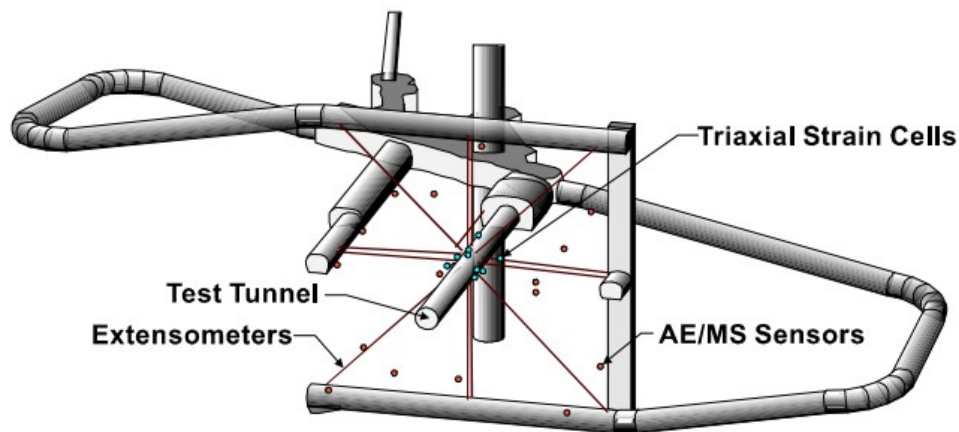
Figure 2-6 Layout of MBE tunnel at 420 m Level of URL (Read, 2004)

2.4.1.1 Excavation Method

According to Read and Martin (1996), based on previous experience in Room 209 and the URL shaft, the disturbed zone near the boundary of openings was a function of both stress redistribution and blast effects. In order to minimize the effect of blast damage, a combination of drill-and-blast near Room 414 at the beginning of the MBE tunnel and line drilling with mechanical breakage using hydraulic splitters (Figure 2-7a) was used (Read & Martin, 1991). The excavation was modified to pilot-and-slash technique to investigate the influence of sequential excavation (Martin et al., 1997). Figure 2-7b demonstrates a schematic longitudinal section of the MBE tunnel indicating the excavation method and sequences for various sections.
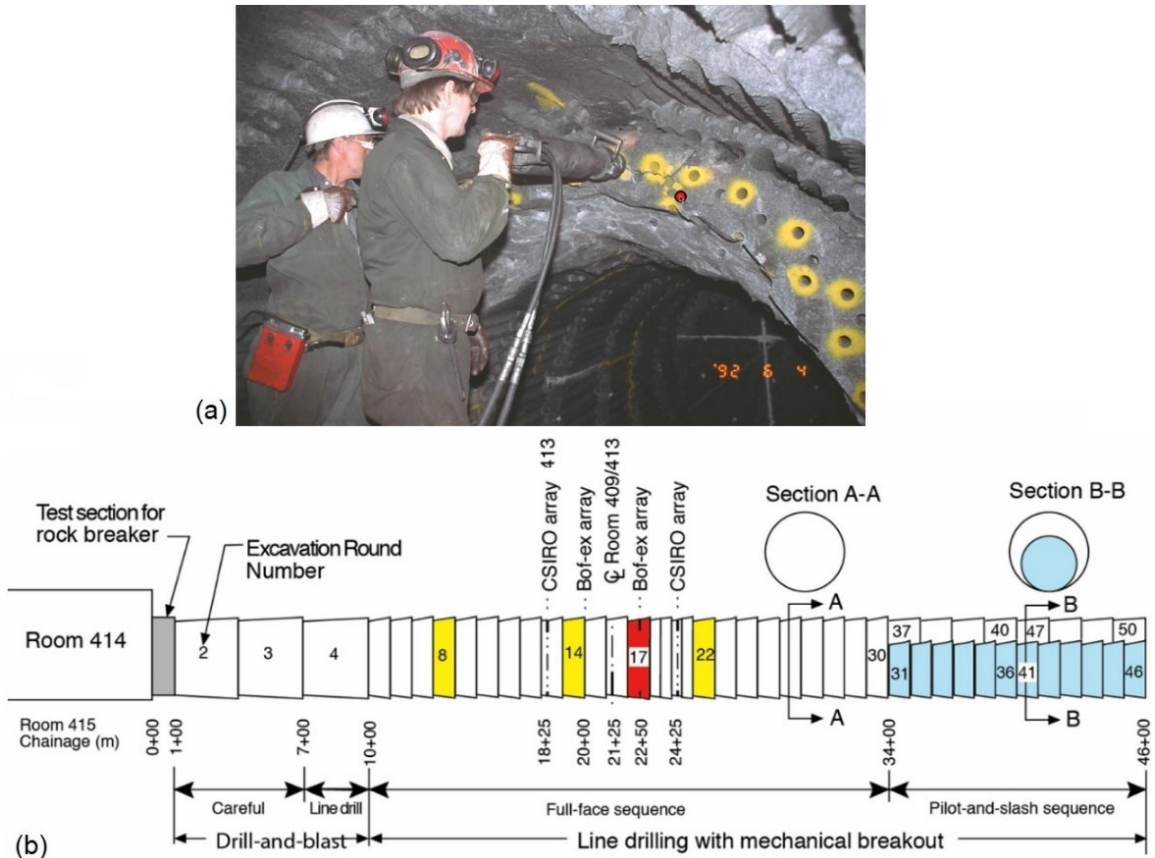
Figure 2-7 a) Excavation by line-drilling method (Ghazvinian, 2015), b) excavation methods and sequences along MBE tunnel (after Martin et al., 1997)

2.4.1.2 Observation of Brittle Failure

In hard brittle rocks subjected to high in situ stresses, failure occurs when the rock mass strength is exceeded by the induced stresses. The excavation of an underground opening reduces confinement from its initial value to zero at the boundary and increases the tangential stresses at certain locations depending on the far-field stress magnitudes and orientations. This usually results in spalling and slabbing of the rock near the excavation boundaries (Martin et al., 1997). The occurrence of failure in hard brittle rocks where the tangential stresses are at their maximum magnitudes, commonly results in a v-shaped failed zone called 'v-shaped notch' (Martin et al., 1997). A v-shaped notch failure was observed at the crown and the floor of the test tunnel as illustrated in Figure 2-8, where the maximum compressive stresses were concentrated (Read, 2004).

Figure 2-8: MBE tunnel: a) final v-shaped notches; b) cross section of notch in tunnel invert; c) notch-tip in tunnel invert (Read, 2004)

The DoF around the MBE tunnel varied throughout its 46 m length. Everitt and Lajtai (2004) discussed that the difference between the grain sizes of granite and granodiorite played an important role in this variability. Therefore, regardless of the excavation method, the depth of v-shaped notch in the fine grained granite was less than the medium grained granite (Figure 2-9).
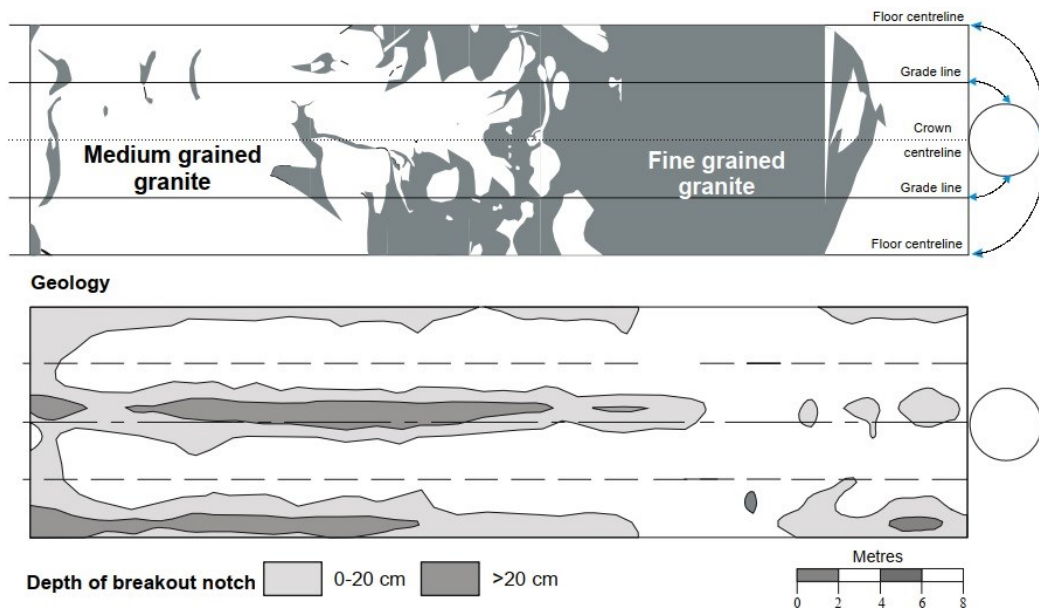
Figure 2-9 Influence of geology on breakout development along MBE tunnel (after Everitt and Lajtai, 2004)

The development of the breakout notch at different locations (Figure 2-7b) along the MBE tunnel is presented in Figure 2-10a to d. The micro-seismic events and acoustic emission data captured around the test tunnel are presented in Figure 2-10e. According to Read and Martin (1996), the tensile regions at the sidewall of the tunnel are considered as the damaged zone, however, the damage in these regions is limited to micro-cracks. The extent of this zone was limited to 1 m from the tunnel boundary based on the acoustic emission activity recorded by the monitoring system. The difference between the extent of damage in the roof and the invert of the tunnel is reported to bbe mainly due to the different stress paths and the confinement provided by the muck in the floor (Martin, 1993; Read et al., 1998; Hajiabdolmajid et al., 2002).
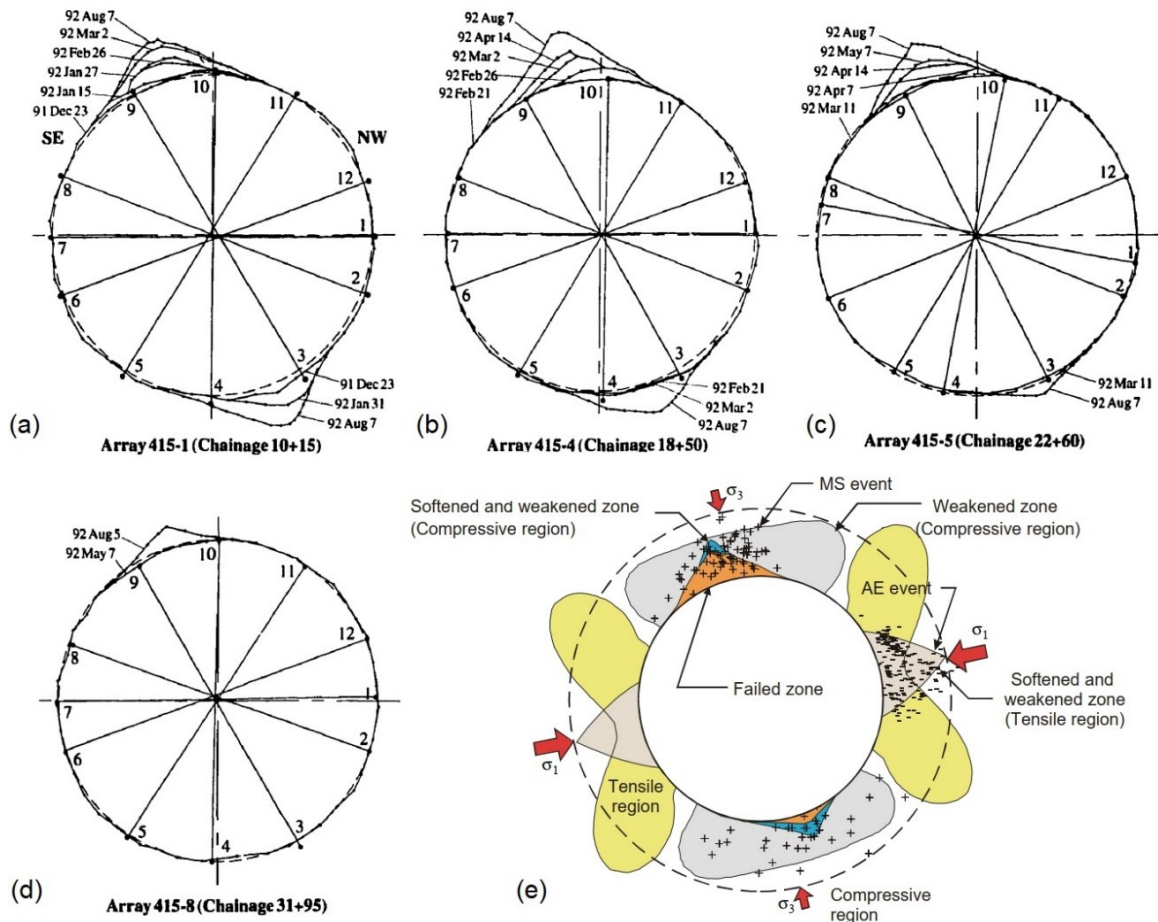
Figure 2-10 Progressive development of breakout notches in MBE tunnel at convergence arrays: a) 415-1, b) 4, c) 415-5 and d) 415-8 (after Read and Martin, 1996); e) EDZ characteristics around MBE tunnel including micro-seismic (+) and acoustic emission (-) events, as well as compressive, tensile and weakened zones (Read, 2004)

17

The monitored data and direct observations in the MBE tunnel indicate the progressive nature of brittle rock failure. According to Martin (1993), Martin et al. (1997), and Read (2004), the progressive brittle failure in the MBE tunnel involves multiple stages as demonstrated schematically in Figure 2-11:

1) Initiation: micro-cracks begin to form in a narrow region ahead of the advancing tunnel face. The locations of these cracks are determined using micro-seismic monitoring.

2) Dilation: at this stage, the maximum tangential stress exceeds the rock strength, hence, shearing and crushing in this zone, called the process zone, takes place and dilation at the grain scale leads to the formation of thin slabs. The process zone controls the failure progression, and if this zone is stabilized the failure progress stops.

3) Slabbing and spalling: shearing, splitting and buckling result in the development of larger and unstable slabs.

4) Stabilization: the final geometry provides enough confinement especially at the notch-tip that stabilizes the process zone.
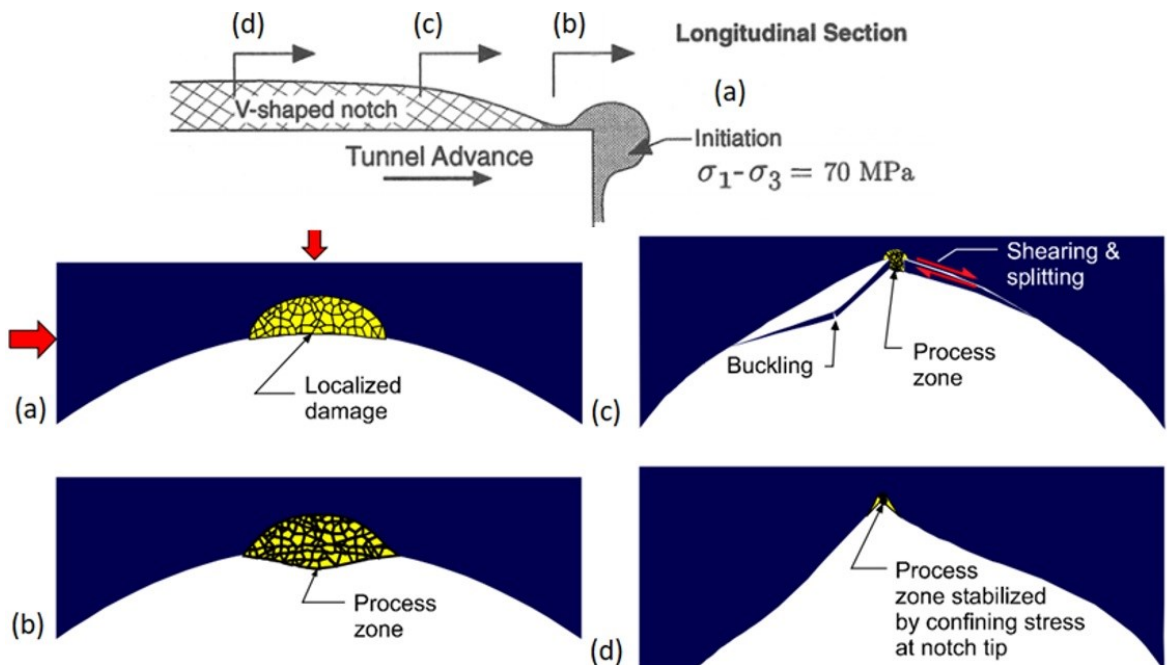
Figure 2-11 Schematic progression of major stages of brittle failure with corresponding location in MBE tunnel: a) initiation; b) dilation; c) slabbing and spalling; and d) stabilization (after Martin et al, 1997 and Read, 2004)

2.4.2 Excavation Stability Study

According to Read (2004) and Martino and Chandler (2004), the Excavation Stability Study (ESS) was carried out in 420 m Level of the URL using the drill-and-blast technique with different tunnel geometries as illustrated in Figure 2-12. The locations of these tunnels at 420 Level are shown in Figure 2-1b. The U1, U2 and U3 tunnels were located at the upper level (Room 418), the M1, M2 and M3 tunnels were at the main level (Room 417) and L1, L2 and L3 tunnels were excavated at the lower level (Room 421). The objective of the ESS was to investigate the stability and the EDZ around underground openings as a function of: 1) tunnel geometry and orientation; 2) geology; and 3) excavation method. The excavations were designed to be in an area of mixed geology in both granite and granodiorite and away from the influence of surrounding excavations.
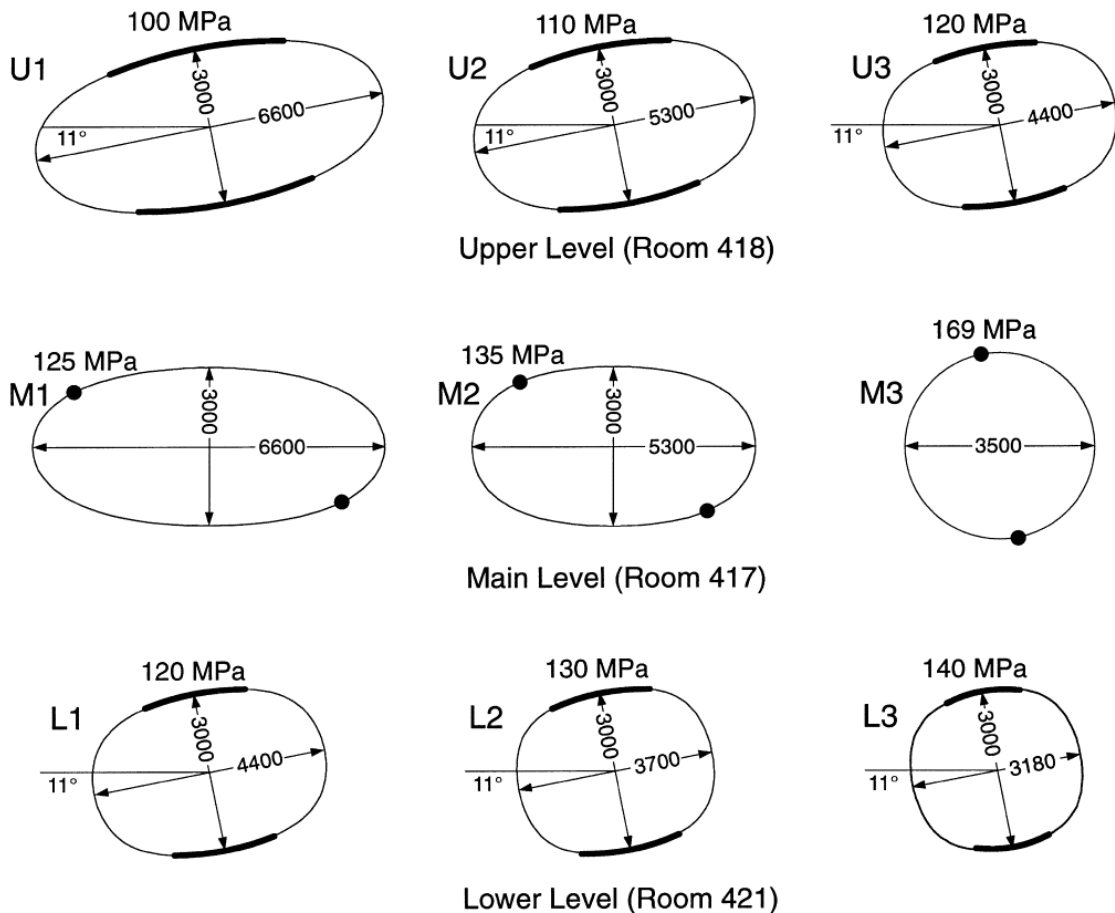
Figure 2-12 Cross-sections of 9 tunnels excavated for ESS. The peak compressive boundary stress magnitudes and distribution from 2D elastic analysis are shown with black circles and bolded lines on the tunnel boundaries (Read et al., 1998)

The potential effects of three-dimensional (3D) stress paths and rock fabric on the stability of the tunnels subjected to in situ stresses with different orientations relative to tunnel axis were studied in the ESS. The results of their investigations indicated that excavation geometry and geological variability influence the rock mass damage and stability. For instance, U1 and M1 had the same geometry but their orientations relative to the major principal stress were different. Thus, the maximum tangential stresses are different around the tunnel boundaries. Read (2004) summarized the results of the ESS and accordingly, suggested that careful characterization of the geological variability and rock fabric is essential in the excavation stability analysis.

Several researchers have attempted to numerically replicate the MBE tunnel and the v-shaped notch failure around its periphery. The following section provides an overview of previous simulations of the MBE tunnel, regardless of their success in capturing the v-shaped notch failure.

2.5 Simulation of Brittle Failure Around MBE Tunnel

The assessment of the stability of underground openings requires insight into the stress distribution around the excavations. According to Brady and Brown (2006), the stress distribution can be obtained using analytical solutions and numerical modeling. Analytical solutions, e.g., equations proposed by Kirsch (1898), necessitate certain assumptions to be made for excavation geometry and rock mass behavior to simplify the problem. For example, they are generally developed for a circular opening excavated in a homogeneous, elastic or elastic-plastic medium subjected to an isotropic stress field under plane strain condition.

In order to overcome some of the limitations of closed-form solutions, numerical modeling is often used. According to Hoek et al. (1991), numerical methods are classified into two broad categories: boundary and domain methods. In the first type, the boundary of the excavation is discretized into several elements, while in the domain methods, the interior is divided into simple zones. According to Li et al. (2019), numerical methods used to simulate a rock mass can be classified into three main categories: continuum,

discontinuum and hybrid continuum-discontinuum methods. An overview of numerical methods applied to rock mechanics can be found in Jing and Hudson (2002) and Brady and Brown (2006).

2.5.1 Continuum Modeling of V-Shaped Notch Failure

2.5.1.1 Elastic Model

A conventional method used for stability analyses of underground excavations is based on calculating the Factor of Safety (FS). FS is the relationship between capacity (C) and demand (D), normally expressed in terms of balance of forces but sometimes in terms of stresses, hence, FS = C/D. The FS of an underground opening is then a ratio between the strength and the induced stress. Any FS values below 1 is an indication of failure in this approach.

Using Kirsch equations, the maximum tangential stress for the test tunnel is calculated to be 169 MPa (i.e., $\sigma_{max} = 3\sigma_1 - \sigma_3 = 169$; $\sigma_1 = 60$ MPa and $\sigma_3 = 11$ MPa). Assuming that the average UCS of LdB granite is 213 MPa, the FS is calculated to be 1.26, suggesting a stable condition for the test tunnel. However, failure occurred at the top and bottom of the MBE tunnel in the form of a v-shaped notch as reviewed earlier.

Martin (1997) discussed that the loading path is influential on the ultimate strength of the rock mass near an excavation boundary. As shown in Figure 2-13, the in situ stress path that a point experiences on the tunnel boundary differs from those applied to a rock specimen in the laboratory. In standard rock mechanics laboratory tests (e.g., uniaxial and triaxial compression tests), the loading path is monotonically increasing. Martin (1997) suggests that the true in situ stress path can be estimated using 3D elastic analyses (Figure 2-13). This figure shows the stress paths of two points at the top and bottom of the MBE tunnel where the tangential stresses are at their peak values. These stress changes are captured by simulating the excavation sequence; A, B, C and D are points ahead, at the tunnel face, behind the face and far behind the face, respectively. The stresses are captured and plotted in σ_1 - σ_3 space during the tunnel advance as the tunnel face approaches and passes these points. It can be observed that during the tunnel advance,

the induced-stresses exceed the crack initiation threshold and pass through the tensile zone. Martin (1997) discussed that rock is weaker when subjected to tension compared to compression, therefore, damage is more prone to occur in the tensile zones, which could lead to rock mass strength degradation. After the tunnel is excavated, the stresses reach their final values that can be estimated using 2D analytical solutions such as Kirsch equations (σ_1 = 169 MPa, σ_3 = 0 MPa) or with a 2D elastic continuum model.
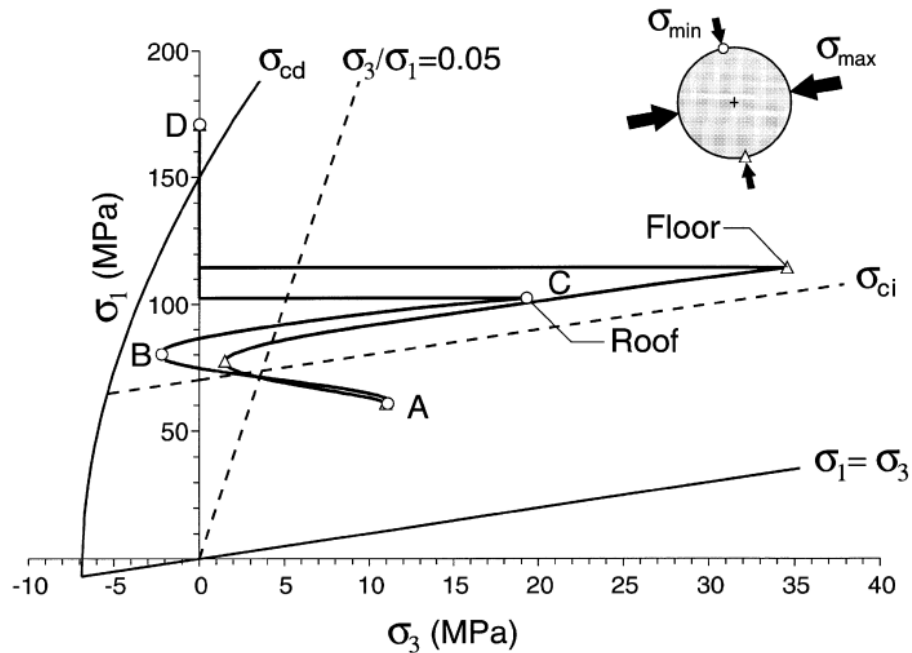
Figure 2-13 In situ stress paths at the top and bottom of MBE tunnel (Read et al., 1998)

Martin (1993), Martin (1997) and Hajiabdolmajid et al. (2002) discussed that the strength of a rock mass is influenced by the stress paths it experiences during an excavation. The difference between the depths of the failure in the top and bottom notches of the MBE tunnel can be an example for this statement. Figure 2-13 shows the difference between the stress paths in the crown and the floor of the test tunnel. Read et al. (1998) suggested that the tunnel axis is not perfectly parallel to the intermediate principal stress direction, therefore, the induced-shear stresses at the top and bottom are different. The stress path from 3D elastic analysis (Figure 2-13) shows that the roof region ahead of the tunnel face experiences higher deviatoric stresses in comparison with the floor (Read et al., 1998). Therefore, the roof of the tunnel is more damaged and the DoF is different from the floor.

Numerical simulations using linear elastic continuum models by Martin (1993) (Examine2D by Rocscience), and Hajiabdolmajid et al. (2002) (FLAC by Itasca Consulting Group Inc., 1995) demonstrated that no failure should occur near the MBE tunnel. Figure 2-14 shows the stress distribution around the MBE tunnel indicating that the FS is greater than 1 when the intact rock strength with a UCS of 213 MPa is used in the analysis.
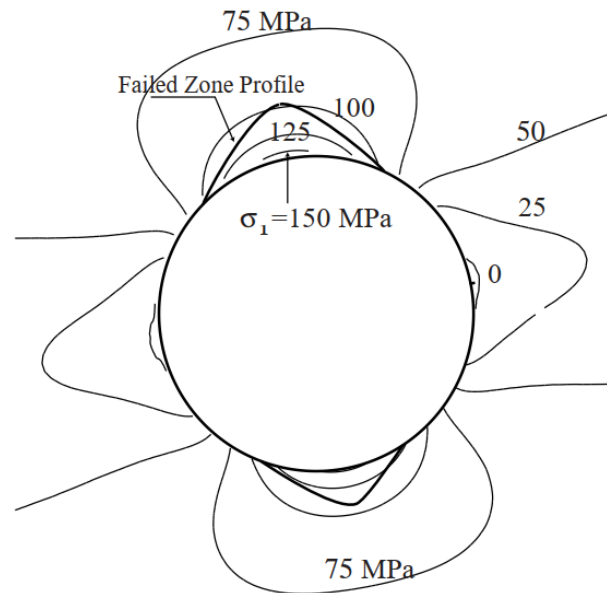
Figure 2-14 Major principal stress distribution in MBE tunnel from an elastic FDM model (Hajiabdolmajid et al., 2002)

In an attempt to simulate the progressive slabbing and spalling leading to the v-shaped notch failure, Read (1994) and Martin (1997) used an elastic approach which consisted of monotonic removal of the failed material, i.e., material with FS < 1 (Figure 2-15). The initial FS was calculated using the Hoek-Brown parameters for an unconfined long-term strength of 114 MPa with an s value of 0.25. As demonstrated in Figure 2-15a, the thin skin over the roof of the tunnel represents the failed material with a FS < 1. These elements were then manually removed (excavated) and a new model with updated tunnel geometry was ran. This process was repeated until the v-shaped notch geometry (see Figure 2-15b) similar to the actual profile of the failed zone was developed. According to Martin (1997), this approach overpredicted the DoF.
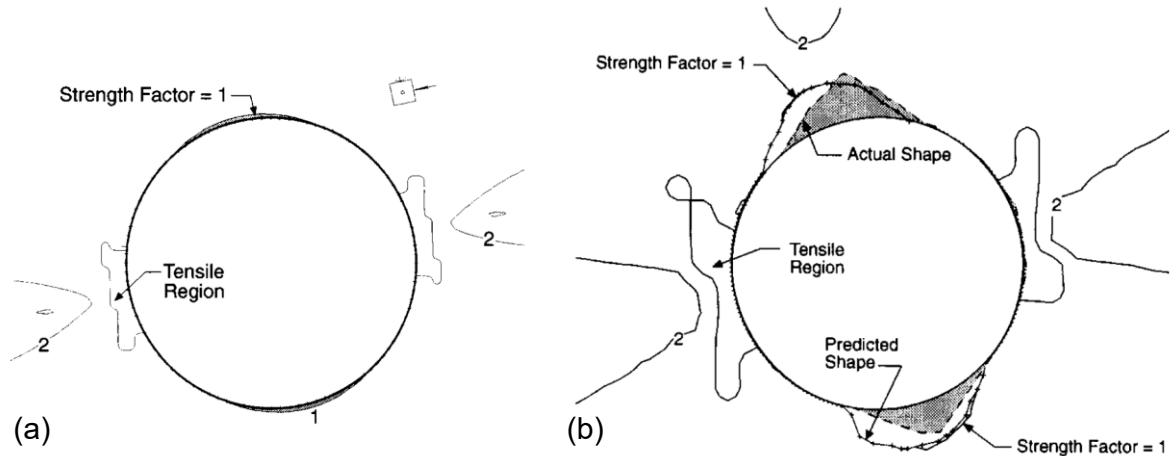
Figure 2-15 Elastic analysis with monotonic removal of failed material (i.e., FS < 1): a) formation of thin skins in top and bottom of MBE tunnel; b) estimated shape of the notch (after Martin 1997)

According to Martin et al. (1999), the initiation of brittle failure around underground excavations occurs when the maximum tangential stress is approximately 40% of the UCS of intact rock. Martin et al. (1999) discussed that the brittle failure around underground openings is mainly dominated by the loss of intrinsic cohesion, thus, the frictional component of the strength can be ignored when estimating the DoF. In the Hoek-Brown failure criterion, the m parameter is a representation of the frictional component of the strength, hence, by keeping m = 0, the strength envelope would be cohesion-based. Martin et al. (1999) used an elastic continuum model with m and s values equal to 0 and 0.11 (Figure 2-16a), respectively, and was able to estimate the DoF (i.e., when FS = 1). The relationship between the DoF and maximum tangential stress at the boundary, and a comparison between the DoF predicted by this approach and measured from case histories are presented in Figure 2-16b and c, respectively.
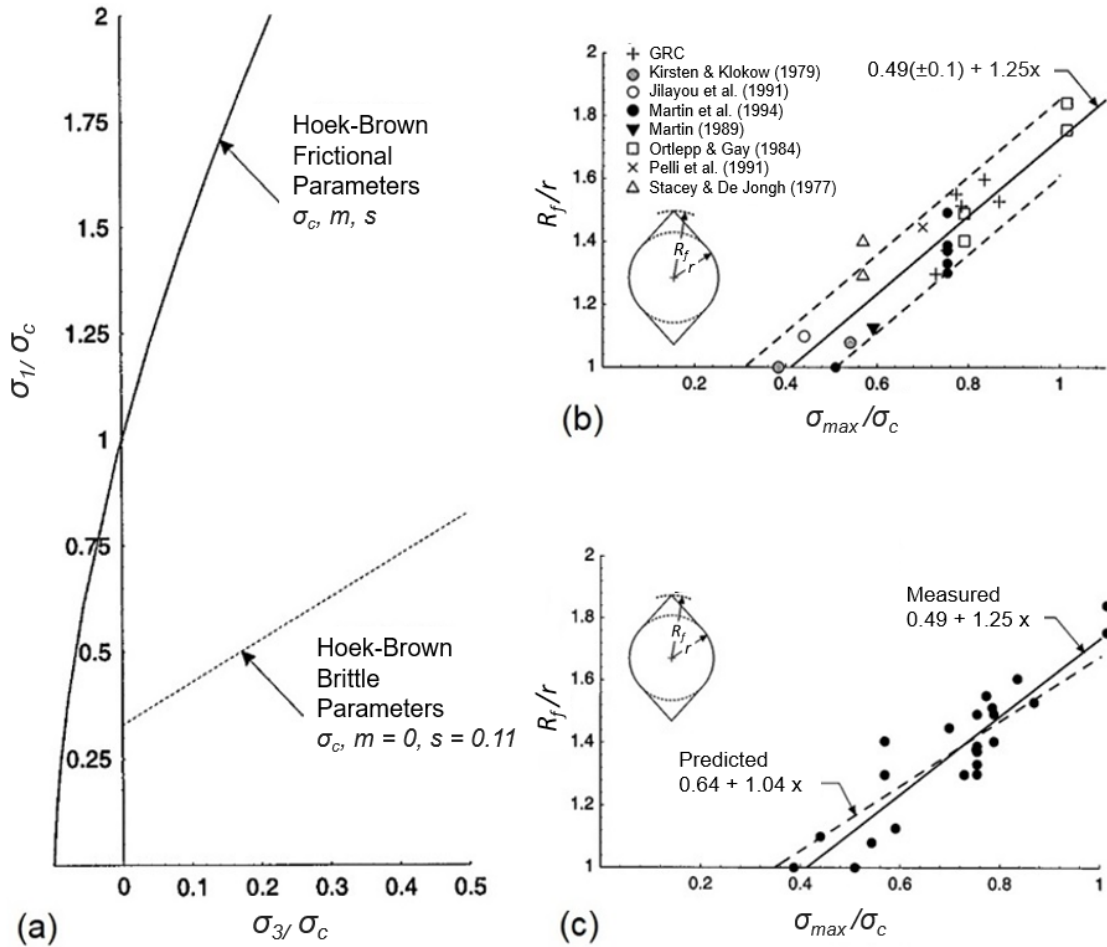
Figure 2-16 a) Hoek-Brown envelopes for frictional (i.e., intact rock strength) and brittle parameters (i.e., m = 0 and s = 0.11); b) relationship between radius of failure (R$_f$) and maximum tangential stress; and c) comparison between depth of failure using Hoek-Brown brittle parameters and measured from case histories (after Martin et al., 1999)

2.5.1.2 Elastic-Perfectly Plastic Model

An elastic-perfectly plastic constitutive law indicates that with increasing strain in the post-peak region, the stress level remains the same as the peak stress. Figure 2-17a illustrates the stress-strain behavior of an elastic-perfectly plastic material used in continuum numerical models. Hajiabdolmajid et al. (2002) discussed that this constitutive model is not representative of brittle rocks because the material weakening is not considered. In order to simulate the test tunnel using this approach, they assumed that the GSI is equal to 90, therefore, the UCS of the rock mass is equal to 128 MPa. The result

25

of this simulation shown in Figure 2-17b demonstrates that an elastic-perfectly plastic model cannot capture the v-shaped notches formed near the MBE tunnel.
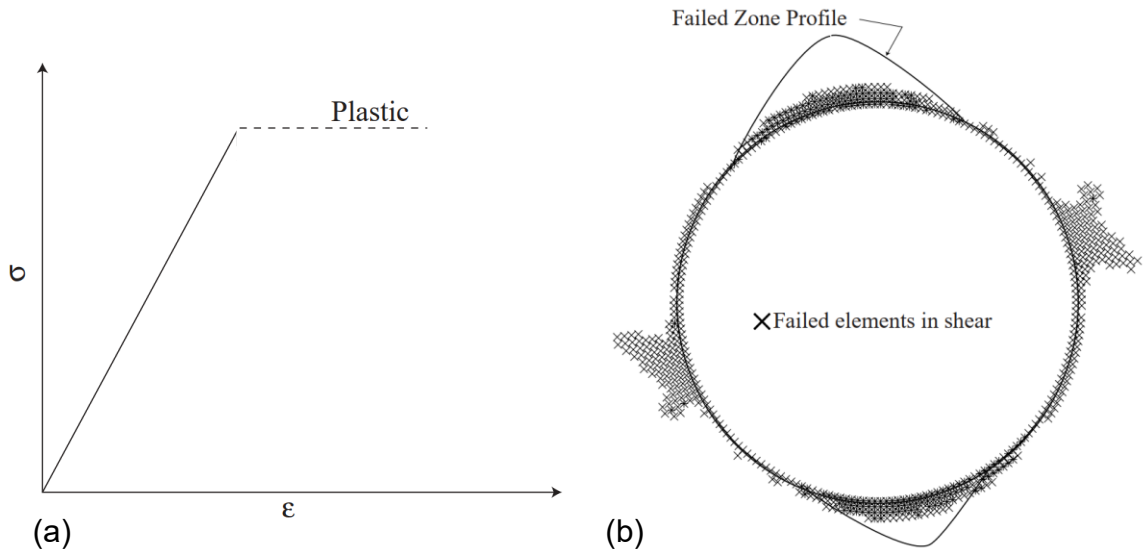
Figure 2-17 a) Elastic-perfectly plastic constitutive law; b) estimated depth of failure in MBE tunnel using elastic-perfectly plastic model in FLAC (Hajiabdolmajid et al., 2002)

2.5.1.3   Elastic-Brittle Model

Hoek et al. (1995) suggest that elastic-brittle constitutive law is suitable for modeling brittle materials. The stress-strain response of this constitutive model is demonstrated in Figure 2-18a. Martin (1997) used the long-term strength with residual m and s values of 1 and 0.01, respectively, to simulate the failure in the MBE tunnel using the FEM program PHASES (by Rocsceince), as shown in Figure 2-18b. Hajiabdolmajid et al. (2002) repeated this simulation in FLAC with a rock mass strength of 128 MPa, estimated based on a GSI of 90. The elastic-brittle models shown in Figure 2-18b and c underestimate the depth of failure and do not capture the EDZ, the shape of failure and realistic failure modes around the MBE tunnel.
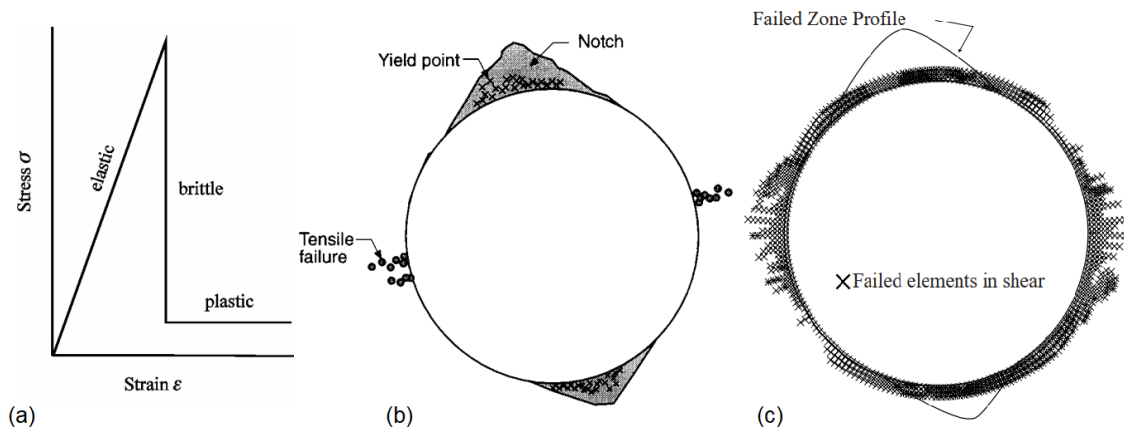
Figure 2-18 a) Elastic-brittle behaviour (Hoek et al., 1995). Estimated depth of failure in MBE tunnel using elastic-brittle model with: b) long-term strength and residual m and s values of 1 and 0.01, respectively (Martin, 1997); and c) rock mass strength based on a GSI of 90 (Hajiabdolmajid et al., 2002)

2.5.1.4 Cohesive Brittle Frictional Model

Martin (1997) proposed a constitutive model in which material yielding occurs when the constant deviatoric-stress criterion, i.e., $\sigma_1 - \sigma_3$ = 70 MPa, is met. The residual values for cohesion and friction used in this model, called Cohesive Brittle Frictional (CBF) model, according to Martin and Chandler (1994), are 7.46 MPa and 47°, respectively. An illustration of the stress-strain response of the CBF model is presented in Figure 21a. Martin (1997) used the CBF model to simulate the MBE tunnel and concluded that this method does not capture the shape of failure. However, the distribution of yielded elements resembles the locations of micro-seismic events (Figure 2-10d) recorded in the field.
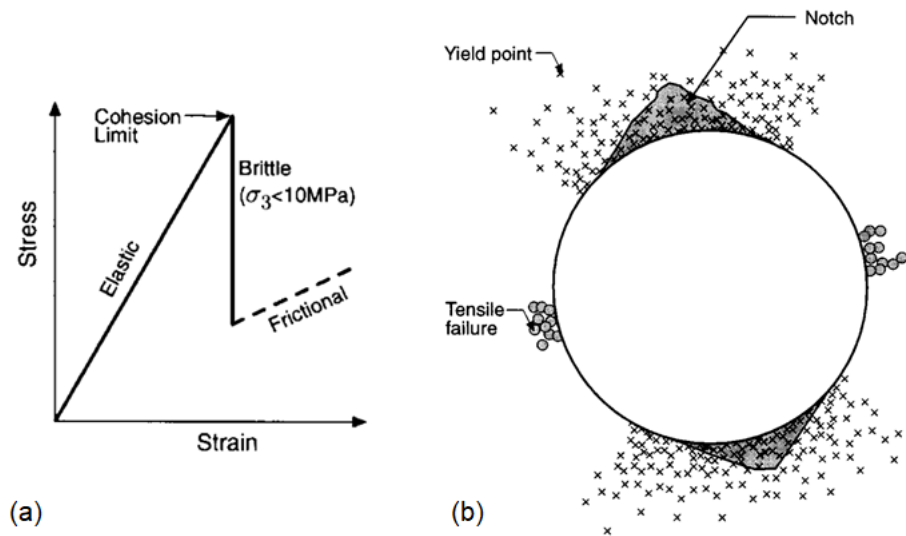
Figure 2-19 a) Stress-strain response of CBF constitutive model; b) estimated depth of failure in MBE tunnel using CBF model in PHASES (After Martin, 1997)

2.5.1.5 Cohesion Weakening Frictional Strengthening (CWFS) Model

Studies such as Martin and Chandler (1994) and Martin et al. (1999) showed that the cohesional and frictional components of the strength are not mobilized simultaneously (Figure 2-5). Based on the logic that cohesion is degraded gradually due to tensile cracking, and friction can only be fully mobilized after the cohesion is significantly reduced, Hajiabdolmajid et al. (2002) proposed a Cohesion Weakening Frictional Strengthening (CWFS) model (Figure 2-20a and b) in FLAC to simulate the brittle failure around the test tunnel. In the CWFS model, cohesion-loss and frictional strength mobilization are functions of plastic shear strain. Hajiabdolmajid et al. (2002) discuss that the residual values for these components must be calibrated against laboratory tests and in situ failure. The result of numerical simulation using the CWFS model in FLAC for predicting the depth and shape of failure is shown in Figure 2-20c. It can be seen in this figure that the depth and shape of failure agree well with field observations. The failure mode of brittle failure at low confinements (e.g., at the vicinity of tunnel walls) is expected to be due to tension. Accordingly, the limitation of this approach is that the failure mechanism is not realistically captured as the elements in the v-shaped notch area are solely failed in shear (Figure 2-20c).
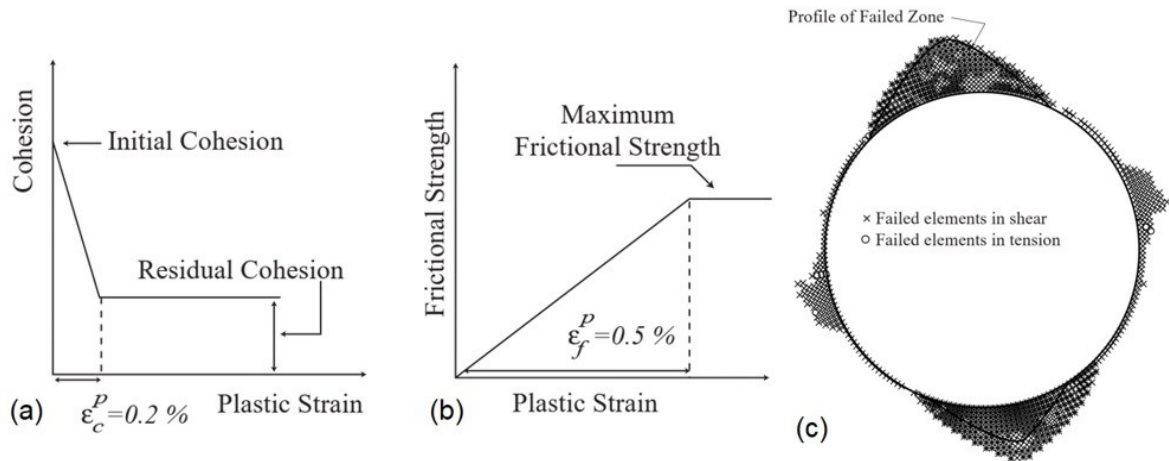
Figure 2-20 CWFS constitutive model: a) cohesion-loss as a function of plastic strain; b) frictional strength mobilization as a function of plastic strain; and c) simulated depth of failure in MBE tunnel using CWFS in FLAC (after Hajiabdolmajid et al., 2002)

Rafiei Renani and Martin (2018) examined the gradual decrease of cohesion and mobilization of friction for LdB granite during laboratory tests. The results of their simulations showed that using the conventional CWFS, in which the cohesional and frictional strength components linearly change with plastic strain (Figure 2-20a and b) cannot capture a realistic stress-strain response for a brittle rock. Therefore, to overcome this problem, a non-linear model was proposed by Rafiei Renani and Martin (2018) in which, the degradation of cohesion and mobilization of frictional strength component are gradual. An illustration of the proposed CWFS model is presented in Figure 2-21a. The back-calculated UCS of the rock mass in this simulation is 110 MPa in their study. In order to confirm the applicability of the proposed model, they simulated the MBE tunnel with FLAC3D (Itasca Consulting Group Inc, 2009). The result of their numerical simulation is shown in Figure 2-21b. It can be concluded that by using the proposed CWFS, the depth and shape of failure can be captured. It should be noted that the failure captured by this model is shear dominated which is not consistent with that of brittle failure at low confinement, therefore, the true failure mechanism cannot be captured using this method.
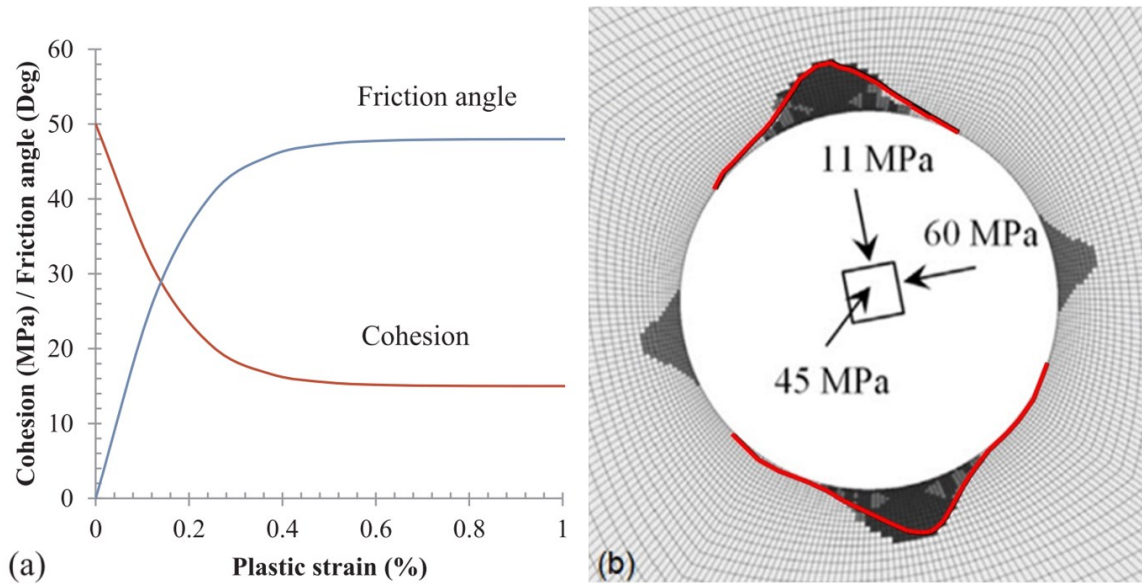
Figure 2-21 a) Proposed CWFS model for gradual degradation of cohesion and mobilization of friction as a function of plastic strain; b) estimated depth and shape of failure in MBE tunnel using proposed CWFS model in FLAC3D (after Rafiei Renani & Martin, 2018). Actual failure profile is added with red lines for comparison purposes

2.5.1.6   Damage Initiation Spalling Limit (DISL) Model

The DISL proposed by Diederichs (2003) is an empirical criterion for massive to moderately jointed rock masses. Diederichs (2003) discussed that rock mass strength near the excavation is controlled by damage initiation, i.e., tensile fracture initiation and accumulation. Therefore, the failure envelope for brittle rocks can be represented by an s-shaped curve (Figure 2-22). According to Diederichs (2003), when the stress path exceeds the 'damage initiation threshold', micro-cracks begin to form. At higher confinements, the accumulation of micro-cracks results in macro-scale shear failure.
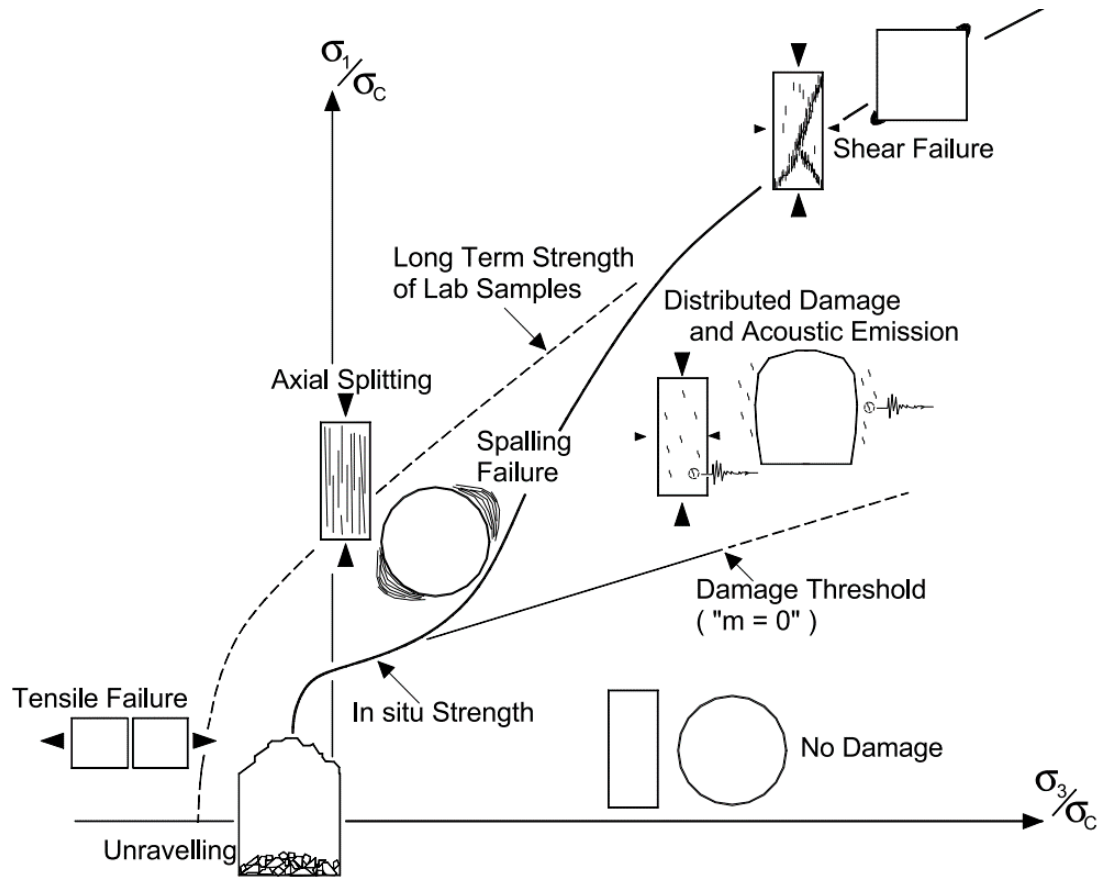
Figure 2-22 Schematic s-shaped failure envelope for brittle rocks illustrating multiple regions and failure modes: no damage, unravelling, spalling and shear failure (Diederichs, 2003)

Based on the concept of s-shaped failure envelope, Diederichs (2007) proposed the DISL model (Figure 2-23a). In this model, the initiation of brittle failure is related to tensile cracking, therefore, the frictional component is ignored. It can be discussed that the DISL is another form of the CWFS, where the transition from peak to residual strength is instantaneous and independent of plastic shear strain. The residual strength envelope, however, is dominated by friction thus the s value is nearly zero (Figure 2-23a). As the peak and residual strength envelopes in this model are different, the failure can be divided into three regions: 1) at low confinement where stress drop occurs as the peak stress is reached; 2) at the intersection of peak and residual strength envelopes where the model is elastic-perfectly plastic because the pair have the same values; and 3) at high confinement, where peak stress is lower residual stress.
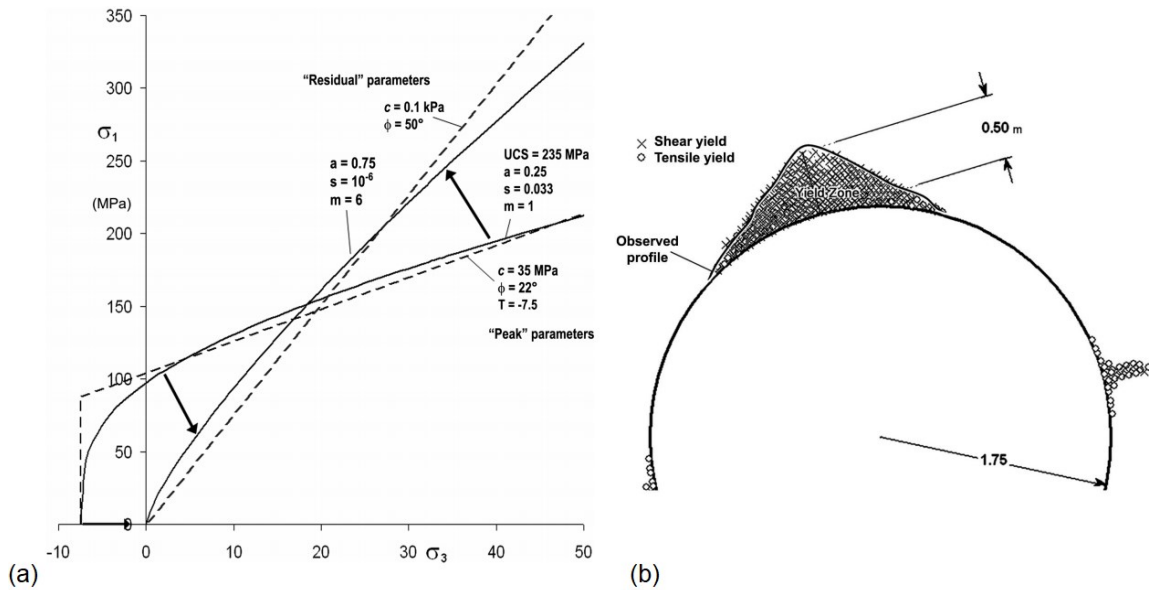
Figure 2-23 a) Peak and residual envelopes used in the DISL model. The arrows show the strength-softening and strength-hardening that occur after reaching to peak strength; b) simulated depth of failure in MBE tunnel using DISL model in Phase[2] (after Diederichs, 2007)

Diederichs (2007) used the DISL in the finite element program Phase[2] (Rocscience, 2005), and simulated the MBE tunnel. The input parameters for simulating the v-shaped notch failure in the MBE tunnel are presented in Figure 2-23a. Note that the UCS of the rock mass in this study was 100 MPa. The results presented in Figure 2-23b indicate that the DISL approach can be used to properly estimate of the depth and shape of the failure. It can be observed that the failure mode in the notch area is dominantly in shear, and therefore, is not in consistent with the brittle failure mechanism at low confinement. This is due to the fact that the model is homogeneous, consequently, only shear yielding can be expected under compressive loading conditions.

2.5.1.7   Instantaneous CWFS Model Considering Tunnel Boundary Irregularities

Cai et al. (2004) highlighted the importance of irregularities around the excavation boundary and its potential influence on tensile damage initiation and propagation. It was understood from simple linear elastic analysis that a smooth wall boundary (Figure 2-24a) compared to an irregular wall surface (Figure 2-24b) results in different stress redistribution. Cai et al. (2004) discussed that the local stress concentration due to the

irregularities increases the maximum tangential stress from 169 MPa to 195 MPa, therefore, promotes early notch formation.
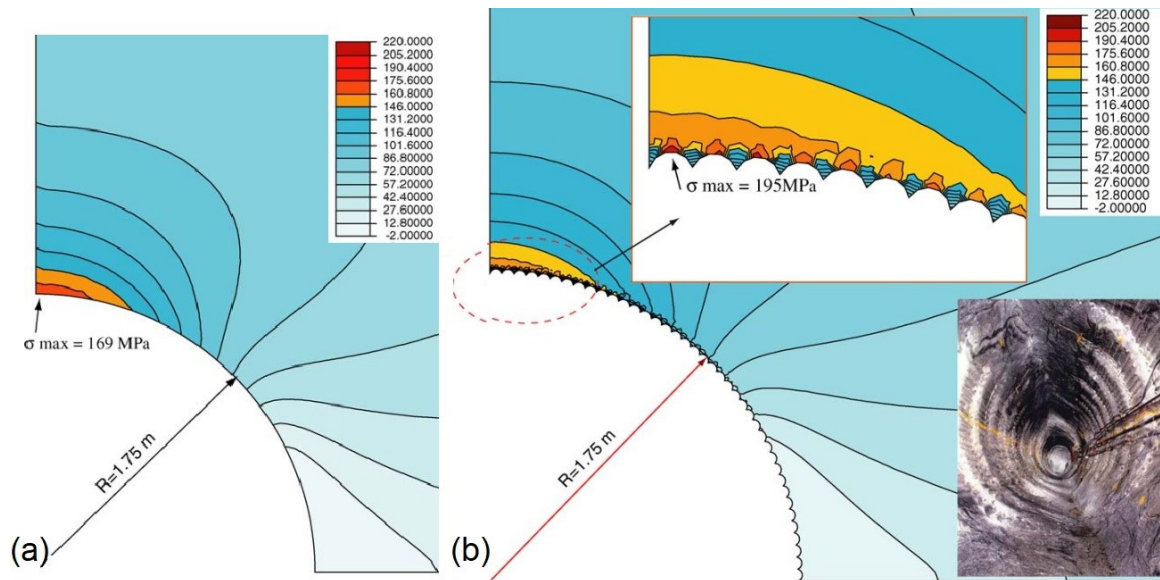
Figure 2-24 Major principal stress redistribution around MBE tunnel with: a) smooth wall surface; b) irregular wall surface (after Cai et al., 2004)

Accordingly, Cai and Kaiser (2014) simulated the MBE tunnel with irregular wall surface. The peak and residual uniaxial compressive strengths were set to be 175 MPa and 0.5 MPa (Figure 2-25), respectively. Cai and Kaiser (2014) discussed that the conventional DISL model (Figure 2-23a) is based on the interpretation of rock failure using simplified elastic studies with smooth wall boundary, which lead to an 'apparent' in situ rock strength that is much lower than the intact rock UCS (i.e., about 30% of UCS). They implied that the 'actual' in situ rock strength is higher than the CI threshold at low confinement, approximately 80% of the peak strength of intact rock. They concluded that the approximation of in situ rock strength, 30% to 40% of UCS, is only applicable when the geometry is simplified; thus, using the crack initiation threshold as the rock strength at low confinement leads to an underestimation of rock mass strength when boundary irregularities are included in the model.
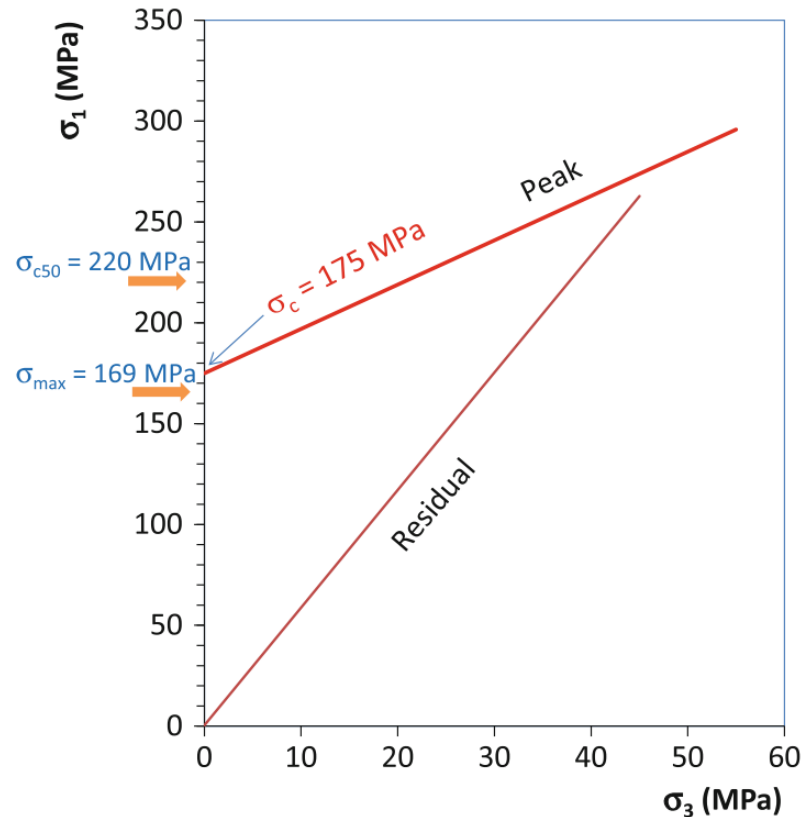
Figure 2-25 Peak and residual strength envelopes used in FEM model with as-built (irregular boundary) tunnel geometry (Cai & Kaiser, 2014)

By considering the fact that in the MBE tunnel, the boundary is not smooth and perfectly circular (Figure 2-26a and b), Cai and Kaiser (2014) created an 'as-built' model in Phase2 (by Rocscience). They discuss that the line-drilling excavation method (see Figure 2-7a) created irregularities in the boundary of the tunnel which imposes stress redistribution around the boundary (Figure 2-24). The result of their simulation which is in agreement in terms of the depth and shape of failure with field observations is illustrated in Figure 2-26c. It should be noted that the failure mechanism (i.e., tensile yielding) is realistically simulated, however, the EDZ around the test tunnel cannot be captured using this method.
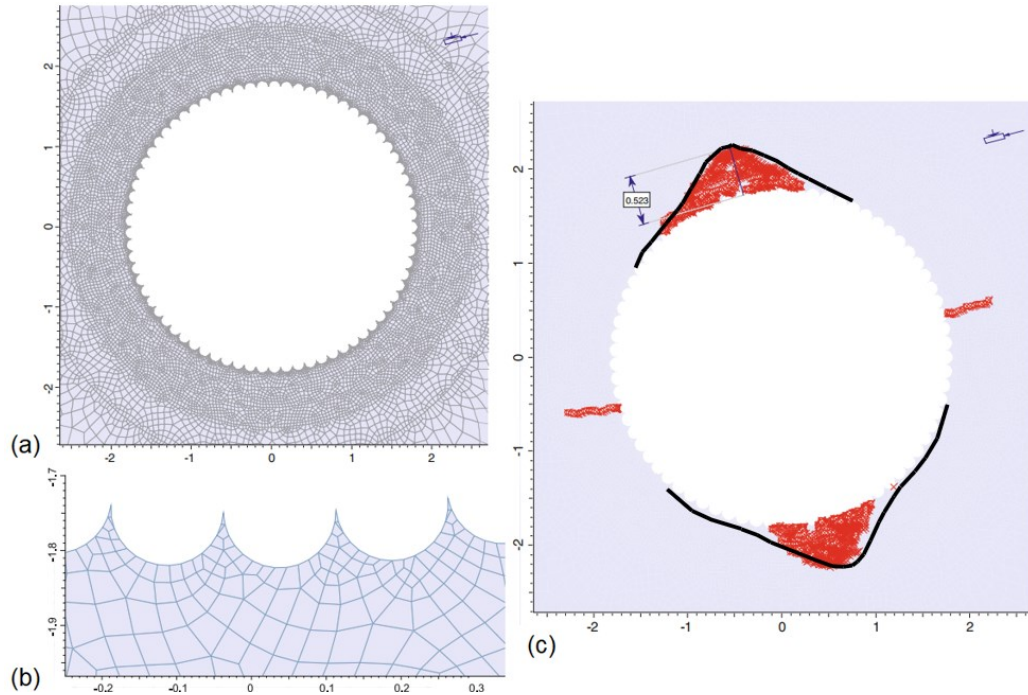
Figure 2-26 a) Finite element model of MBE tunnel with 'as-built' geometry at the tunnel boundary; b) closer view of irregularities at the boundary; and c) simulated depth and shape of failure in MBE tunnel using 'as-built' model (after Cai & Kaiser, 2014). Actual notch profile is added with black lines for comparison purposes

2.5.2   Discontinuum Modeling of V-Shaped Notch Failure

According to Jing and Hudson (2002), in discontinuum numerical methods, e.g., Distinct Element Method (DEM), the domain of interest consists of an assemblage of rigid or deformable blocks/particles, interacting with each other through a contact or bond model. Accordingly, the properties of both blocks/particles and contacts/bonds should be determined. The behavior of the blocks and contacts is controlled by different constitutive models. Li et al. (2019) classified the discontinuum methods based on their logic of time integration into implicit (e.g., Discontinuous Deformation Analysis (DDA)) and explicit methods. According to Jing and Hudson (2002) and Li et al. (2019), the most well-known explicit DEM programs are Particle Flow Code (PFC) for 2D and 3D analyses, and Universal Distinct Element Code (UDEC) for 2D and 3DEC for 3D problems. A comprehensive review of discontinuum numerical methods can be found in Bobet et al.

(2009). The following sections provides a brief review of the simulation of v-shaped notch failure around the MBE tunnel using discontinuum models.

2.5.2.1 Simulation of V-Shaped Notch Failure Using PFC

In PFC, the disc-shaped particles are bonded to the surrounding particles at their contact points. This allows for simulating the key aspects of micro-behaviour of brittle rocks, such as internal cracking and heterogeneity of stress and strain.

Potyondy and Cundall (2004) used PFC and calibrated the model to the Brazilian tensile and triaxial compressive strengths of LdB granite. They used the calibrated PFC model coupled with FLAC to simulate the v-shaped notch failure around the MBE tunnel. However, the model calibrated to the intact rock properties could not capture the observed brittle failure. Therefore, a series of sensitivity analyses on the bond strength of the PFC model was carried out. The UCS of the rock mass model in this study was reduced from the intact rock peak strength (i.e., 213 MPa) to about 120 MPa. As discussed by Potyondy and Cundall (2004), the formation of v-shaped notch initiates when the maximum tangential stress exceeds approximately 120 MPa. Figure 2-27 illustrates the model with a strength reduction factor of 0.6 (i.e., estimated PFC model strength of 120 MPa) that captured the v-shaped notch in the MBE tunnel.
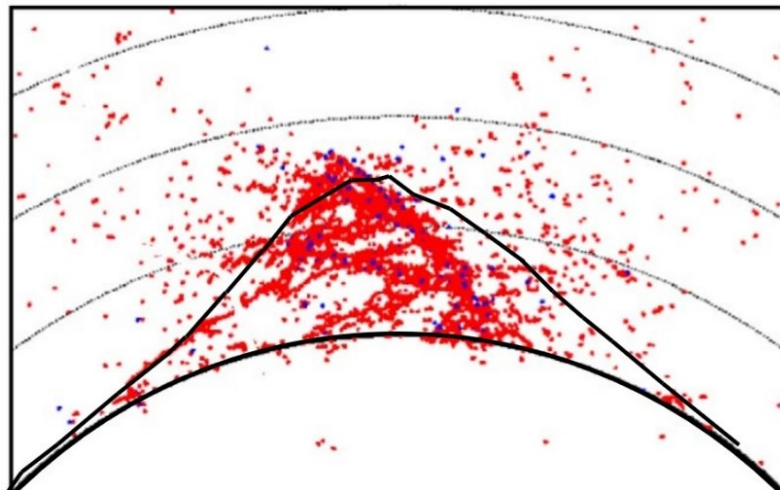
Figure 2-27 Simulated depth of failure in the MBE tunnel using a coupled PFC-FLAC model with a strength reduction factor of 0.6 applied to the calibrated PFC model. Blue and red colours correspond to shear and tensile failure, respectively (after Potyondy & Cundall, 2004). Actual notch profile is added with black lines for comparison purposes

Hazzard and Young (2004) used a technique in PFC to simulate deformation, damage and seismic events in brittle rocks subjected to compressive stresses. They developed an approach in PFC to capture seismicity by monitoring and analysing the failed contacts between the particles. Thereafter, a UCS test was simulated for LdB granite and the applicability of the technique to reproduce micro-seismic events observed in laboratory tests was evaluated. In order to validate their model, they simulated the MBE tunnel to capture the distribution of in situ seismicity around the failure zone. The UCS of their rock mass model was approximately 120 MPa. A comparison between the seismicity captured using their method with actual recorded events around the MBE tunnel is illustrated in Figure 2-28a and Figure 2-28b, respectively. It is observed that the locations of micro-seismic events recorded in the field are marginally extended in lateral directions, however, the simulation results fit the recorded data in terms of the DoF. According to Hazzard and Young (2004), the test was run for a simulated 1-year period and the events stopped after approximately 4.5 months, which is in agreement with the excavation time of the MBE tunnel.
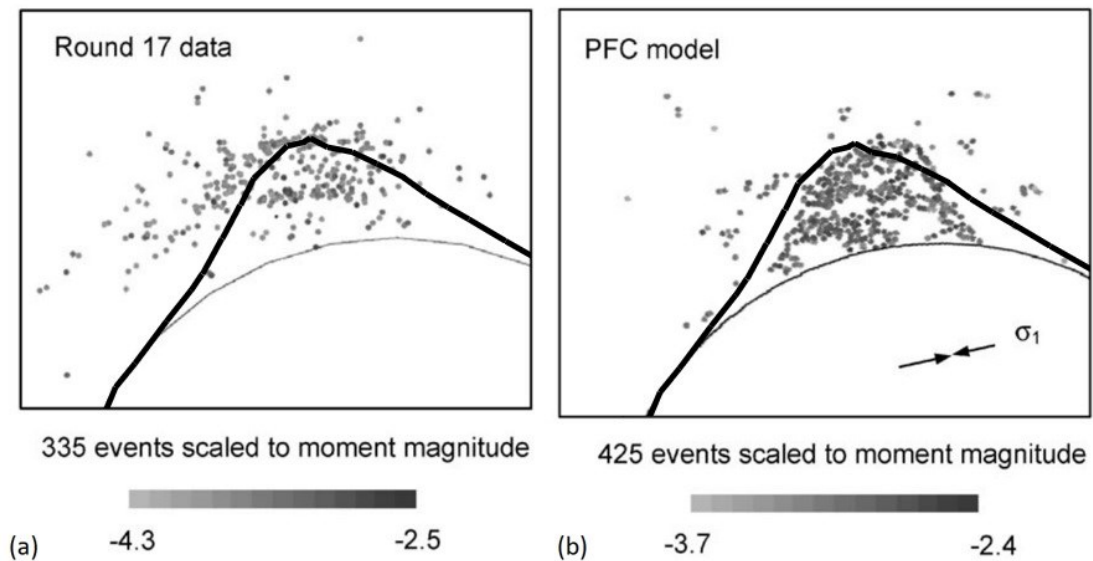
Figure 2-28 a) Actual recorded seismic events in top notch of MBE tunnel; b) seismicity captured by PFC model (b). Grey scale shows the magnitude of events (after Hazzard & Young, 2004). Actual notch profile is added with black lines for comparison purposes

The influence of stress path on stress-induced fracturing in brittle rocks was investigated by Bahrani et al. (2019) using a 2D clumped PFC model, calibrated to the properties of

intact LdB granite with a UCS of 213 MPa. The objective of this investigation was to explore the potential effects of stress path on the depth of damage. Therefore, the MBE tunnel was first simulated using RS2, as illustrated in Figure 2-29a, with intact rock properties and the Internal Pressure Reduction (IPR) approach to simulate the 3D tunnel advance. The 2D stress paths of seven points on the boundary and adjacent to the tunnel wall (Figure 2-29b) were then applied to the calibrated PFC2D model. Figure 2-29c demonstrates the microcracks developed at the end of each stress paths in the clumped PFC model, shown in Figure 2-29b. It can be seen in this figure that the damage density decreases rapidly with increasing distance (i.e., increasing confinement).
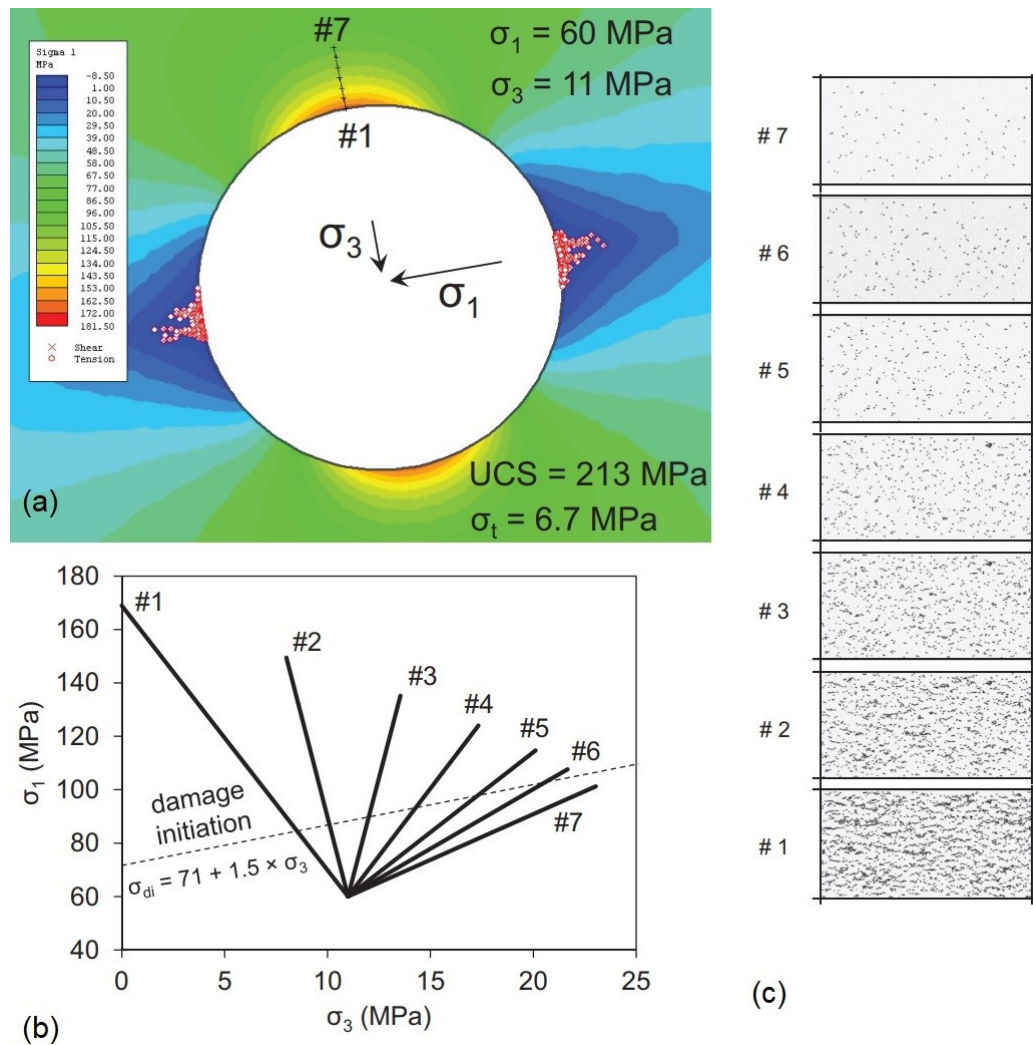
Figure 2-29 a) Contours of major principal stresses in in RS2 with intact rock properties, showing locations of 7 monitoring points; b) 2D stress paths of 7 monitoring points during excavation along with damage initiation threshold; and c) contact failure in clumped PFC model after application of 2D stress paths (after Bahrani et al., 2019)

Bahrani et al. (2019) discussed that although the UCS of both the FEM and clumped PFC models are 213 MPa, the continuum model does not capture the damage around the tunnel. In contrast, the DEM model in this indirect approach is able to capture the extent of damage observed in the field due to its heterogeneous nature. They further discussed that the compressive stresses cause the micro-cracks to grow at a stress level which is drastically lower than the peak compressive strength of the intact rock. According to Bahrani et al. (2019), this approach is not capable of simulating in situ spalling process. They suggested that a 3D coupled continuum-discontinuum method is likely the solution for accurately simulating the failure around the MBE with intact rock properties.

2.5.2.2 Simulation of V-Shaped Notch Failure Using UDEC and 3DEC

Shin (2010) used UDEC (Itasca Consulting Group Inc., 1996) to investigate and simulate the EDZ around the test tunnel. They used an approach based on the Voronoi tessellation technique to produce polygonal blocks; thus, the interior is an assemblage of blocks/grains that interact with each other at their contacts surfaces. This method is called a Grain-Based Model (GBM) in the literature. Two sets of micro-properties are needed for blocks and block boundaries in UDEC-GBM. Shin (2010) calibrated the model by simulating the UCS and confined compression tests, as well as the BTS and DTS tests. Shin (2010) also compared the simulated stress-strain curves with those from laboratory tests on the intact LdB granite. The target UCS of the UDEC-GBM was set to 205 MPa, to be the same as the UCS of intact LdB granite. The micro-properties of the contacts followed the CWFS model, and the blocks were assumed to be elastic. The failure envelope obtained from this model is illustrated in Figure 32, which also show the failure modes over a range of confinement. The Hoek-Brown and equivalent Mohr-Coulomb failure envelopes of the intact LdB granite are additionally shown in Figure 2-30.
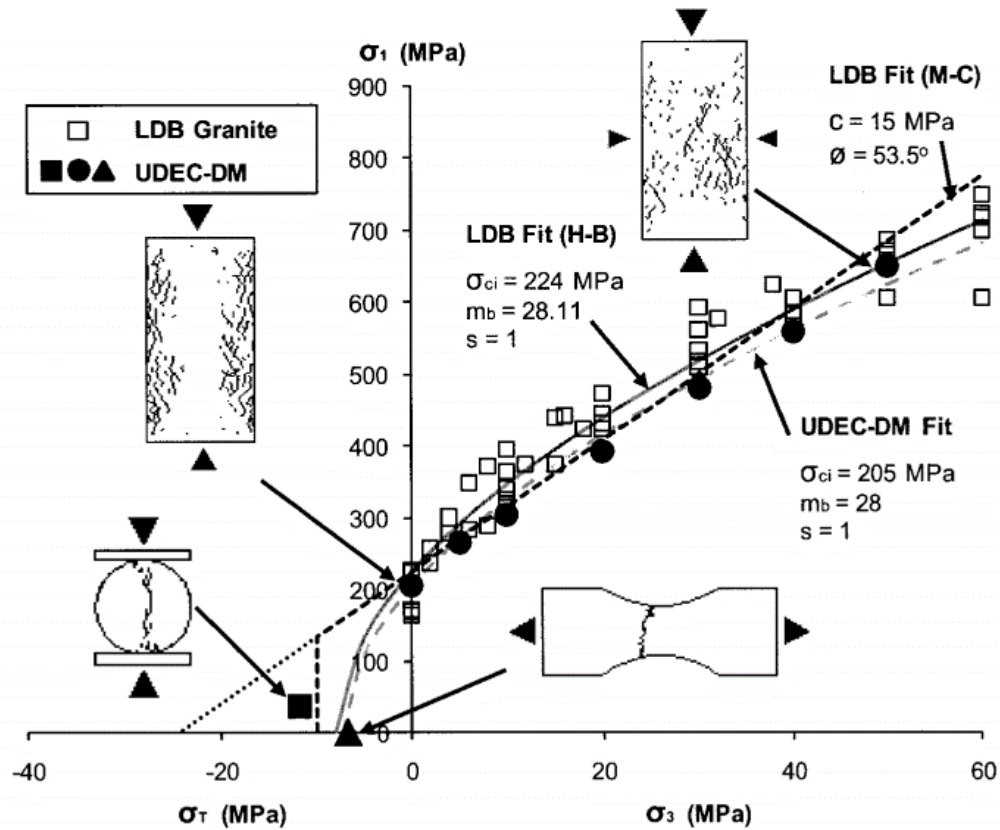
Figure 2-30 Strength envelope obtained from calibrated UDEC-GBM in comparison with intact rock strength envelopes for LdB granite and failure modes of different laboratory test simulations (Shin, 2010)

Shin (2010) upscaled the calibrated UDEC-GBM to simulate the MBE tunnel, as shown in Figure 2-31a. The development of the cracks around the MBE tunnel from the UDEC-GBM is presented in Figure 33b. As can be seen in this figure, the depth of cracks from the UDEC-GBM does not reach the actual notch profile, meaning that this approach underestimates the depth of failure. Additionally, it can be discussed that contact failure in Figure 2-31b is most likely a representation of damage not failure since the rock strength in 205 MPa but the maximum tangential stress is 169 MPa. Therefore, failure cannot propagate to match the v-shaped notch failure around the MBE tunnel.

40
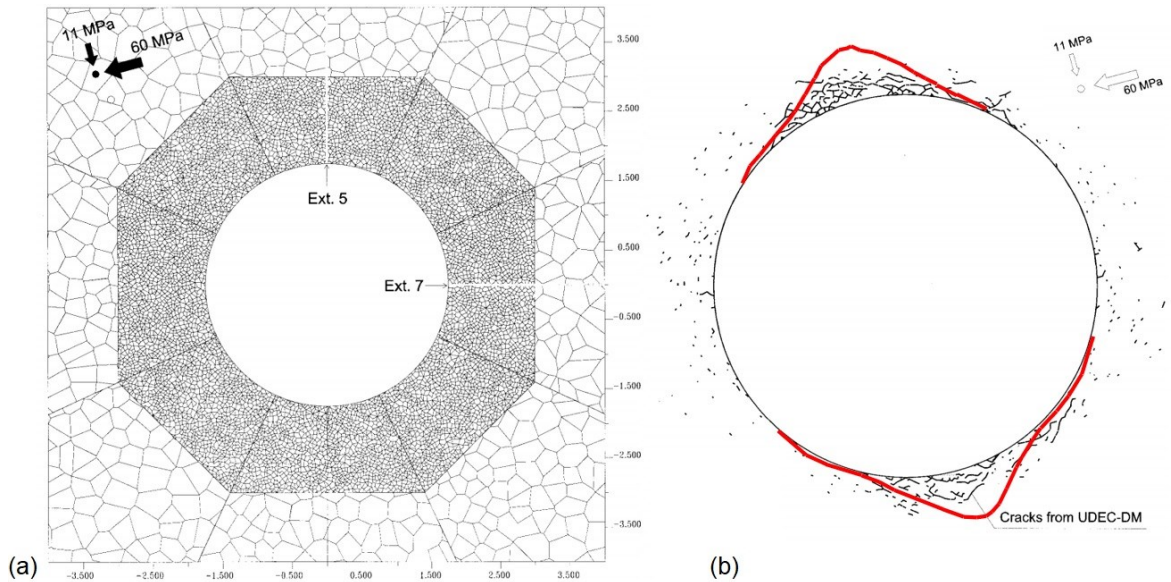
Figure 2-31 a) Simulated MBE tunnel with calibrated UDEC-GBM; b) development of damage around MBE tunnel (After Shin, 2010). Actual notch profile is added with red lines for comparison purposes

Azocar (2016) employed a GBM in 3DEC (Itasca Consulting Group Inc., 2014) to simulate brittle failure of LdB granite at the laboratory and in situ scales. The geometry of the grains in GBMs has essential influence on modeling results. To further investigate these potential effects, Azocar (2016) used Voronoi and tetrahedral blocks in his 3DEC-GBM. The grains in his models were assumed to be elastic and the micro-properties of the contacts were adjusted until the models were calibrated to intact LdB granite with a UCS of 200 MPa. The failure mechanism in UCS simulations showed that when the Voronoi tessellated model is used, tensile failure is more likely to occur. Conversely, in the model with tetrahedral blocks, shear failure was the dominant mode of the failure.

After calibrating the models, the MBE tunnel was simulated using both approaches. The numerical set up of the MBE tunnel is presented in Figure 2-32a and b. The results of the model with tetrahedral blocks with intact rock properties show that no damage developed at the top and bottom of the MBE tunnel and minor damage occurred near the sidewalls (Figure 2-32c). According to Azocar (2016), the Voronoi tessellated model also underestimated the DoF in the roof and floor of the tunnel and overestimated the damage in the sidewalls (Figure 2-32d) when the laboratory-scale calibrated micro-properties were used.

41
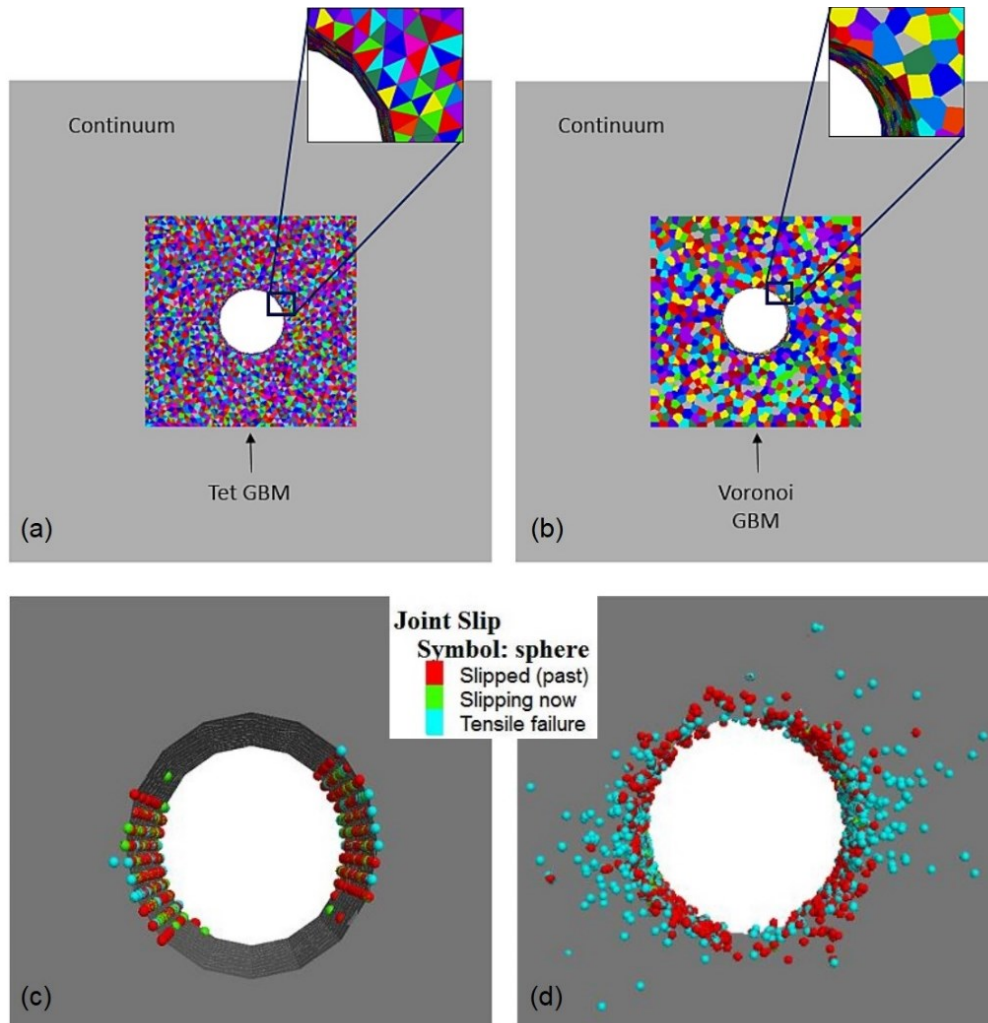
Figure 2-32 Numerical set up of MBE tunnel in 3DEC-GBM with: a) tetrahedral blocks; b) Voronoi blocks. Simulated depth of failure in MBE tunnel using: c) tetrahedral blocks; d) Voronoi blocks (after Azocar, 2016)

Azocar (2016) discussed that the tetrahedral model can capture the DoF if the micro-properties are re-adjusted, and if the large-scale model follows a suitable CWFS model. Therefore, by re-calibrating the model and decreasing the contact cohesive strength from 130 to 100 MPa, a more realistic depth of damage zone was obtained, as shown in Figure 2-33a. However, re-calibrating the micro-properties of the Voronoi tessellated model did not accurately capture the v-shaped failure (Figure 2-33b). Note that the re-calibration of the Voronoi tessellated model by Azocar (2016) was done by decreasing the tensile strength of the contacts from 60 to 40 MPa.
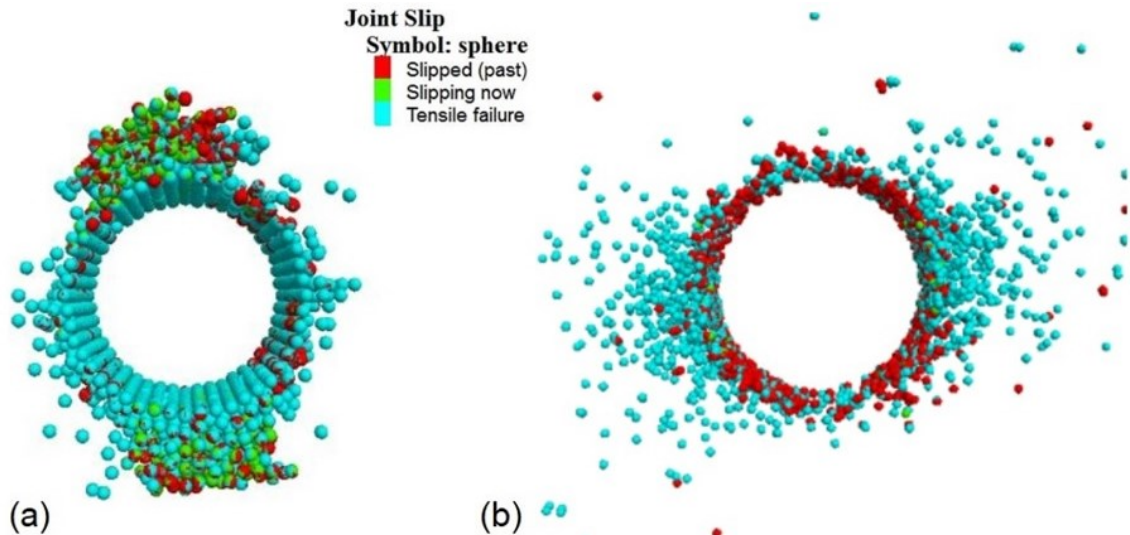
Figure 2-33 Simulated depth of failure in MBE tunnel using re-calibrated 3DEC-GBM with: a) tetrahedral blocks; b) Voronoi blocks (after Azocar, 2016)

2.5.3 Simulation of V-Shaped Notch Failure Using Hybrid Continuum-Discontinuum Approach

According to Hoek et al. (1995), hybrid approaches combine the continuum and discontinuum numerical methods to remove the limitations of each while keeping their advantages. The hybrid Finite-Discrete Element Method is a combination of continuum finite element and discontinuum discrete element methods (Li et al., 2019). In the FDEM, micro-scale damage leads to macro-scale behavior of the simulated material, hence, micro-properties need to be determined. An overview on the fundamentals and applicability of the FDEM can be found in Tatone and Grasselli (2015) and Li et al. (2019).

Vazaios et al. (2016) employed an approach utilizing the FDEM in Irazu (Geomechanica Inc, 2017) to simulate progressive brittle failure of hard, massive rock by modeling the MBE tunnel. The model was initially calibrated to a UCS of 213 MPa. However, they found that this calibrated model does not allow the brittle failure process to occur in the MBE tunnel simulation. Therefore, Vazios et al. (2016) re-calibrated the model to match the failure observed in the MBE tunnel, which leads to a back-calculated UCS of 119.5 MPa.

The results of the UCS test and MBE simulations based on the micro-properties of the re-calibrated Irazu model are shown in Figure 2-34a and Figure 2-34b, respectively.
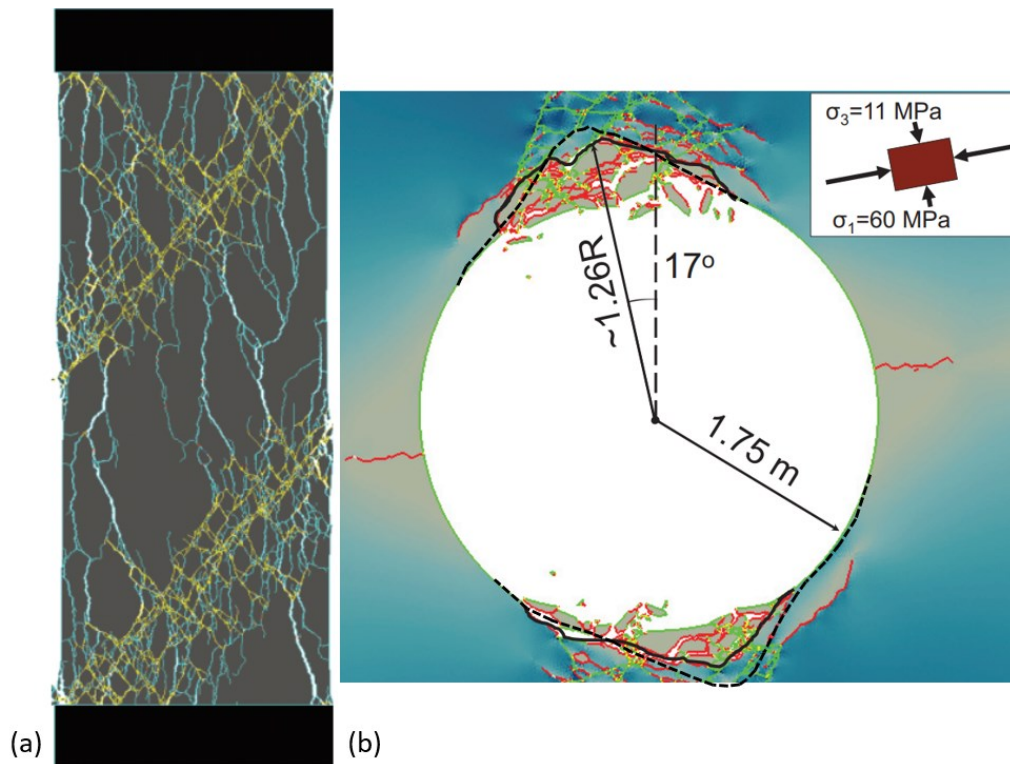
Figure 2-34 a) UCS test model in Irazu, (blue and yellow correspond to tensile and shear cracks, respectively); b) simulated failure of MBE tunnel using FDEM in Irazu (after Vazaios et al., 2016). Actual notch profile is added with black dashed line for comparison purposes.

The results of numerical simulation of the MBE tunnel using the calibrated model matches the EDZ around the test tunnel (Figure 2-34b). Vazaios et al. (2016) discussed that in this model, the initiation of fractures is due to tensile failure at the top and bottom notches, and shear fracturing dominates the higher confined area near the notch-tips. Thus, in addition to the DoF and EDZ, the failure mechanism is realistically captured around the MBE tunnel.

2.6   Summary

This chapter provided an overview of the excavation response experiments at the URL, focusing on the MBE tunnel, a 46 m long circular tunnel with a diameter of 3.5 m at the 420 m Level. The objective of this experiment was to investigate the characteristics of

excavation damage zone adjacent to an underground opening including the depth and extent of this zone. As discussed, predicting the behavior of rock mass is important in order to safely isolate the waste in a host rock. Amongst available options for the prediction of DoF and simulation of EDZ around underground openings, numerical methods are the tools that overcome many of the limitations of existing analytical and empirical approaches. Thus, a review of the numerical simulations of failure around the MBE tunnel was also provided in this chapter. A summary of the previous attempts to capture the depth and shape of v-shaped notch failure is presented in Table 2-3. It should be noted that various studies used different rock mass UCS, hence, these values are explicitly indicated in Table 2-3 for each study.

From the comprehensive literature review conducted in this chapter and summarized in Table 2-3 it can be concluded that the rock mass UCS used in a 2D model needs to be lower than the UCS of intact rock in order to be able to capture the DoF (Hajiabdolmajid et al., 2002; Cai and Kaiser, 2014; Diederichs, 2007; Potyondy and Cundall, 2004; Hazzard and Young, 2004; and Vazaios et al., 2019). Using the UCS of intact rock strength in 2D models leads to an underestimation of the DoF (Shin, 2010; and Vazios et al., 2019). As discussed by Bahrani et al. (2019), realistic simulations of spalling process leading to v-shaped notch failure most likely requires the application of the actual 3D stress path. Therefore, a 3D coupled continuum–discontinuum should be used to capture micro-cracking ahead of tunnel face and associated strength degradation, and thus, the DoF without the need to manually reduce the rock strength.

Table 2-3 Summary of numerical simulations of failure around MBE tunnel

Model description	Rock mass UCS (MPa)	DoF	SoF	EDZ	Failure mode	Reference
Continuum						
Elastic	128	Underestimated	✗	✗	✗	Hajiabdolmajid et al. (2002)
Elastic with monotonical removal of failed elements (FS < 1)	114	Overestimated	✗	✗	✗	Martin (1997)
Elastic-brittle with long-term strength	160	Underestimated	✗	✗	✗	Martin (1997)
Elastic-perfectly plastic	128	Underestimated	✗	✗	✗	Hajiabdolmajid et al. (2002)
Elastic-brittle	128	Underestimated	✗	✗	✗	Hajiabdolmajid et al. (2002)
Cohesive brittle frictional	70	Overestimated	✓	✗	✗	Martin (1997)
CWFS with FLAC2D	128	Estimated	✓	✗	✗	Hajiabdolmajid et al. (2002)
CWFS with FLAC3D	110	Estimated	✓	✗	✗	Rafiei Renani & Martin (2018)
Instantaneous CWFS with tunnel boundary irregularities	175	Estimated	✓	✗	✓	Cai and Kaiser (2014)
DISL	100	Estimated	✓	✗	✗	Diederichs (2007)
Discontinuum						
BPM (PFC2D)	120	Estimated	✓	✓	✓	Potyondy & Cundall (2004)
Dynamic BPM (PFC2D)	<120	Estimated	✓	✓	✓	Hazzard & Young (2004)
UDEC-GBM with elastic grains and CWFS for contacts	205	Underestimated	✗	✓	✗	Shin (2010)
3DEC-BBM with elastic grains and strain independent CWFS for contacts	<200	Estimated	✗	✓	✓	Azocar (2016)
Hybrid Continuum-Discontinuum						
FDEM (Irazu 2D)	119.5	Estimated	✓	✓	✓	Vazaios et al. (2016)

The objective of this research is to develop a VTM in a 2D continuum model to simulate brittle failure with reasonable failure mode around underground excavations, which is the focus of the following chapter. Based on the comprehensive literature review presented in this chapter, it is expected that a strength reduction is necessary for simulating the DoF and SoF in a 2D VTM.

Chapter 3 A 2D Continuum-Based Voronoi Tessellated Model (VTM) for Lac du Bonnet Granite

3.1   Introduction

As reviewed in Chapter 2, different methodologies have been developed to simulate the DoF, SoF and EDZ around the MBE tunnel, including the DISL model proposed by Diederichs (2003). In this chapter, the application of the DISL model in simulating the failure modes of brittle rocks under laboratory loading conditions is investigated. It is discussed that heterogeneous models are more suitable to simulate the brittle failure process compared to homogeneous models. Next, RS2 is used to simulate the laboratory behavior of intact (undamaged) LdB granite and the v-shaped notch failure around the MBE tunnel. For this purpose, a continuum-based heterogeneous model, in which the numerical specimen consists of several randomly generated polygonal blocks separated by block boundaries, is developed. This model called Voronoi Tessellated Model (VTM), is calibrated to the laboratory properties of intact LdB granite. The calibrated VTM is then used to simulate the MBE tunnel to further investigate the capabilities of the proposed modeling approach for simulating the damage and failure around the MBE tunnel.

3.2   The Finite Element Method

RS2 (version 10), which is a two-dimensional numerical program based on the Finite Element Method (FEM), was used in this research. The FEM is one of the most popular numerical methods in rock mechanics and rock engineering. It is commonly used to simulate underground excavations in rocks (Hoek et al., 1995). In this method, the material (e.g., rock mass) is treated as a continuum medium and is discretized into several smaller regularly shaped elements connected to adjacent elements and the model boundaries at their nodes. There are four different element types in RS2: 3-noded triangular, 6-noded triangular, 4-noded quadrilateral, and 8-noded quadrilateral

elements. The steps to calculate the stresses and corresponding strains in the FEM can be summarized into five stages (Pande et al. 1990):

1. Discretization of domain: the continuum medium is divided into several smaller elements.

2. Calculation of strain within each element: the displacement over an element is estimated with a trial function of the nodal displacements, which must satisfy its governing probabilistic density function.

3. Derivation of stiffness matrix: a stiffness matrix is derived from the material and geometric properties of an element using the principle of the minimum potential energy.

4. Assembling of global algebraic equations: a global stiffness matrix is assembled from individual element stiffness matrices.

5. Calculation of stresses and strains: the corresponding stresses and strains are calculated from global displacements.

There are different material models available in RS2, such as the Mohr-Coulomb and Hoek-Brown models. In this research, the Mohr-Coulomb model was used for both mesh and joint elements. The Mohr-Coulomb model in RS2 is an elasto-brittle-plastic material model (Rocscience, 2021). This means that RS2 accepts peak and residual values for the strength properties (i.e., cohesion and friction angle). After the initial yielding, the strength of the material instantly drops from its peak state to a lower residual state. In the case where the residual values are the same as peak values, the behavior is elastic perfectly-plastic. In RS2, the dilation angle should be less than or equal to the residual friction angle, which makes the flow rule non-associated or associated, respectively (Rocscience, 2021). In this research, a dilation angle of zero was used in all RS2 models. RS2 also accepts peak and residual values for the tensile strength. The flow rule for tensile strength is associated.

The joint element in RS2 is a one-dimensional 4-noded quadrilateral element with a negligible thickness (Riahi et al., 2010). It is an edge-to-edge contact in which interconnectivity does not change with time. Figure 3-1 presents the configurations of a

joint element before and after deformation. As can be seen in this figure, the two sides of the joint element have equal lengths. Before deformation occurs (Figure 3-1a), nodes 1 and 4 of the joint element share the same position, while nodes 2 and 3 share another position. When the blocks start to deform (Figure 3-1b), the nodes can move normally and tangentially from each other. According to Riahi et al. (2010), displacement, rotation, or strains of discrete objects can be accommodated by the joint element so long as these mechanisms do not change contacting node couples.
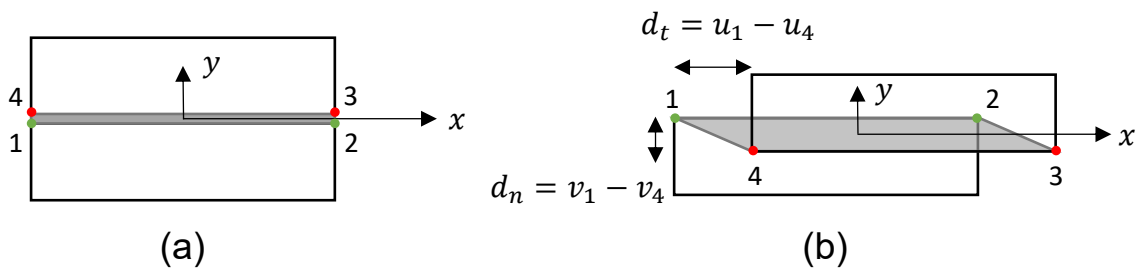
Figure 3-1 Interpretation of finite element interface (joint element) in RS2 (after Riahi et al., 2010, and Li and Bahrani, 2020a): a) undeformed joint element; and b) deformed joint element.

The joint elements in RS2 are assigned strength and stiffness properties. Relative movements of the two sides of a joint may be elastic or inelastic. Inelastic joints with perfectly plastic or brittle post-peak response can be simulated by assigning a failure criterion (e.g., Mohr-Coulomb, Barton-Bandis, etc.) and appropriate residual strength values, to allow for shear (slip) or tensile yielding between the two discrete bodies. The residual strength parameters will be in effect if joint slip or tensile yielding occurs (i.e., peak strength envelope is exceeded). For example, in the Mohr-Coulomb model, if the shear stress on a joint element exceeds the joint peak shear strength, slip (or shear yielding) occurs, and the cohesion and friction angle of the joint element are reduced to their residual values. Similarly, if the normal stress on a joint element exceeds the joint peak tensile strength, tensile yielding occurs, and the tensile strength of the joint element is reduced to its residual value. Note that since the FEM assumes that the domain is continuous, joint elements cannot experience detachment. The detachment is simulated by a reduction in post-peak normal stiffness of the joint element. In this research, it was assumed that joint tensile yielding reduces the joint stiffness by a factor of 0.01.

3.3 Simulation of Brittle Failure Using Continuum Homogeneous Models

Hoek and Brown (1997) introduced their non-linear failure criterion in an attempt to provide input data for the design of underground excavations in rock masses. Since many researchers and practitioners still use the linear Mohr-Coulomb criterion for excavation designs and many geotechnical software programs are developed based on this criterion, it is necessary to determine equivalent friction angles and cohesive strengths for each rock mass and stress range (Hoek and Brown, 2002). This is done by fitting a linear relationship to the Hoek-Brown curve for a range of minor principal stress (σ_3). Hoek et al. (2002) have developed guidelines that can be used to determine the upper limit of confining stress (σ'_{3max}) for different applications (e.g., deep tunnel, shallow tunnel and slopes). The σ'_{3max} value can then be used to determine the equivalent linear Mohr-Coulomb envelope (i.e., friction angle and cohesion). In this section, an alternative approach is used to determine the σ'_{3max} value. First, a homogeneous elastic model of the MBE tunnel is constructed, and the σ_3 around the tunnel is monitored. The maximum σ_3 value near the tunnel boundary is used as the upper bound of the confining stress to determine the equivalent Mohr-Coulomb parameters, which will then be considered for the calibration of heterogeneous models.

3.3.1 Analysis of Elastic Stresses Around MBE Tunnel

In this section, a 180 m × 180 m homogeneous elastic model fixed on all sides is used to monitor the induced stresses around the MBE tunnel. Figure 3-2 shows a close view of the 2D plane strain homogenous model of the MBE tunnel. Six-noded triangular elements were used to mesh the model. The mesh size was chosen in such a way that the minor principal stress at the tunnel boundary would drop to approximately zero following the excavation of the tunnel. The maximum tangential stress was found to be 169 MPa, which is consistent with that obtained from the Kirsch equations (i.e., $\sigma_{max} = 3\sigma_1 - \sigma_3 = 3 \times 60 - 11 = 169$ MPa). Figure 3-2 illustrates the contours of the major (σ_1) and minor principal stresses around the tunnel.
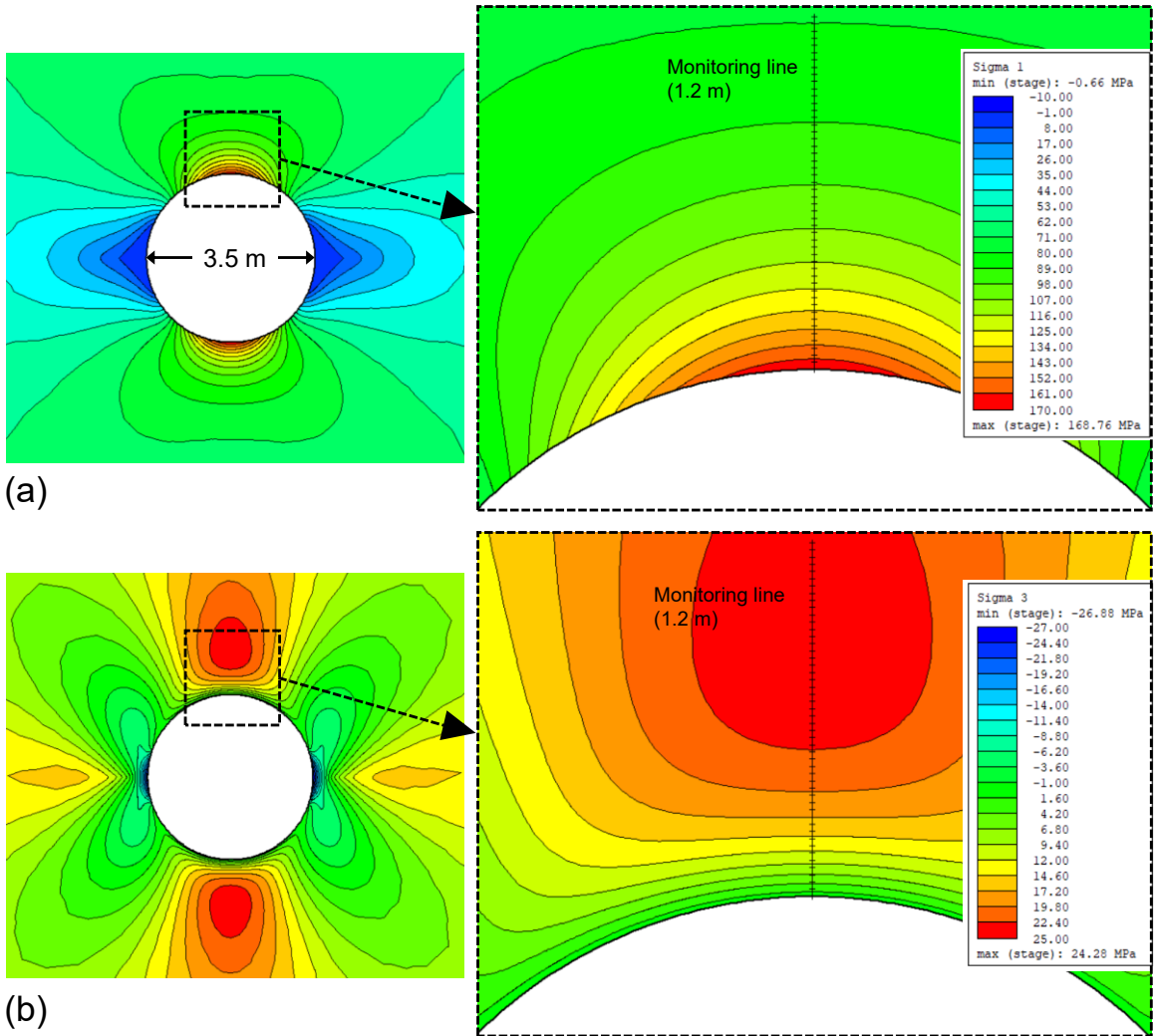
Figure 3-2 Elastic stresses around MBE tunnel obtained from a homogeneous elastic model in RS2: a) major principal stress; and b) minor principal stress

A monitoring line shown in Figure 3-2 was used to extract the induced stresses as a function of distance from the excavation wall. Figure 3-3 shows the stresses along side the monitoring line. It can be observed in this figure that the maximum value of σ_3 around the MBE tunnel is approximately 25 MPa. Therefore, this value can be used as the upper limit of the confining stress (i.e., σ'_{3max}) to determine the equivalent Mohr-Coulomb strength parameters and for the calibration of heterogeneous models.
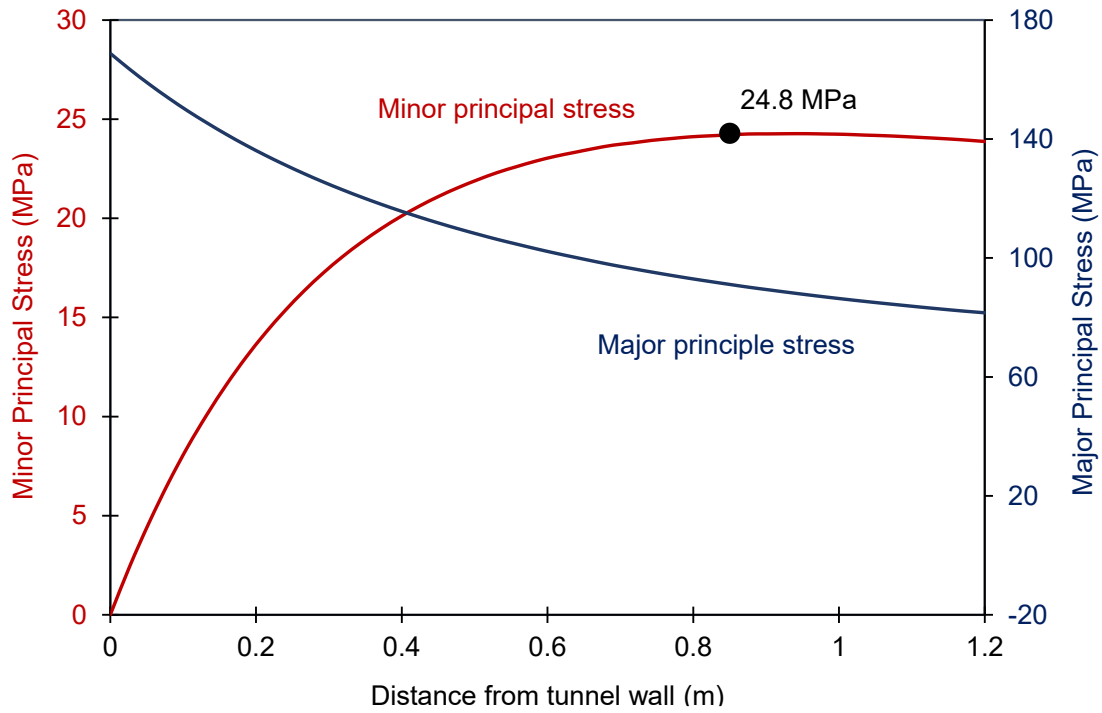
Figure 3-3 Major and minor principal stresses along monitoring line shown in Figure 3-2 following the excavation of tunnel, obtained from a homogeneous elastic model in RS2

Figure 3-4 shows the HB strength envelope fitted to the results of laboratory triaxial tests on intact LdB granite. Two equivalent Mohr-Coulomb envelopes are fitted to the non-linear HB envelope, one for a σ'_{3max} value of 25 MPa and the other for a σ'_{3max} value of 60-MPa. It is shown that the unconfined compressive strength (203 MPa) obtained for the σ'_{3max} value of 25 MPa is closer to the average UCS of LdB granite, which is 213 MPa. For this reason, the Mohr-Coulomb parameters corresponding to the confinement range of 0 to 25 MPa is used for model calibration.
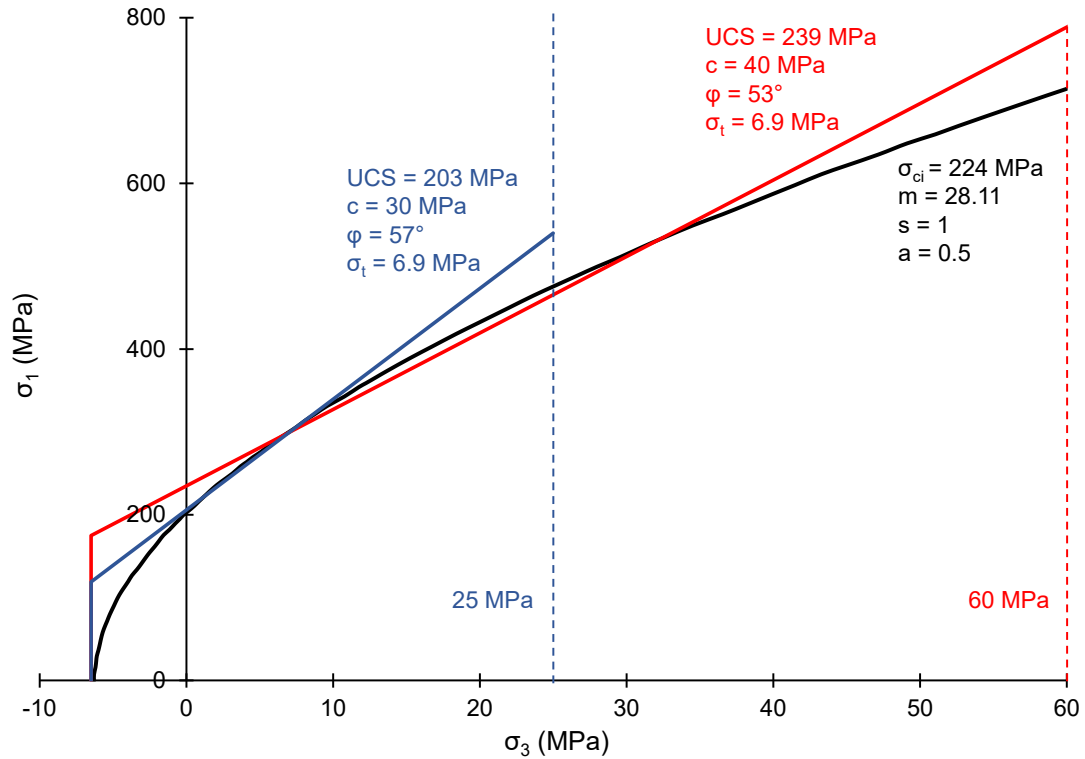
Figure 3-4 Non-linear HB strength envelope fitted to results of laboratory triaxial tests on LdB granite and corresponding equivalent Mohr-Coulomb envelopes for confinement ranges with σ'_{3max} values of 25 and 60 MPa

Figure 2-10a shows the profiles of the MBE tunnel as the v-shaped notch was progressively developed over a period of several months. In an attempt to better understand the evolution of stresses around the test tunnel during its excavation and progressive formation of the v-shaped notch failure, a homogenous elastic model of the tunnel was constructed in RS2. In this model, the progressive failure around the test tunnel was simulated by manually excavating slabs in seven stages, as shown in Figure 2-10b to g. Stage 1 corresponds to the application of the far-field stresses (i.e., $\sigma_1 = 60$ MPa, $\sigma_3 = 11$ MPa, $\sigma_2 = 45$ MPa). At Stage 2, the tunnel core is excavated (Figure 2-10b). Stages 3 to 7 correspond to the tunnel profiles observed in the field:

- Stage 3: tunnel profile on Dec. 23, 1991 (Figure 2-10c);
- Stage 4: tunnel profile on Jan 15, 1992 (Figure 2-10d);
- Stage 5: tunnel profile on Feb 26, 1992 (Figure 2-10e);
- Stage 6: tunnel profile on Mar 2, 1992 (Figure 2-10f); and
- Stage 7: final v-shaped notch profile on Aug 7, 1992 (Figure 2-10g).

54
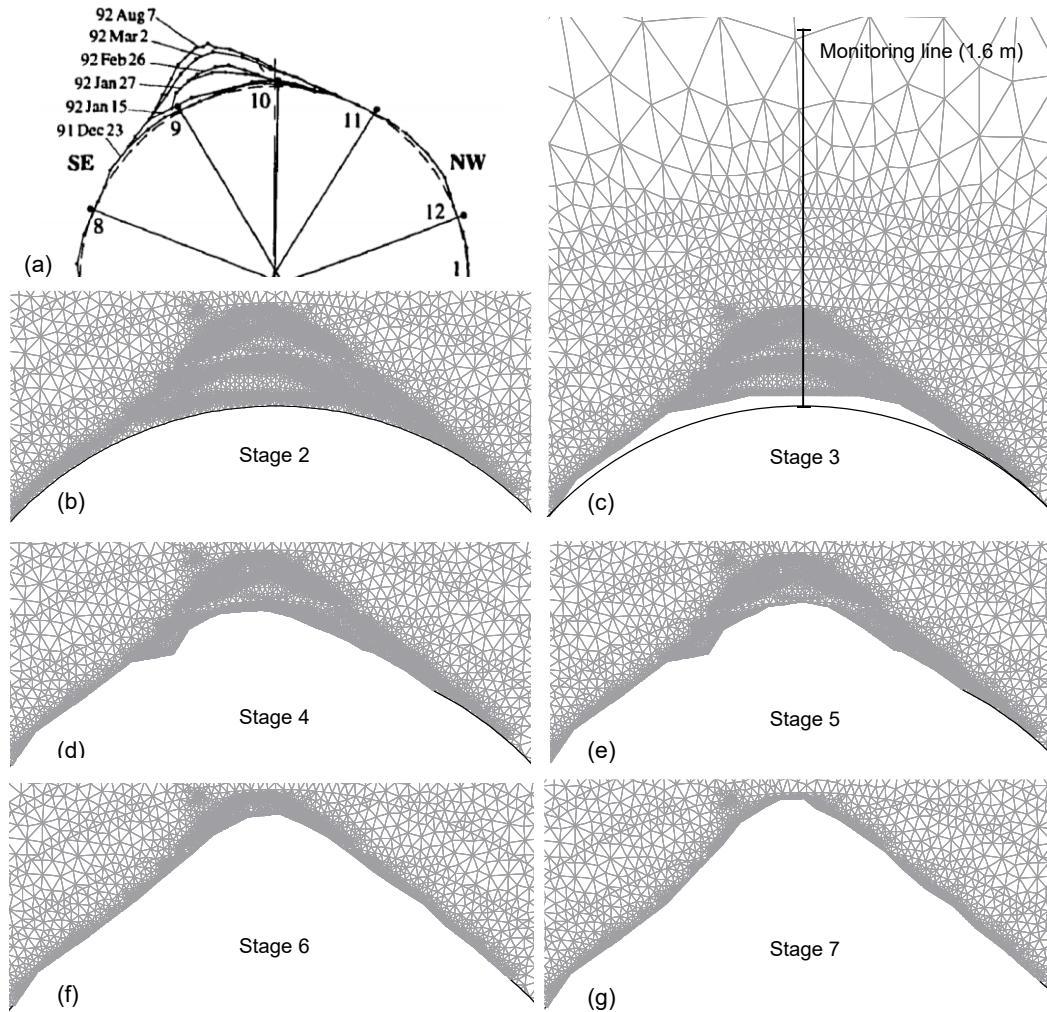
Figure 3-5 Simulated MBE tunnel using an elastic homogeneous model in RS2 considering progressive detachment of rock slabs as observed in the field: a) Stage 2 (excavation of circular tunnel) (Read & Martin, 1996); b) Stage 3 (tunnel profile on Dec. 23, 1991); c) Stage 4 (Jan 15, 1992); d) Stage 5 (Feb 26, 1992); e) Stage 6 (Mar 2, 1992); and f) Stage 7 (final v-shaped notch profile on Aug 7, 1992)

The excavation-induced elastic stresses along the monitoring line shown in Figure 3-5c were plotted as a function of distance from the excavation boundary for all the excavation stages shown in Figure 3-5. The results, including σ_1 and σ_3 distributions along the monitoring line, are presented in Figure 3-6a and b, respectively. It can be seen in Figure 3-6a that σ_1 increases near the tunnel boundary as the slabs are removed from Stage 2 to Stage 7 up to approximately 375 MPa near the tip of the v-shaped notch. Figure 3-6b shows that the confinement is zero at the tunnel boundary after each round of slab removal. The confinement increases rapidly away from the excavation boundary to around 68 MPa near the tip of the notch at Stage 7. It can be discussed that the

55

stabilization of the failed zone (i.e., v-shaped notch) could be related to the sudden increase in the confinement (Figure 3-6b), which inhibited the propagation of cracks formed near the tip of the v-shaped notch (see Figure 2-8c).

(a)

(b)
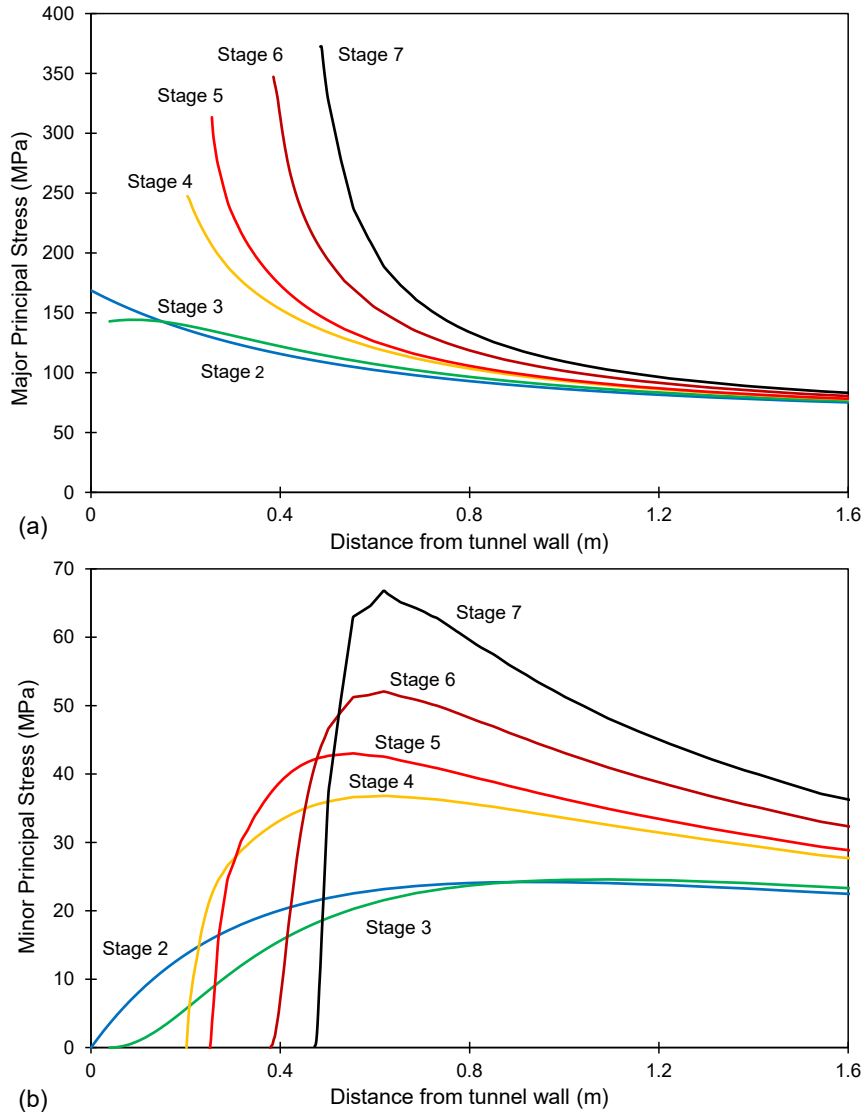
Figure 3-6 Elastic stresses as a function of distance from tunnel wall after removal of failed slabs around the tunnel shown in Figure 3-5: a) σ_1; and b) σ_3

3.3.2 DISL Model

According to Diederichs (2003), the conventional shear-based failure criteria do not consider the tensile-induced micro-cracking at low confinement (e.g., near tunnel

boundaries). Accordingly, a multi-phase failure criterion such as the DISL model (shown in Figure 2-23a) can be used to differentiate the failure initiation at low confinement from shear-dominated failure at high confinement. Such a constitutive law allows the onset of failure to occur at a stress level that is lower than the UCS of intact rock (i.e., crack initiation). In this approach, the elements start to yield in shear when the maximum tangential stress around the tunnel exceeds the rock mass strength defined by the crack initiation stress level. The failure propagates away from the tunnel wall until the induced stresses reach higher confining pressures (i.e., spalling limit) when the final failure profile (i.e., v-shaped notch) is formed. Figure 3-7 shows that even though the DISL model captures the observed DoF and SoF, the simulated failure mechanism is not consistent with field observations shown in Figure 2-22. As described by Martin (1997), the failure mode near the MBE tunnel was spalling, which is caused by the development of visible tensile fractures under a compressive stress state near the excavation boundary.
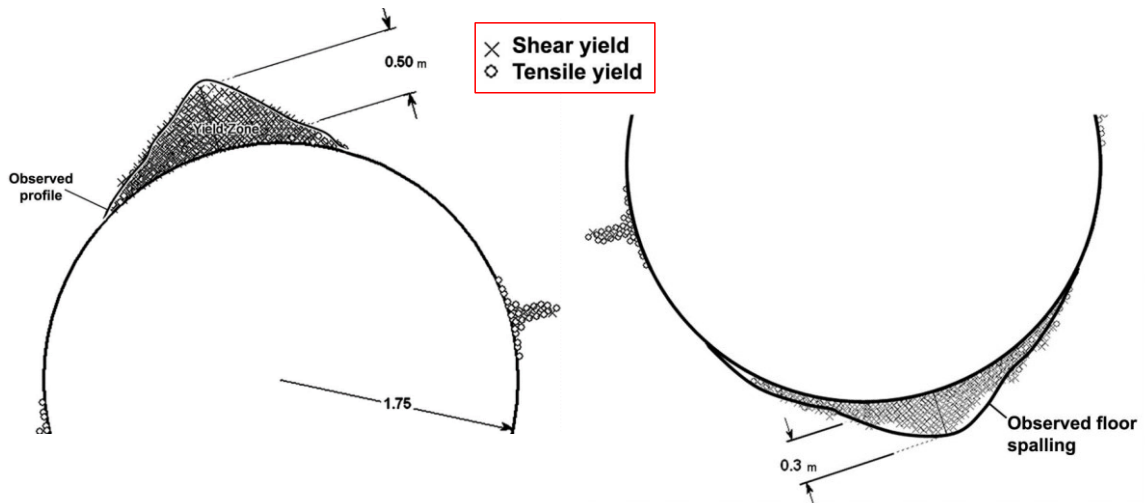
Figure 3-7 Simulated failure around MBE tunnel using DISL model in Phase^2 (after Diederichs, 2007)

In this section, the application of the DISL model in capturing the failure mechanism of brittle rocks is further investigated. For this purpose, standard rock mechanics laboratory tests including the BTS, DTS, UCS and confined compression tests were simulated. In these numerical simulations, the input parameters were set to be the same as those suggested by Diederichs (2007) for LdB granite.

Ideally, full 3D models should be used when simulating laboratory tests to ensure that the boundary conditions in the simulations are consistent with those in the actual tests. However, previous studies (e.g., Shin, 2010; Lan et al., 2010; Valley et al., 2010; Gao et al., 2016; Vazaios et al., 2019; Qi et al., 2019; Sinha & Walton, 2020; Li & Bahrani, 2021a) show that a 2D plane strain model can also be used for this purpose. In this section, a 1.2 m × 0.6 m rectangular-shaped plane strain model was developed in RS2 to simulate the UCS, DTS and confined compression tests (Figure 3-8). All the models were meshed using six-noded triangular elements with an average edge length of 18 mm. Figure 3-8a illustrates the boundary conditions for the UCS test simulations. As can be seen in this figure, the lower boundary of the UCS model was fixed in the vertical direction except for the midpoint, which was fixed in both vertical and horizontal directions to restrain lateral movement of the specimen during loading. The specimen was loaded by applying a constant displacement to the top boundary of the model.

In the DTS test, a constant displacement was applied in an upward direction to the top model boundary, as shown in Figure 3-8b. For the simulation of the Brazilian test, the top and bottom of the Brazilian disk were flattened following the suggestion by Wang et al. (2004). In this test, a constant displacement was applied to the top boundary of the model (Figure 3-8c). The confined compression tests were simulated for confining pressures of 5, 10, 15, 20 and 25 MPa. To simulate these tests, a constant stress was first applied to the model boundaries (except for the bottom boundary) to mimic the hydrostatic confining pressure (Figure 3-8d). At later stages, a displacement boundary was applied to the top boundary of the model to simulate axial loading.

Note that the boundary conditions used to simulate laboratory tests in this study are consistent with those of Valley et al. (2010), Bewick et al. (2012) and Li and Bahrani (2021a). It should be mentioned that it is also possible to consider the upper and lower platens in the simulations, similar to the work by Gao et al. (2016), who used UDEC to simulate laboratory compression tests.
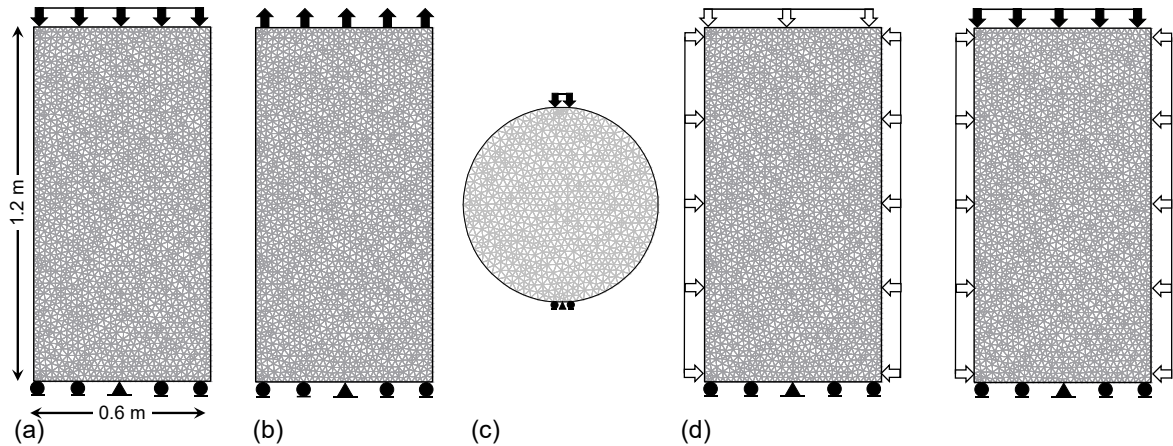
Figure 3-8 Simulated laboratory tests using homogeneous models in RS2: a) UCS test; b) DTS test; c) BTS test; and d) confined compression tests. Black and white arrows represent applied displacement and stress, respectively. Note: specimen width is 0.6 m.

The strength envelope obtained from the laboratory test simulations, along with the input peak and residual strength envelopes, and the stress-strain curves for the DISL model are presented in Figure 3-9a and b. As expected and shown in Figure 3-9a, the emergent strength envelope is bi-linear. Figure 3-9b shows that at low confinement, the post-peak response is brittle. However, it becomes perfectly plastic as the confining pressure increases. This can be attributed to the fact that the residual strength is less than the peak strength at low confinement (σ_3 < 18 MPa), becomes the same as the peak at σ_3 = 18 MPa, and exceeds the peak strength at higher confinements (σ_3 > 18 MPa).
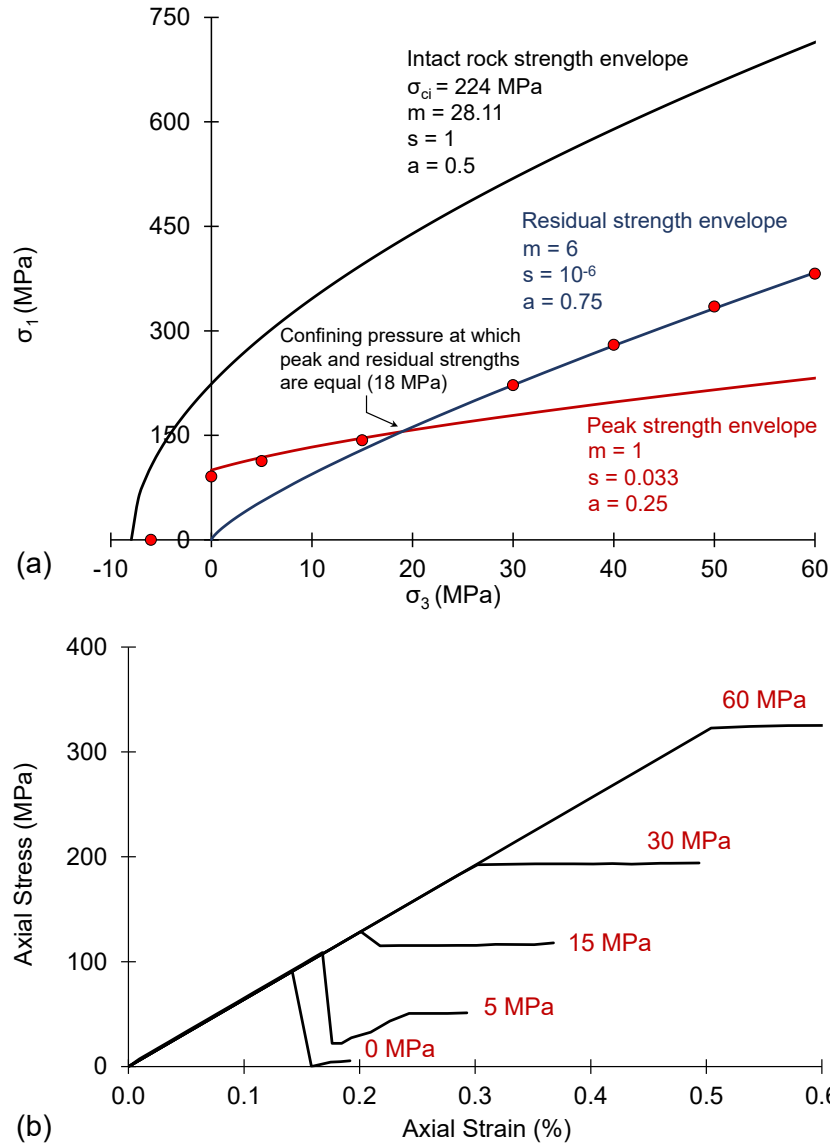
Figure 3-9 a) Peak and residual strength envelopes in DISL model and the emergent strength envelope from simulated laboratory tests; and d) stress-strain curves of simulated compression tests using DISL model

Figure 3-10 shows the failure modes of the simulated laboratory tests using the DISL model. As expected, all the elements in this homogenous model yield simultaneously in shear following the peak stress. This is because the homogeneous model consists of finite elements with the same properties; thus, localized tensile stresses and pre-peak yielding leading to axial splitting in the UCS test (Figure 3-10a), localized tensile failure in the DTS test (Figure 3-10b) and shear band formation in the confined compression tests (Figure 3-10c) are not captured. The non-uniform yielding in the BTS test (Figure 3-10d) captured

by the homogeneous model can be related to the specimen geometry, the boundary conditions, and the non-uniform mesh elements across the numerical specimen.
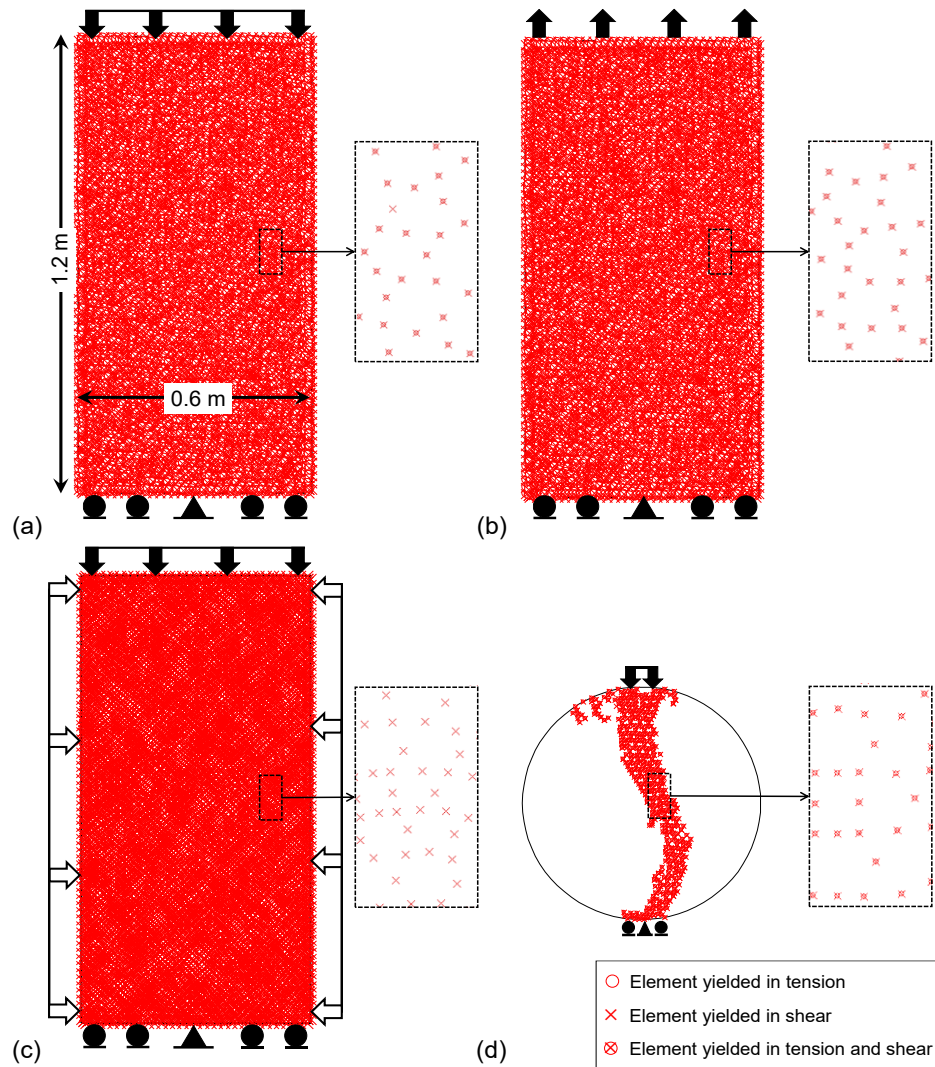
Figure 3-10 Failure modes of simulated laboratory tests using homogeneous DISL model in RS2: a) UCS test; b) DTS test; c) confined compression test; and d) BTS tests. Black and white arrows represent applied displacement and stresses, respectively.

3.4   Simulation of Brittle Failure Using Continuum Heterogeneous Models

It is known that the macroscopic behavior of a crystalline rock subjected to loading is controlled by its micro-structure and grain-scale heterogeneities. According to Lan et al.

61

(2010), there are different types of grain-scale heterogeneities: 1) grain geometric heterogeneities arising from different grain shapes and sizes; 2) grain property heterogeneities arising from the difference between strength and deformation properties of different mineral grains; and 3) grain boundary heterogeneities arising from the difference in strength, stiffness, length and orientations of grain boundaries.

Different types of heterogeneities can be implemented into numerical models to simulate the brittle failure process. In general, the objectives of using heterogeneous numerical models include capturing: 1) pre-peak fracturing due to localized tensile stresses; 2) non-linear stress-strain curve due to crack closure; 3) realistic tensile to compressive strength ratio (i.e., 0.05 in hard brittle rocks); 4) transition of failure mode from axial splitting at low confinement to shear failure at high confinement; 5) change in the stress-strain response from brittle to strain hardening with increasing confinement; and 6) non-linear strength envelope.

Gao et al. (2010) summarised the numerical methods commonly used to simulate the micro-structure of crystalline rocks in terms of geometric and contact heterogeneities into four groups: 1) disk-shaped elements (e.g., PFC by Potyondy & Cundall, 2004); 2) square-shaped elements (e.g., RFPA2D by Tang & Kaiser, 1998; and FLAC by Fang and Harrison, 2002); 3) triangular elements (e.g., Irazu by Vazaios et al., 2019; and UDEC by Gao & Stead, 2014); and 4) polygonal elements (e.g., UDEC by Lan et al., 2010, and Sinha & Walton, 2020). Figure 3-11 shows an example of the mineral grain structure for LdB granite. Lan et al. (2010) discussed that Voronoi tessellations can be used to realistically simulate the brittle failure process, as the generated polygons are appropriate representations of the micro-structure of crystalline rocks.

4 mm
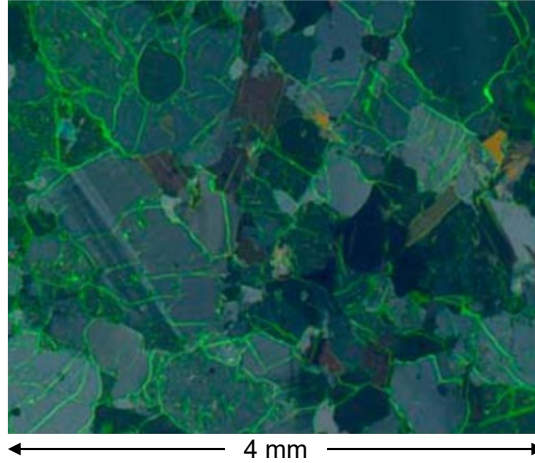
Figure 3-11 Grain structure of LdB granite observed in polarized light thin section (Lan et al., 2010)

Various researchers have simulated the failure process of brittle rocks using heterogeneous models developed in discontinuum programs reviewed above (e.g., Shin, 2010; Lan et al. 2010; Potyondy & Cundall, 2004; Gao et al., 2016; Bahrani & Kaiser, 2017; Wang & Cai, 2018; Qi et al., 2019; Sinha & Walton, 2020). Valley et al. (2010) used a heterogeneous continuum model to study the influence of stiffness heterogeneity on internal stress paths, localized tensile stress and post-peak response during compressive loading. They used a 2D FEM model to simulate unconfined and confined compression tests. The heterogeneity in these models was limited to variability in the Young's modulus of finite elements (i.e., stiffness heterogeneity). Using this heterogeneous model, they captured pre-peak localized tensile stresses within the numerical specimens. Although this approach allowed for capturing pre-peak damage and tensile yielding at low confinement and shear failure at high confinement, the simulated macroscopic failure mode at low confinement was not axial splitting, and the emergent strength envelope was found to be linear.

A typical approach is to assume that the blocks/grains within the numerical specimen are elastic; therefore, failure can only happen along the boundaries (Shin, 2010; Lan et al., 2010; Wang & Cai, 2018). This approach is mostly used in discontinuum codes such as UDEC and 3DEC. Bewick et al. (2012) used a continuum grain-based model with elastic grains and grain boundaries and studied the effects of grain geometric heterogeneity on the tensile stress generation within the specimens under compression. They concluded

that the grain boundary orientation has a significant impact on the generation of localized tensile stresses. Markus (2019) used RS2 to generate grain-based models with elastic blocks (grains) and inelastic block boundaries (grain boundaries). They found that heterogeneous models created with elastic blocks do not capture the post-peak response. They used Voronoi and trigon tessellations to develop RS2-GBMs and compared the simulation results with those of FDEM models, as shown in Figure 3-12.
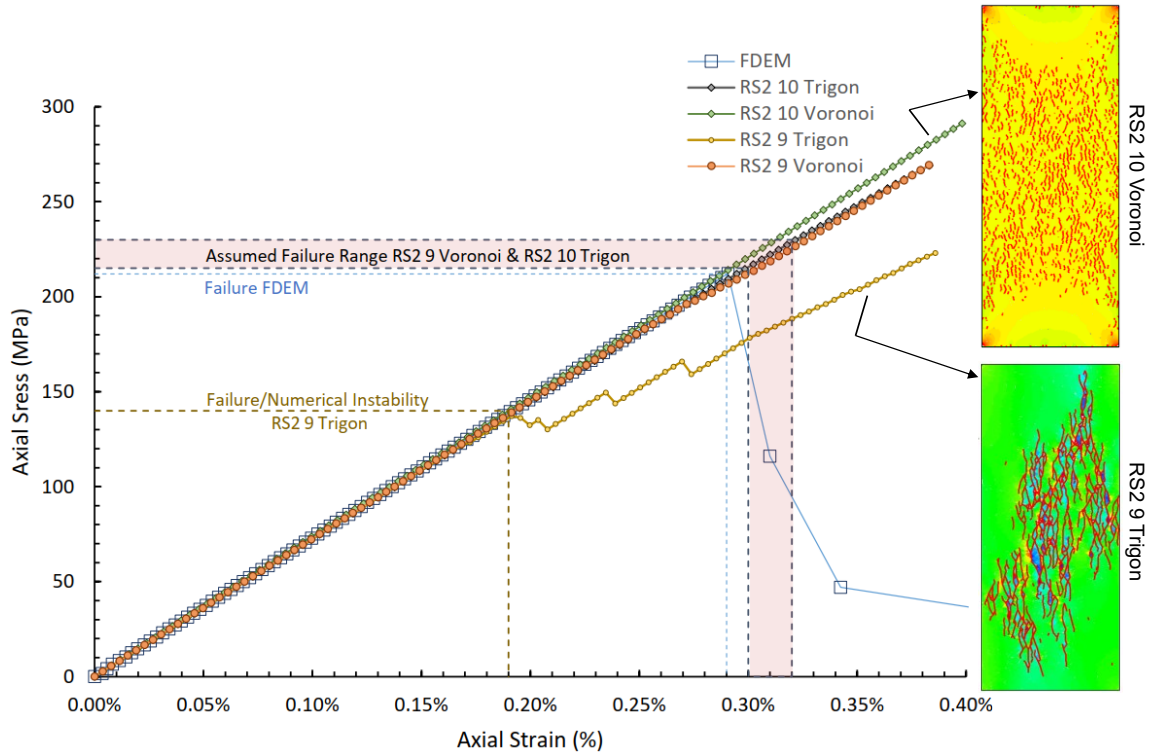
Figure 3-12 Comparison of UCS test simulations in RS2 versions 9.0 and 10.0 using Voronoi- and trigon-based models with those of FDEM models in Irazu (after Markus, 2019)

Figure 3-12 compares the results of numerical simulations using different versions of RS2 with FDEM models. Markus (2019) reported that non-convergence errors occurred when the trigon- and Voronoi-based models were used in RS2 version 9 (RS2 9). However, the RS2 version 10 models reached a converged solution, and no stress drops occurred past the peak stress. They assumed that the non-convergence error occurred at an axial stress of 140 MPa in the RS2 9 Voronoi-based model (Figure 3-12) is an indication of failure. Figure 3-12 shows that only the RS2 9 trigon-based model replicated the stress drop. The region selected as the 'assumed failure range' in Figure 3-12 for RS2 9 Voronoi-based and

RS2 10 trigon-based models was chosen solely because of the aggregation of contact yielding and not based on the stress-strain response.

To overcome the limitations described above, Li and Bahrani (2021) developed a heterogeneous model in RS2 with inelastic blocks (grains) and block boundaries (grain boundaries) to simulate intact and heat-treated Wombeyan marble. Using this approach, they were able to capture the pre-peak damage, the observed post-peak response, realistic macroscopic failure modes, and non-linear strength envelope. The simulated stress-strain response of the grain-based model of intact marble is shown in Figure 3-13.
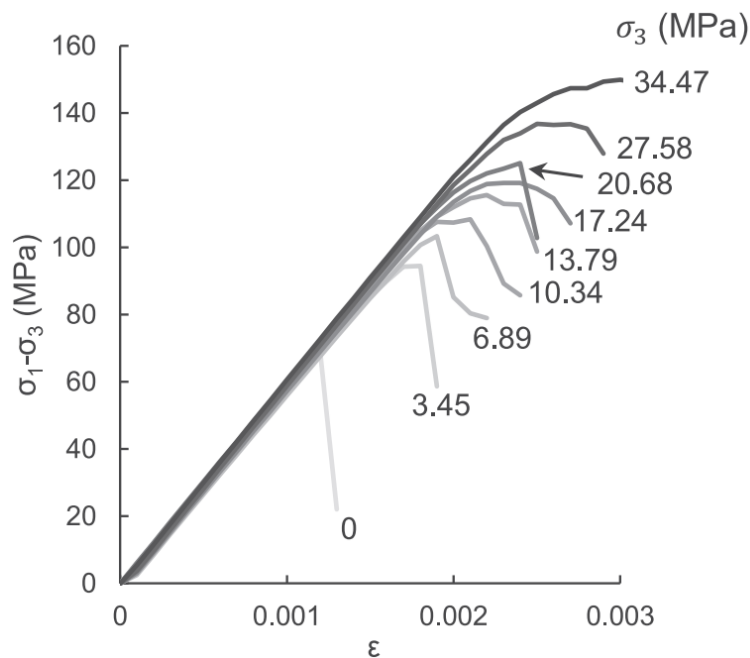
Figure 3-13 Stress-strain response of RS2-GBMs of intact Wombeyan marble (after Li and Bahrani, 2021)

Figure 3-13 shows that by using inelastic properties for both grains and grain boundaries, the observed transition in the stress-strain response of brittle rocks can be realistically simulated. At low confinement, the stress-strain response of the RS2-GBM is brittle, and a transition from brittle to strain-hardening behavior can be seen as the confinement increases. In the following sections, a similar approach is used to further explore the advantages and limitations of the continuum-based heterogeneous models in capturing the behavior of brittle rocks under laboratory and field loading conditions.

3.4.1 Continuum-Based Voronoi Tessellated Model

The joint network option in RS2 allows for simulating patterns of natural geological structures at different scales. Various joint network models available in RS2 include parallel (deterministic and statistical), cross jointed, Baecher, Veneziano, and Voronoi. Among them, the Voronoi joint network has been used to simulate the granular structure of brittle rocks (e.g., Li and Bahrani, 2021) and large-scale rock mass heterogeneities (e.g., Kaiser et al. 2016; Day et al., 2019).

The construction process of the Voronoi Tessellated Model (VTM) in RS2 used in this study can be summarised in three steps, as described below:

1. Create an initial VTM for a UCS specimen to determine the proper joint length and block size. Note that the size of the UCS specimen should be chosen with respect to the scale of the problem (i.e., block size is not the same as grain size for large scale excavations such as a tunnel).
2. Generate a Voronoi joint network with joint length and block size determined from the previous step into the MBE tunnel model in such a way that the heterogeneous domain (i.e., VTM) covers the area where failure is expected.
3. Carve rectangular and disk-shaped specimens from the heterogeneous domain. These specimens will be used to simulate the laboratory tests (i.e., compression and tensile tests).

In RS2, the generation of the Voronoi joint network requires an average joint (or contact) length. Based on the suggestion by the ISRM (1979), the width of the specimen should be at least ten times larger than the largest grain of the rock. As a starting point (i.e., the first step of model construction), the average joint length was chosen to be 26 mm, which resulted in at least ten blocks across the width of the rectangular-shaped specimen. The joint end condition was selected to be 'open'. This means that each end of the joint element, which is represented by two nodes in the finite element mesh, can move with respect to each other (Rocscience, 2021). Figure 3-14 shows the initial VTM developed to determine the average joint length and block size.
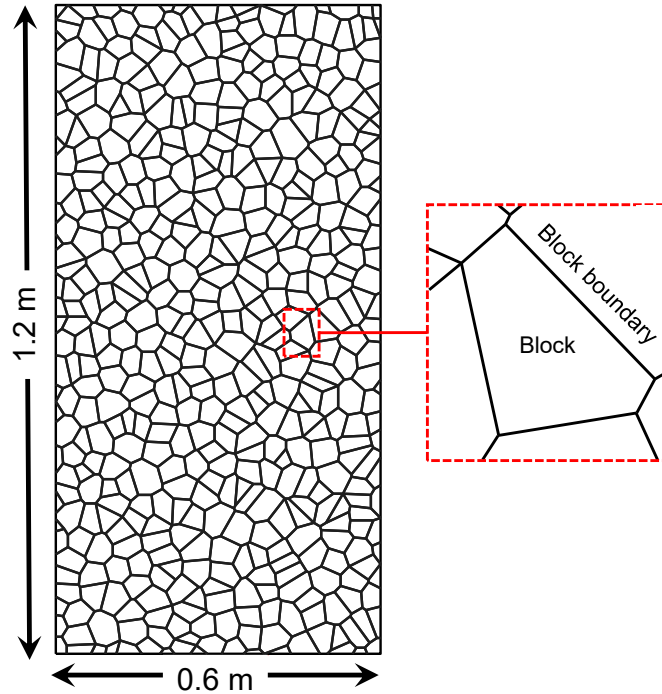
Figure 3-14 Initial VTM developed in RS2 to determine average joint length showing a close view of blocks and block boundaries

It should be noted that the blocks and block boundaries in this model represent the general behaviour of the grains and grain boundaries of the heterogeneous LdB granite but at an increased scale. This allows for general micro-mechanical behavior to be replicated without prohibitive computational effort. Therefore, in this study, the Voronoi joint network was mainly used as a means to implement geometrical heterogeneities into the continuum model to allow for the generation of localized tensile stresses and, consequently, pre-peak tensile damage within a specimen under an overall compressive stress field.

According to Read (2004), the EDZ around the MBE tunnel was limited to 1 m away from the tunnel wall according to results from underground characterization, geophysics surveys and acoustic emission studies. Based on this information, the RS2 model of the MBE tunnel was divided into two domains (i.e., heterogeneous and homogeneous) to reduce the computation time. In the second step of model construction, the built-in Voronoi DFN generator with an average joint length of 26 mm (determined from the previous step) was used to simulate the rock mass in the heterogeneous domain of the

RS2 model. Figure 3-15a shows the heterogeneous domain (i.e., VTM) representing the rock mass near the tunnel with a width of 1 m from the excavation boundary.

In the last step of model construction, a rectangular specimen (Figure 3-15b) and a disk-shaped specimen (Figure 3-15c) were carved from the heterogenous domain at the location of the maximum compressive stress to generate the numerical specimens for the simulations of direct tensile, unconfined and confined compression and Brazilian tests.
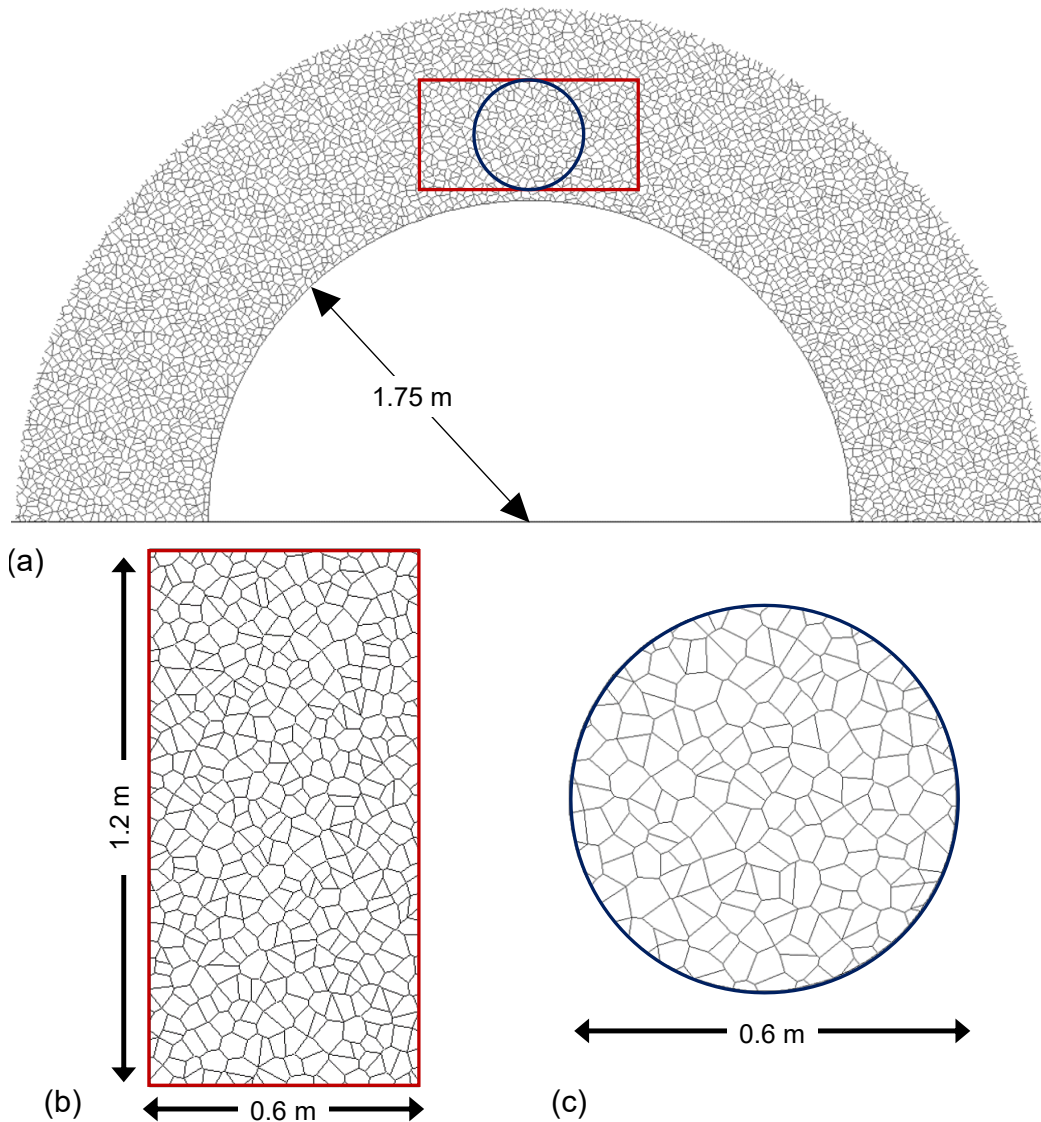
Figure 3-15 a) Voronoi tessellated model used to simulate the rock mass near the test tunnel generated using the joint network option in RS2; b) rectangular-shaped specimen carved from heterogeneous domain near the tunnel for simulating direct tensile and compressive tests; and c) disk-shaped specimen carved from heterogeneous domain near the tunnel for simulating Brazilian test

To consider variability in the simulation results, four additional VTMs with the same width to height ratio were created following the approach described above (Figure 3-16). These specimens were used to determine the minimum, maximum and average strength and deformation modulus for comparison with LdB granite triaxial test results.

#1   #2   #3   #4
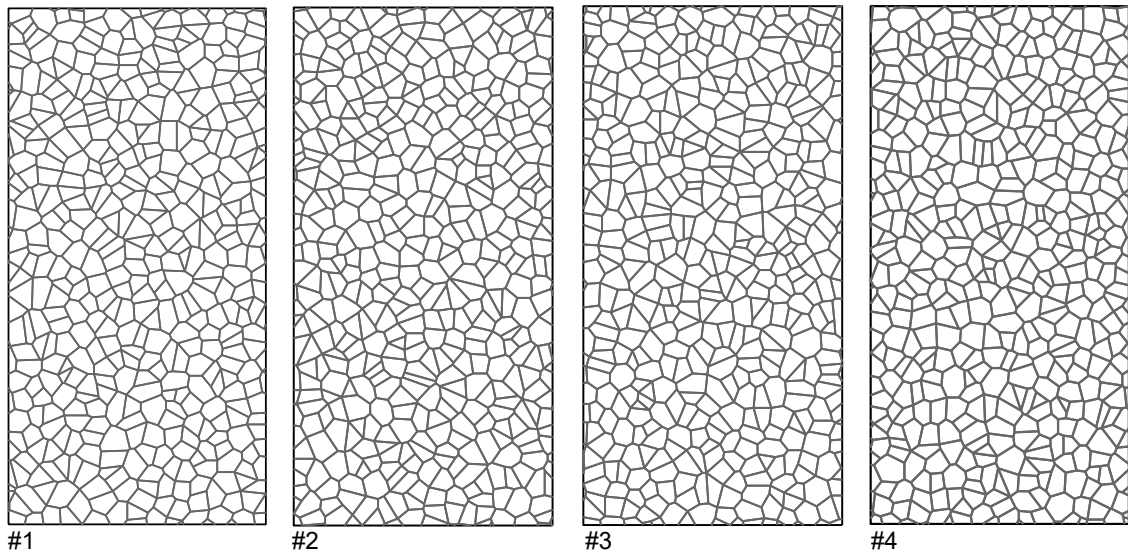
Figure 3-16 Four realizations of rectangular-shaped VTMs carved from the joint network around the model of MBE tunnel

3.4.2 Calibration Procedure

It is essential that a numerical model can replicate the laboratory behavior of rocks as laboratory testing is one of the primary sources of obtaining detailed information regarding the behavior of rocks. Simulating the laboratory behavior of LdB granite by the VTM requires its calibration to the intact strength envelope. Thus, the input parameters for the VTM need to be adjusted in a way that the macro-behavior of the VTM would match that of LdB granite.

As mentioned earlier, the Voronoi joint network divides the numerical specimen into several randomly generated polygonal blocks. Each block is meshed into several elements, and the joint elements represent the block boundaries. The strength properties of the VTM include cohesion (c), friction angle (φ) and tensile strength (σ_t) for blocks (i.e.,

finite elements) and block boundaries (i.e., joint elements). The deformation properties include the Young's modulus (E_b) and Poisson's ratio for blocks, (υ_b), and normal stiffness (k_n) and shear stiffness (k_s) for the block boundaries. Note that the subscripts p, r, b, and bb refer to peak, residual, block and block boundary, respectively. In an RS2-VTM, a total of 16 input parameters (called micro-properties) are required, as listed in Table 3-1.

Table 3-1 Micro-properties of VTM in RS2

	Blocks (i.e., finite elements)	Block Boundaries (i.e., joint elements)
Peak strength	Cohesion, c_{pb} (MPa) Friction angle, ϕ_{pb} (°) Tensile strength, σ_{tpb} (MPa)	Cohesion, c_{pbb} (MPa) Friction angle, ϕ_{pbb} (°) Tensile strength, σ_{tpbb} (MPa)
Residual strength	Cohesion, c_{rb} (MPa) Friction angle, ϕ_{rb} (°) Tensile strength, σ_{trb} (MPa)	Cohesion, c_{rbb} (MPa) Friction angle, ϕ_{rbb} (°) Tensile strength, σ_{trbb} (MPa)
Stiffness	Young's modulus, E_b (GPa) Poisson's ratio, υ_b	Normal stiffness, k_n (MPa/m) Shear stiffness, k_s (MPa/m)

As discussed in Section 3.4, the RS2-GBM with inelastic blocks results in realistic failure mode and post-peak response. Having inelastic blocks and block boundaries means that more input parameters are required for model calibration compared to a model with elastic blocks. This increases the complexity of the calibration process. Li and Bahrani (2021) discussed that the calibration of such models can be simplified by making some assumptions to reduce the computation time. To simplify the calibration procedure, several assumptions were made as described below:

- Both blocks and block boundaries follow the elastic-brittle constitutive behavior.
- The Poisson's ratio of the blocks (υ_b) is obtained from the results of laboratory tests. Therefore, $\upsilon_b = 0.25$.
- The Young's modulus of the blocks (E_b) is equal to the weighted average Young's modulus of the minerals in LdB granite. According to Lan et al. (2010), LdB granite contains 40% K-feldspar, 20% plagioclase, 30% quartz and 10% mafic minerals,

with Young's moduli of 69.8 GPa, 88.1 GPa, 94.5 GPa and 33.8 GPa, respectively. Therefore, E_b = 77 GPa.

- The joint stiffness ratio (k_n/k_s) is 2.5.

- The peak and residual friction angles for blocks and block boundaries (i.e., ϕ_{pb}, ϕ_{pbb}, ϕ_{rb} and ϕ_{rbb}) are considered to be equal to the friction angle of intact LdB granite obtained from triaxial test results (i.e., 57°).

- The peak tensile strength of the block boundaries (σ_{tpbb}) is the same as the average tensile strength of LdB granite obtained from direct tensile tests. Therefore, σ_{tpbb} = 6.9 MPa.

- The residual tensile strengths of blocks (σ_{trb}) and block boundaries (σ_{trbb}) and the residual block cohesion (c_{rbb}) are 0.1 MPa.

The assumptions described above reduced the number of unknowns from 16 to 6, simplifying the calibration process. As a starting point, arbitrary values were chosen for the unknown parameters. All the laboratory tests were simulated, and the macro-properties (i.e., strength and deformation) were compared to those of LdB granite. The initial input micro-properties that were used as a starting point for model calibration are presented in Table 3-2. Note that the peak strengths of both blocks and block boundaries are the same as those of intact rock, which were obtained from the equivalent Mohr-Coulomb strength envelope (c = 30 MPa and ϕ = 57°) for a maximum confining pressure of 25 MPa (see Figure 3-4). The rest of the input parameters follow the assumptions described above.

The initial values given in Table 3-2 significantly underestimated the VTM peak strength when compared to the peak strength of intact LdB granite obtained from laboratory tests, as demonstrated in Figure 3-17. The emergent tensile strength of the VTM is 4.7 MPa, which is lower than that of intact LdB granite (6.9 MPa).

Table 3-2 Initial input micro-properties of VTM

		Micro-properties	Values
Block	Peak strength	Peak cohesion (MPa)	30*
		Peak friction angle (°)	57*
		Peak tensile strength (MPa)	6.9*
	Residual strength	Residual cohesion (MPa)	30**
		Residual friction angle (°)	57**
		Residual tensile strength (MPa)	0.1**
	Deformation properties	Young's modulus (GPa)	77**
		Poisson's ratio	0.25*
Block boundary	Peak strength	Peak cohesion (MPa)	30*
		Peak friction angle (°)	57*
		Peak tensile strength (MPa)	6.9*
	Residual strength	Residual cohesion (MPa)	0.1**
		Residual friction angle (°)	57**
		Residual tensile strength (MPa)	0.1**
	Deformation properties	Normal stiffness (MPa/m)	10×10^6
		Shear stiffness (MPa/m)	4×10^6

* Intact rock properties obtained from laboratory tests (Martin 1993; 1997)
** Assumption (see Section 3.4.2)
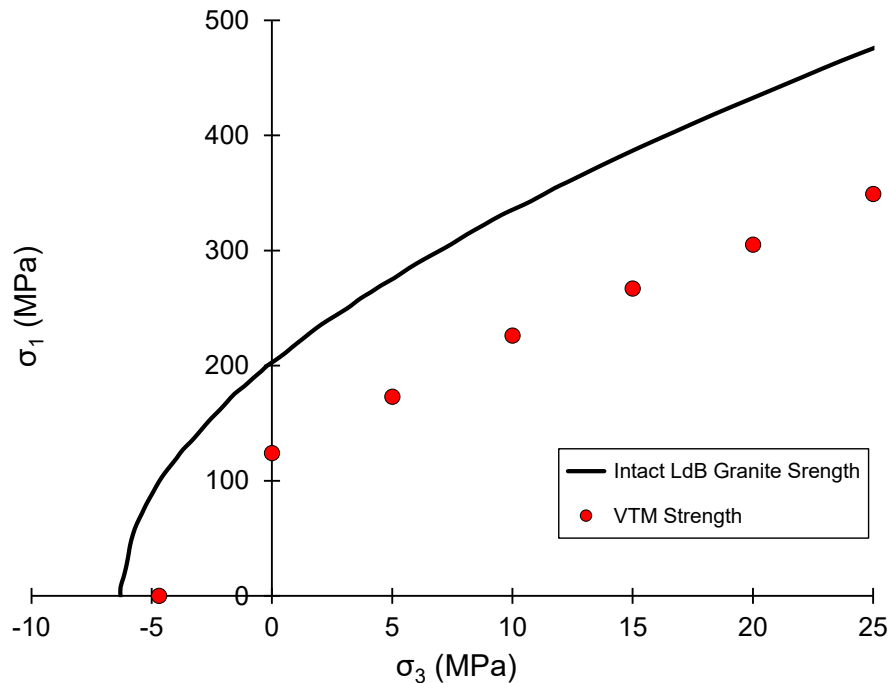
Figure 3-17 Emergent peak strengths for VTM with initial values given in Table 3-2, compared to the strength envelope of intact LdB granite obtained from laboratory tests

It is concluded that in order to match the VTM strength to the strength envelope of intact LdB granite, the micro-properties of the VTM should be adjusted through a systematic calibration process. The flowchart in Figure 3-18 illustrates the steps that were taken to calibrate the VTM to the laboratory properties of intact LdB granite. The model calibration started by simulating the BTS and DTS tests, which required adjusting the σ_{tpb} value. Once the VTM was calibrated to the tensile strength of LdB granite (6.9 MPa), the UCS test was simulated. At this stage, the joint stiffness values (k_n and k_s) were adjusted until the Young's modulus of LdB granite (65 GPa) was matched, and the c_{pb} and c_{pbb} values were adjusted until the UCS of intact rock (213 MPa) was matched. In the final stage of model calibration, the confined compressive strength of LdB granite was matched by adjusting the c_{rb} value. At this stage, all the tensile and compressive tests simulations were repeated, and when a match with the laboratory strength and deformation properties of intact LdB granite was not achieved, model calibration was repeated from the first step. The details of this calibration process and the results of laboratory test simulations using the VTM are presented in the following section.
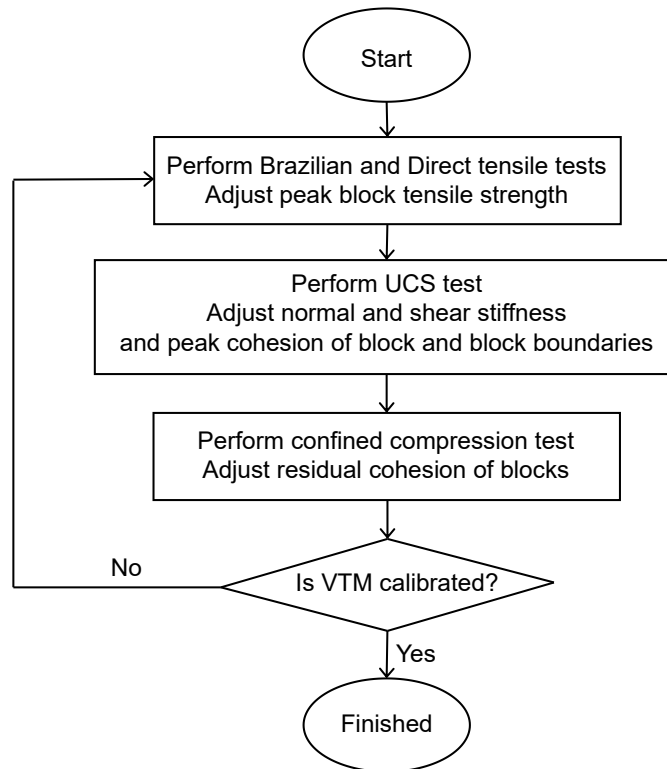
Figure 3-18 Flowchart showing the procedure for calibrating the RS2-VTM to laboratory properties of intact LdB granite

3.4.3 Simulation of Laboratory Tests Using VTM

3.4.3.1 Brazilian Tensile Strength (BTS) Test

The Brazilian tensile test was simulated by loading the disk-shaped VTM by applying a constant displacement to the top boundary of the model, as shown in Figure 3-8c with a rate of 0.1 mm per stage. As the maximum tensile stress in the Brazilian disk occurs at its centre, the average of node stresses (σ_3) within a 40 mm × 40 mm window at the center of the VTM was used to monitor the tensile stresses. The VTM was calibrated to the tensile strength of LdB granite (i.e., 6.9 MPa) by adjusting the σ_{tpb} value, which resulted in a damage initiation of about 80% of the peak stress.

Figure 3-19a and b show the stress-strain curve from the BTS test simulation and the failure mode at three stress levels corresponding to 80% of the peak, the peak stress, and the first stage in the post-peak region, where a sudden stress drop occurred. Matching the peak strength and pre-peak damage initiation in the calibration cycle led to a σ_{tpb} value of 11 MPa. As shown in Figure 3-19b, the onset of block boundary yielding occurs before the peak at about 80% of the peak stress. This is followed by the initiation of finite element (block) yielding near the peak stress and its rapid propagation in the post-peak region. The macro-response of the VTM agrees with that of standard laboratory BTS tests. Analysis of the stress-strain curve and simulated progressive damage in Figure 3-19a and b suggests that: 1) block boundary yielding is an indication of damage, as it does not cause a sudden stress drop; 2) block yielding and its rapid propagation is an indication of failure, as it significantly redistributes the stresses; 3) the blocks are yielded only in tension; thus, the failure mechanism captured by the VTM is purely in tension. This is consistent with the observed failure mode of BTS tests in the laboratory.
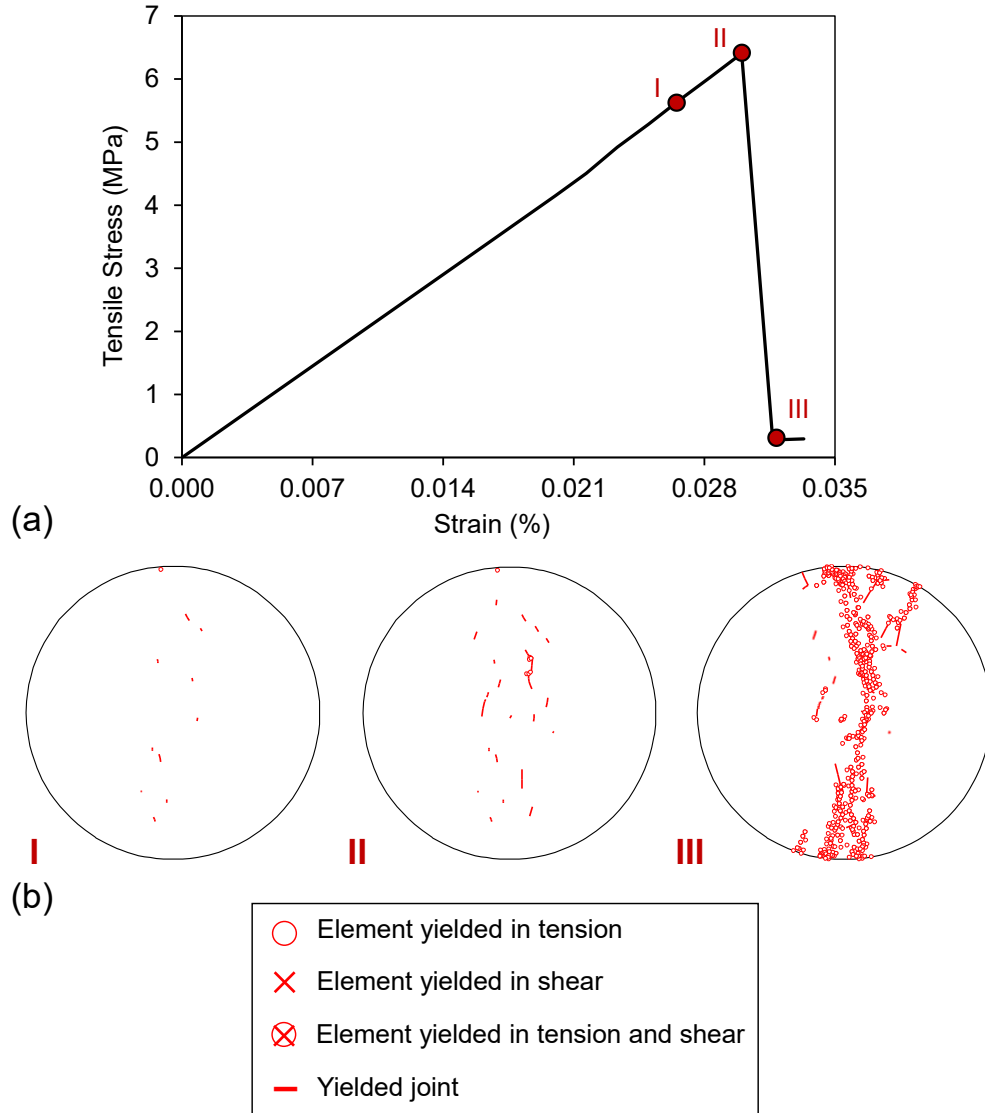
Figure 3-19 a) Stress-strain curve of simulated BTS test using VTM in RS2; and b) failure modes at three loading stages: damage initiation (I), peak stress (II), and post-peak (III)

3.4.3.2 Direct Tensile Strength (DTS) Test

Typically, the BTS of intact rock is higher than its DTS. Laboratory tests on LdB granite resulted in an average DTS and BTS of 6.9 MPa and 8.8 MPa, respectively (Martin, 1994; and Qi et al., 2019). However, it was found that the tensile strengths obtained from the simulations of DTS and BTS tests using RS2-VTM are equal. This could be due to the stress calculation method in the Brazilian test simulation. In this test, the BTS was calculated from the average stresses at the centre of the disk and not from the reaction forces at the

top boundary of the model. This suggests that the method of stress calculation in the Brazilian test simulation needs further investigation.

The boundary conditions used to simulate the DTS test are shown in Figure 3-8b. The DTS test was simulated by applying a displacement boundary with a constant rate of 0.025- mm per stage to the top boundary of the VTM in the vertical direction. The tensile stress was calculated by averaging all the node stresses (σ_3) within the specimen at every stage. The stress-strain curve and failure mode at three stress levels corresponding to the damage initiation, the peak stress and the first stage in the post-peak region, where a sudden stress drop occurred, are shown in Figure 3-20a and b, respectively.

Figure 3-20b shows that block boundary yielding purely in tension, representing damage, initiates at about 85% of the peak stress (stage I). The number of yielded block boundaries slightly increases until the peak stress (stage II). This is followed by a sudden increase in the number of yielded blocks and block boundaries, generating failure planes perpendicular to the loading direction (stage III). This sudden yielding causes a significant stress drop in the post-peak region. The macroscopic failure mode of the DTS test captured by the VTM is consistent with the failure mode observed in laboratory tests.
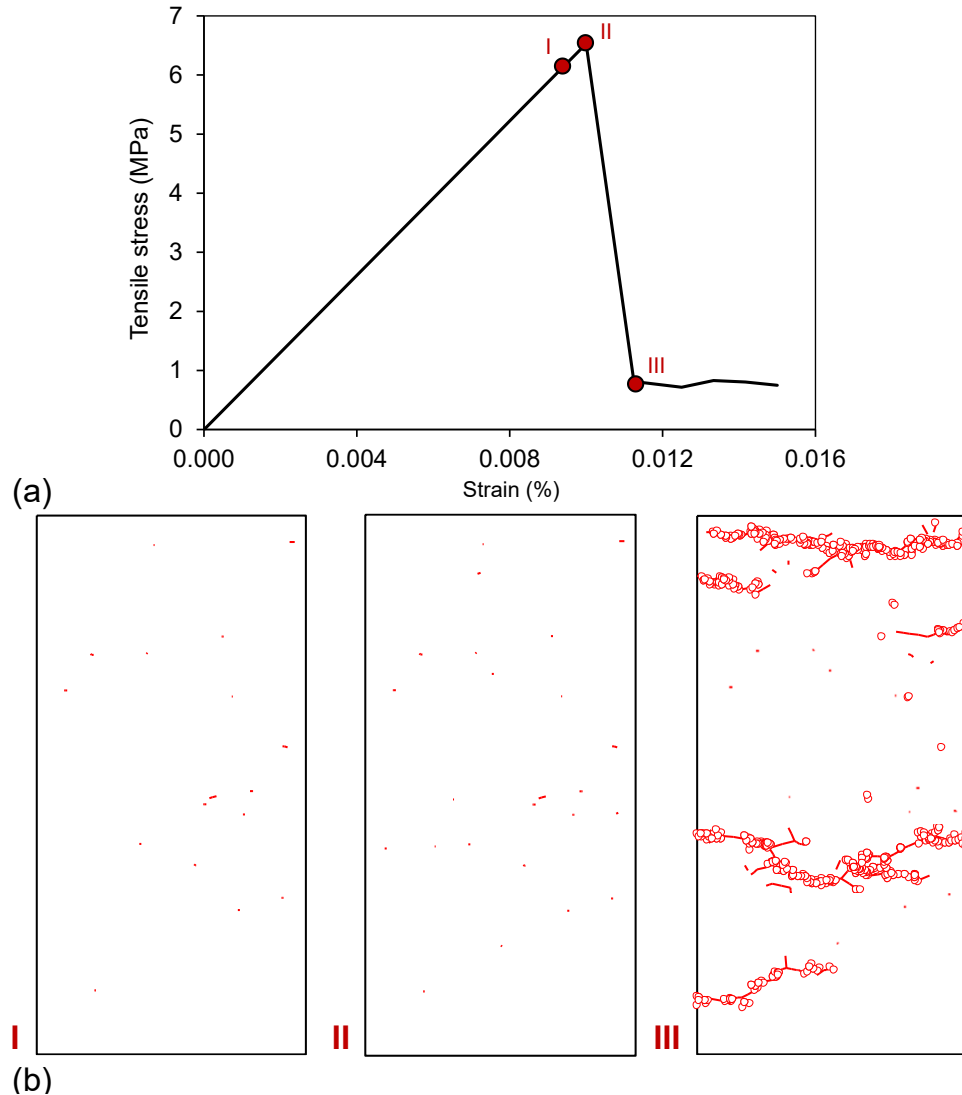
Figure 3-20 a) Stress-strain curve of simulated DTS test using VTM in RS2; and b) failure modes at three loading stages: damage initiation (I), peak stress (II) and failure in the post-peak region (III)

3.4.3.3 Uniaxial Compressive Strength (UCS) Test

It is known that the failure mode of low porosity crystalline rocks under an unconfined condition is axial splitting. As discussed earlier, the geometrical heterogeneity in the VTM makes it possible to capture localized tensile stresses within the specimen even under an overall compressive stress field. Other than the macroscopic failure mode, it is desirable to capture the following during compressive loading: 1) crack initiation (σ_{ci}); 2) crack damage (σ_d); and 3) sudden stress-drop in the post-peak region.

The UCS test was simulated by applying a displacement boundary with a constant rate of 0.2 mm per stage to the top boundary of the VTM, as shown in Figure 3-8a. Similar to the DTS test, the lower boundary was fixed in the horizontal direction, except for the midpoint, which was fixed in both horizontal and vertical directions.

The Young's modulus of the VTM was calculated from the slope of the axial stress versus axial strain curve. Matching the Young's modulus of the VTM to that of LdB granite (i.e., 65 GPa) required adjusting the block boundary k_n and k_s values, as the deformation modulus of the blocks was assumed to be 77 GPa, equal to the weighted average of the deformation moduli of the mineral grains. During the calibration process, the target strength was set to the average UCS of intact LdB granite obtained from laboratory tests (i.e., 213 MPa). c_{pb} was found to be the main factor controlling the UCS of the VTM among the six unknown input parameters, while c_{pbb} was found to control block boundary yielding in the pre-peak loading stages.

Figure 3-21b and c show that the VTM realistically simulates the failure mode of LdB granite in a UCS test. The sub-vertical block boundary yielding (Figure 3-21b) initiates at about 30% of the peak stress (stage I). The density of yielded block boundaries increases as the axial stress increases (stages II and III). Block tensile yielding initiates at about 70% (stage II in Figure 3-21c) and propagates at about 90% (stage III) of the peak stress. A sudden drop in the axial stress coincides with instantaneous yielding of several blocks (finite elements) in the first loading stage following the peak stress (stage IV in Figure 3-21c). The pattern of yielded finite elements at stage IV (all in tension) resembles axial splitting observed in laboratory tests.
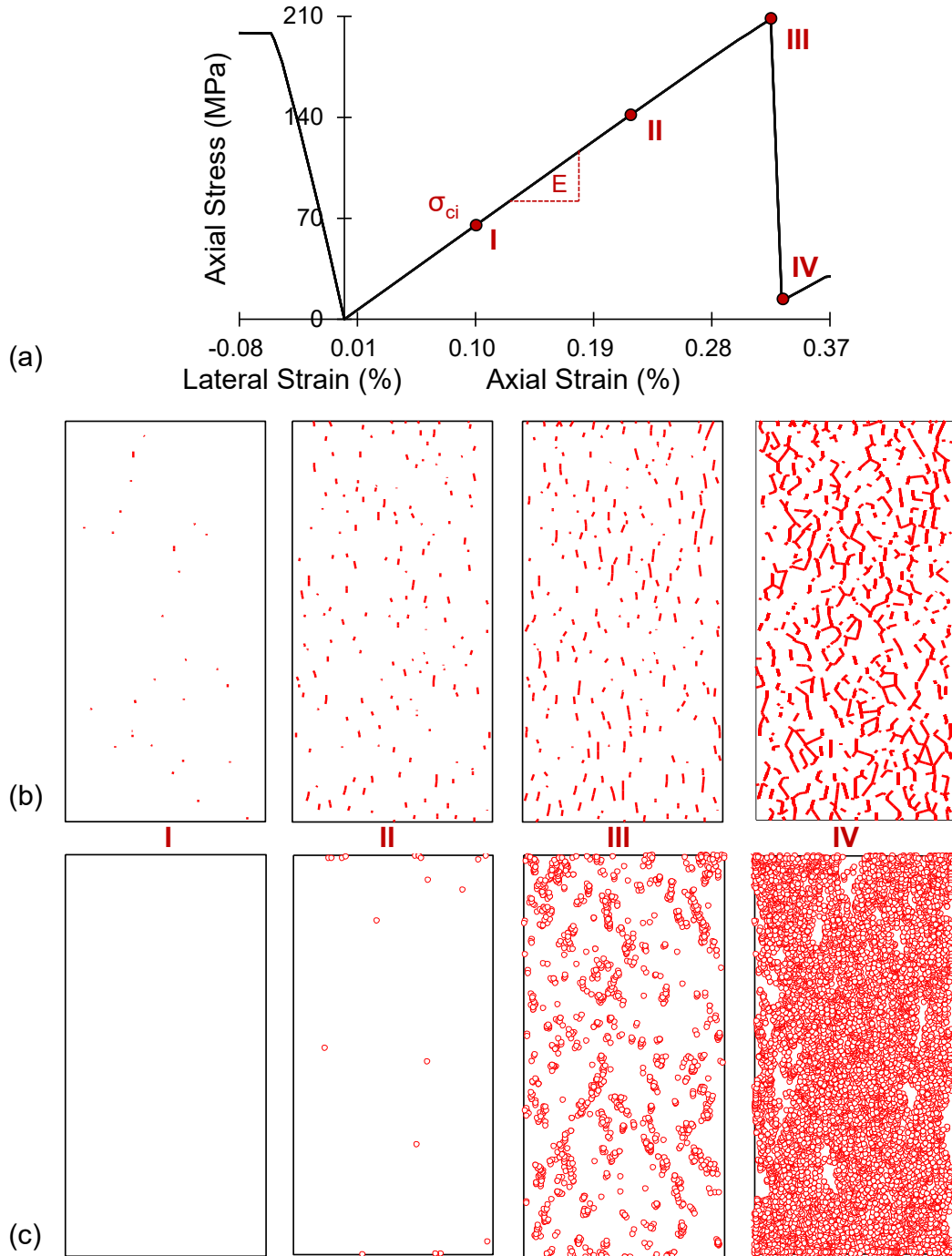
Figure 3-21 a) Axial stress versus axial and lateral strains; b) block boundary yielding; and c) block yielding at four loading stages

Martin (1990) and Eberhardt et al. (1998) defined the crack initiation threshold as the stress level at which the lateral and volumetric strain curves depart from linearity. However, the VTM does not capture the initial crack closure nor the deviation from linearity in the axial stress versus lateral strain curve (Figure 3-21a). The crack initiation

threshold of LdB granite is approximately 71 MPa (Martin and Chandler, 1994; Martin, 1997; Read et al., 1998), which is close to the stress level at which acoustic emissions were detected in the field (i.e., in situ damage initiation). The first signs of damage in the VTM (i.e., block boundary yielding) occurs at about 30% of the peak stress (σ_{ci} = 65 MPa), as illustrated in Figure 3-21b. According to Cai et al. (2004), the crack initiation threshold of intact rock ranges between 30% and 50% of the peak stress. Thus, it is concluded that the continuum-based VTM is capable of capturing the crack initiation threshold of intact LdB granite.

3.4.3.4   Confined Compression Strength Tests

The confined compression tests were simulated for confining pressures of 5, 10, 15, 20 and 25 MPa. To simulate the confined compression test, a constant stress boundary was first applied to the model boundaries (except for the bottom boundary) to mimic the hydrostatic confining pressure, as shown in Figure 3-8d. At later stages, a displacement boundary was applied to the top boundary of the model to simulate axial loading. Throughout the simulations, the c_{rb} value was adjusted to match the confined strength of LdB granite obtained from laboratory tests. It was found that this parameter has the largest influence on the confined peak strength of the VTM among the six unknown input parameters.

The stress-strain curves with the corresponding failure modes of the simulated confined tests (i.e., post-peak macro-behavior) are presented in Figure 3-22a and b, respectively. According to Martin and Chandler (1994), the post-peak response of intact LdB granite exhibited a stress drop even at high confinements (e.g., 60 MPa). It should be noted that LdB granite post-peak response was not considered in the calibration process. However, the emergent post-peak behavior of the calibrated VTM is consistent with the laboratory tests.
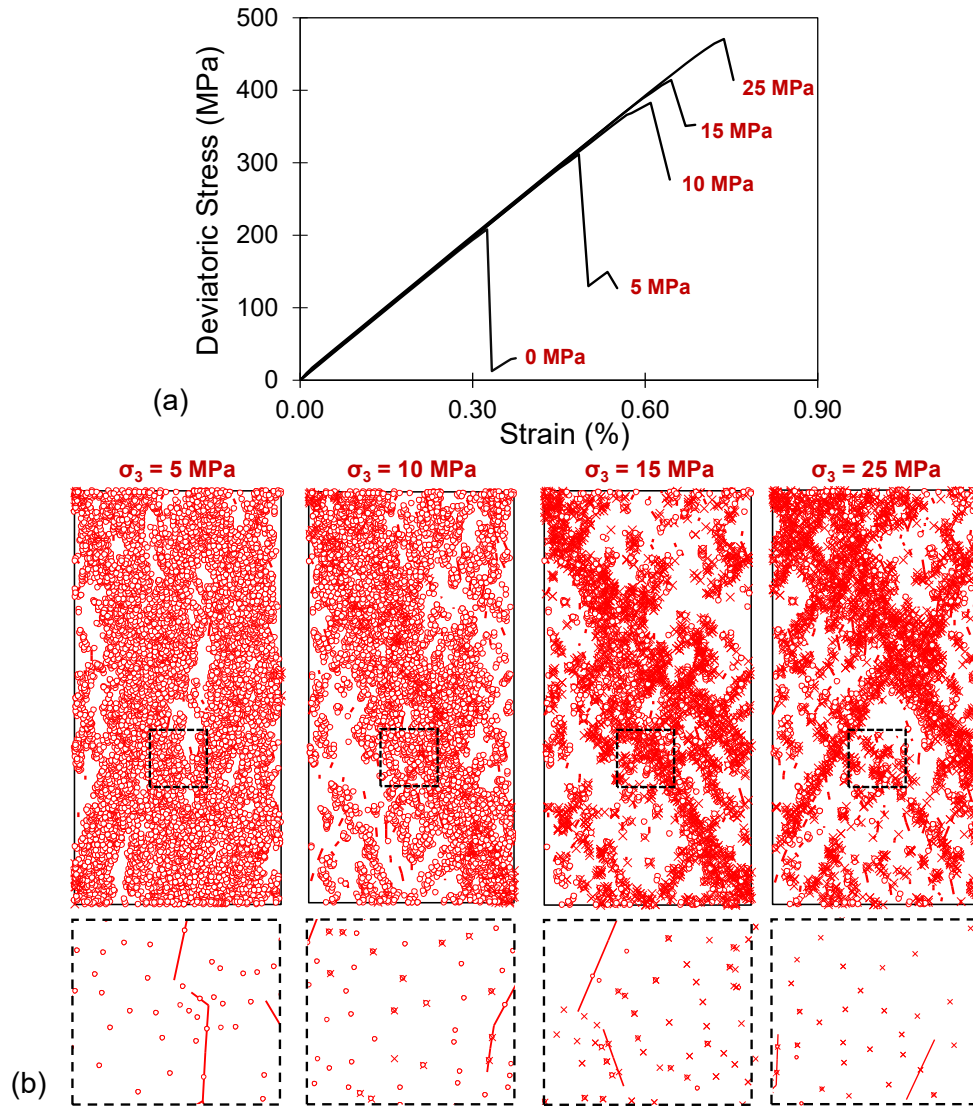
Figure 3-22 a) Stress-strain curves of simulated confined compression tests using VTM; and b) corresponding failure modes of four confined compression tests

In Figure 3-22b, a transition from tensile to shear failure can be observed in the calibrated VTM as the confinement increases. At low confining pressures (i.e., 0 and 5 MPa), most of the elements are yielded in tension, but the macroscopic yielded pattern suggests a combined axial splitting and shear failure. At higher confinements (e.g., 25 MPa), most of the elements are yielded in shear generating conjugate shear bands, consistent with observed failure mode in laboratory tests. Therefore, it is concluded from the simulation results that the continuum-based VTM can realistically capture the stress-strain behavior and the failure mechanism of brittle rocks for a wide range of confinement.

3.4.4   VTM Calibration Results

The micro-properties of the calibrated VTM are presented in Table 3-3. As discussed by Bahrani et al. (2014) and Sinha and Walton (2020), in such models, multiple combinations of input parameters could lead to similar calibration results (i.e., macro-properties and macro-behavior). Therefore, the presented combination of micro-properties is one of the many possible solutions for the continuum-based VTM of LdB granite.

Table 3-3 Micro-properties of VTM calibrated to laboratory properties of LdB granite

		Micro-properties	Value
Block	Peak strength	Peak cohesion (MPa)	80
		Peak friction angle (°)	57*
		Peak tensile strength (MPa)	11
	Residual strength	Residual cohesion (MPa)	50
		Residual friction angle (°)	57*
		Residual tensile strength (MPa)	0.1**
	Deformation properties	Young's modulus (GPa)	77**
		Poisson's ratio	0.25*
Block boundary	Peak strength	Peak cohesion (MPa)	60
		Peak friction angle (°)	57*
		Peak tensile strength (MPa)	6.9*
	Residual strength	Residual cohesion (MPa)	0.1**
		Residual friction angle (°)	57*
		Residual tensile strength (MPa)	0.1**
	Deformation properties	Normal stiffness (MPa/m)	10.5×10^6
		Shear stiffness (MPa/m)	4.1×10^6

* Intact rock properties obtained from laboratory tests (Martin 1993; 1997)
** Assumption (see Section 3.4.2)

As shown in Figure 3-23a, the peak strength of the VTM is a result of four input strength envelopes: 1) peak block strength; 2) residual block strength; 3) peak block boundary strength; and 4) residual block boundary strength. Figure 3-23b shows the peak strengths of four VTMs with different joint network realizations. This figure also shows the HB strength envelope fitted to the results of laboratory tests on intact LdB granite for comparison purposes. It was found that the m-value and UCS for the calibrated VTM (i.e.,

28.17 and 208.27 MPa, respectively) are comparable to those of intact LdB granite obtained from laboratory triaxial tests (i.e., 34.79 and 203 MPa), confirming that the VTM is well calibrated. Figure 3-23b shows that the non-linearity in the emergent strength envelope of the VTM obtained from different realizations is consistent with the Hoek-Brown strength envelope fitted to the results of laboratory triaxial tests.
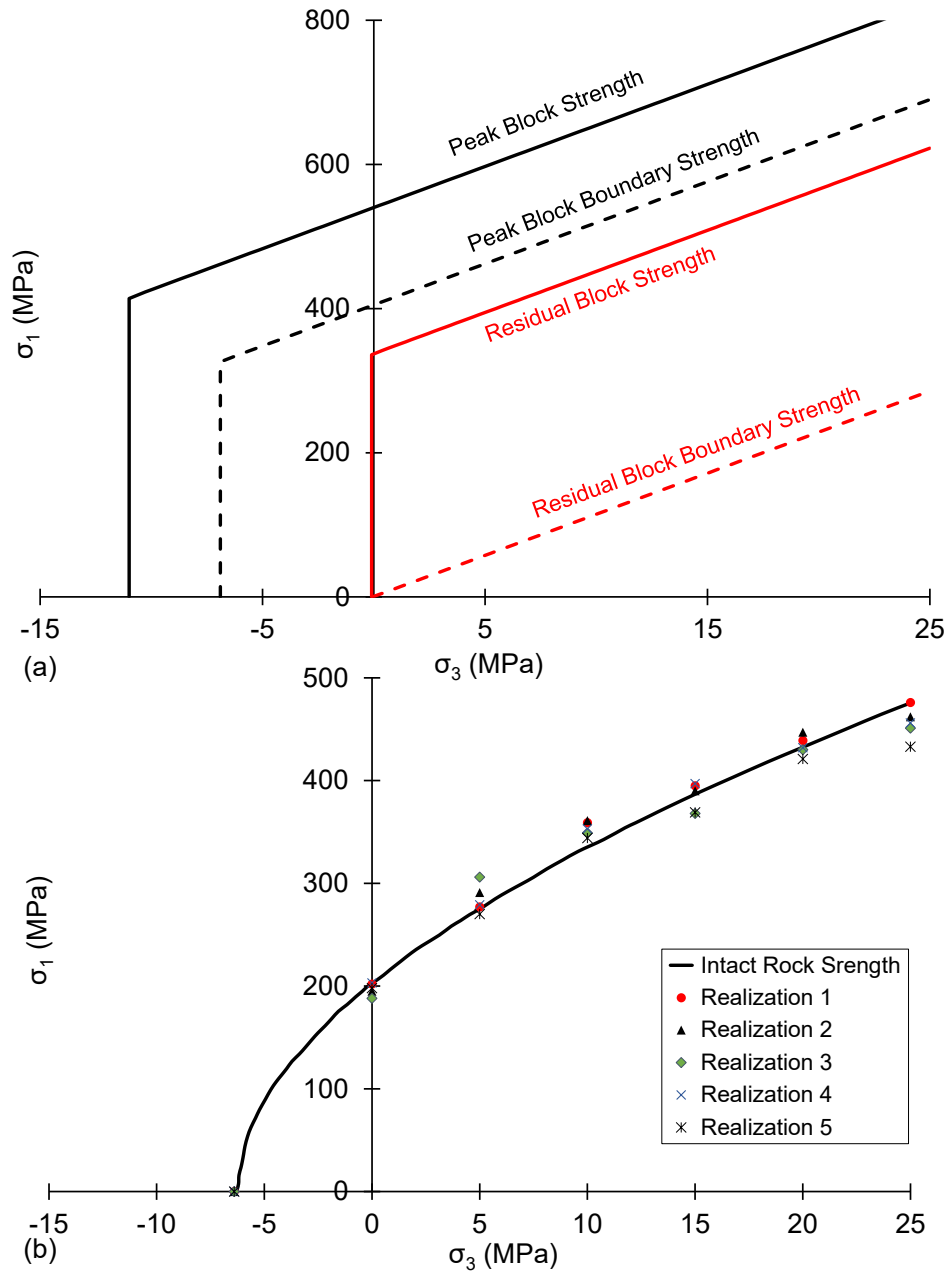
Figure 3-23 a) Peak and residual strength envelopes of VTM calibrated to laboratory properties of intact LdB granite; and b) strength envelope of intact LdB granite obtained from laboratory tests compared to peak strengths of five VTMs with different joint network realizations

The following figure shows the failure modes of the simulated laboratory tests using three realizations of the VTM with the micro-properties given in Table 3-3. This figure indicates that although the VTM with different realizations were assigned the same micro-properties, their failure patterns are not the same. This is due to different block arrangements stochastically generated using the built-in joint network option in RS2.
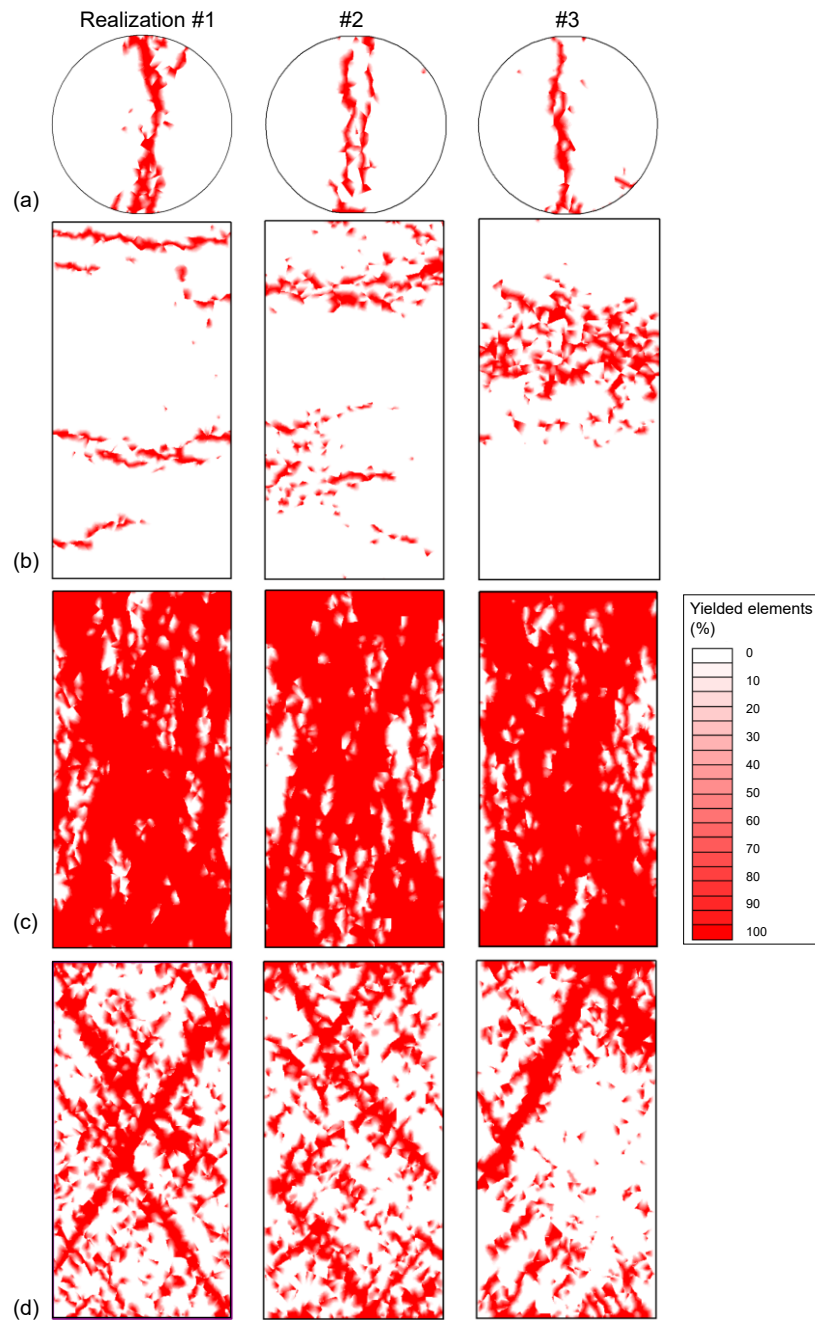
Figure 3-24 Failure modes of laboratory tests simulated using three realizations of RS2-VTM calibrated to intact rock properties: a) BTS test; b) DTS test; c) UCS test; and d) confined compression test at a confining pressure of 25 MPa

3.4.5 Simulation of MBE Tunnel Using VTM Calibrated to Laboratory Properties of Intact Rock

Previous numerical investigations indicate that a 2D model calibrated to the laboratory peak strength of intact LdB granite (i.e., UCS = 213 MPa) cannot capture the shape and depth of failure around the MBE tunnel, even when heterogeneities are considered (Shin, 2010; Azocar, 2016; Bahrani et al., 2019; and Vazaios et al., 2019). Bahrani et al. (2019) discussed that this could be due to the 3D stress path and stress rotation causing strength degradation ahead of an advancing tunnel, which is not captured in a 2D model.

The simulation of laboratory tests showed that block boundary and block yielding initiate at about 30% and 70% of the peak stress, respectively. The maximum tangential stress at the MBE tunnel boundary based on plane strain elastic analysis (e.g., Kirsch equations) is 169 MPa, which is about 20% lower than the UCS of the calibrated VTM. Therefore, it was expected that the induced localized tensile stresses around the tunnel would lead to only sparse yielding near the notch area, but not a complete failure.

Nevertheless, to further investigate the DoF, SoF and EDZ, the MBE tunnel was simulated using the calibrated VTM. Figure 3-25 shows the RS2 model of the MBE tunnel, which consists of homogenous and heterogeneous (i.e., VTM) domains. In this model, the heterogeneous domain consisting of Voronoi blocks has the same block size and mesh geometry as those used to simulate laboratory tests. The results of sensitivity analyses indicated that the coarser mesh elements in the homogenous domain around the VTM have a negligible impact on the stress redistribution in the VTM zone. This was further investigated by comparing the elastic stresses in the VTM consisting of elastic blocks and block boundaries (shown in Figure 3-25) with those of a homogeneous elastic model, which is described in the following section.

The in situ stress magnitudes used in this model were σ_1 = 60 MPa, σ_2 = 45 MPa, and σ_3 = 11 MPa, where σ_1 and σ_3 were assumed to be horizontal and vertical, respectively. The core softening approach (Vlachopoulos and Diederichs, 2014) was used to replicate the 3D tunnel advance in the 2D model.
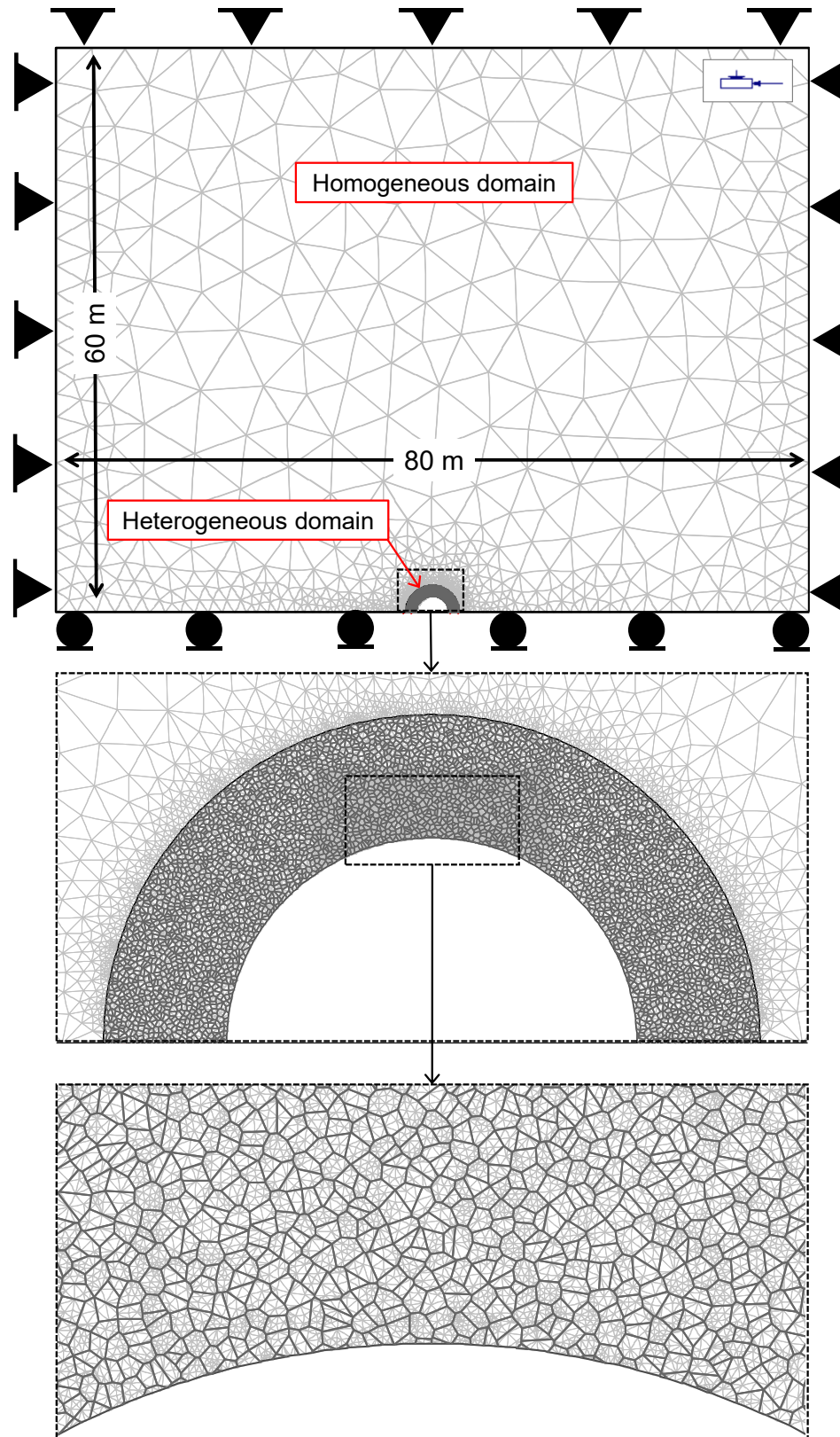
Figure 3-25 Geometry of the RS2 model of MBE tunnel. Note: Tunnel radius is 1.75 m.

3.4.5.1 Elastic VTM

Prior to using the model of the MBE tunnel with inelastic VTM properties, it is paramount to verify that the redistributed elastic stresses are comparable to those of the homogeneous model shown in Figure 3-2. For this purpose, both the blocks and block boundaries in the heterogeneous domain (i.e., VTM) of the modeled tunnel were assumed to be elastic. Figure 3-26 shows the contours of major and minor principal stresses around the tunnel.
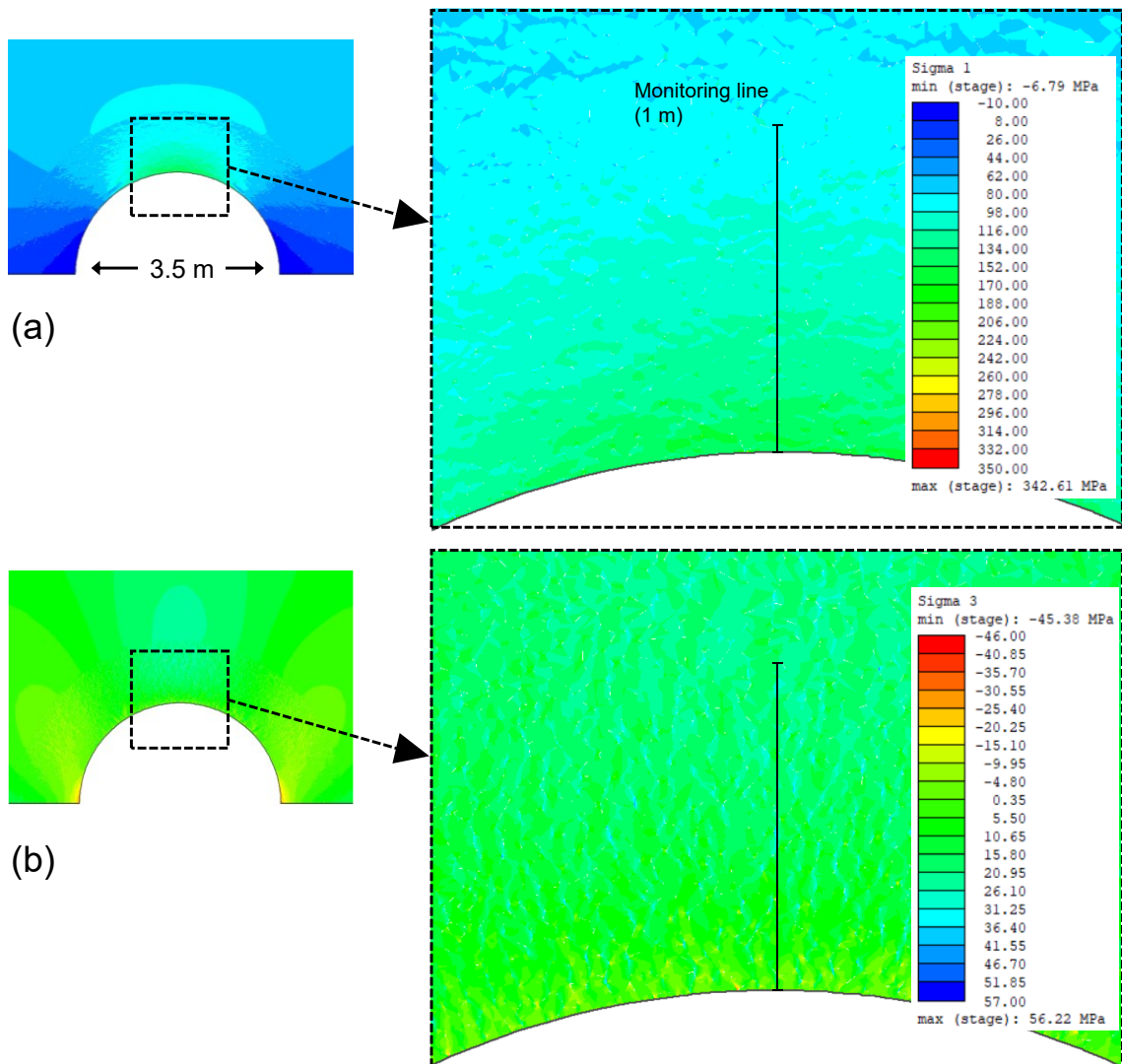
Figure 3-26 Elastic stresses around MBE tunnel following the excavation of the tunnel: a) major principal stresses; and b) minor principal stresses

In order to determine whether the stress distribution around the tunnel is similar to that of the homogeneous model, the major and minor principal stresses along the monitoring

line shown in Figure 3-26, were plotted in Figure 3-27. Note that the variation of stresses along the monitoring line (i.e., around the tunnel) shown in Figure 3-27 is caused by geometrical heterogeneities in the VTM. It is concluded that the distributions of the stresses are consistent with those obtained from the homogeneous model (see Figure 3-2), and therefore, an inelastic VTM can be used to simulate the MBE tunnel and its failure.
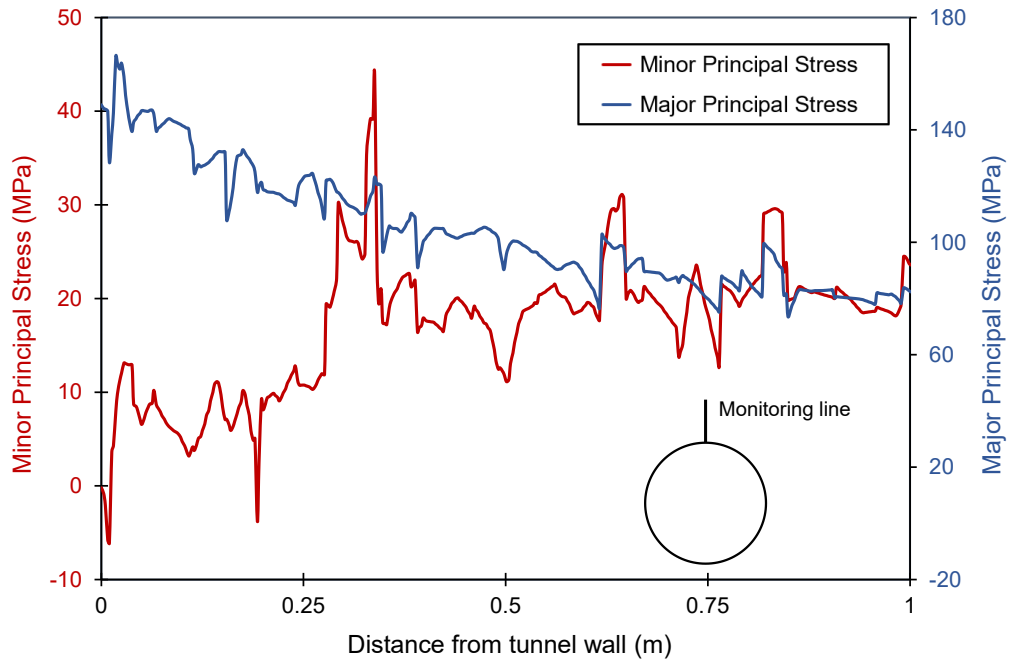
Figure 3-27 Major and minor principal stresses along the monitoring line obtained from heterogeneous elastic model of MBE tunnel

3.4.5.2   Inelastic VTM

As mentioned earlier, the Core Softening (CS) approach was used in this study to replicate the 3D advance of the MBE tunnel. In this method, the Young's modulus of the tunnel core is gradually reduced from its initial value in different stages. In the last stage, the core is fully excavated. Using the CS approach, the progressive deformation of the excavation boundary due to the tunnel advance can be approximated (Vlachopoulos and Diederichs, 2014). Table 3-4 shows the stages and corresponding Young's moduli of the core used to simulate the 3D advance of the MBE tunnel.

Table 3-4 RS2 stages and corresponding tunnel core Young's moduli used in the simulation of 3D tunnel advance using core softening approach

Stage #	Young's modulus (GPa)	Comment
1	65	Initial stiffness assigned
2	40	
3	30	
4	20	
5	10	
6	5	
7	2	
8	0.5	
9	0.02	
10	0	Core excavated

Figure 3-28 shows the failed (v-shaped notch) and damaged (micro-seismic events) zones near the MBE tunnel. As expected and shown in Figure 3-28, failure does not occur near the tunnel simulated using the calibrated VTM. Only sparse random block and block boundary yielding occurred around the tunnel boundary near the failed zone. The simulation result is consistent with those of previous research (e.g., Shin, 2010; Potyondy and Cundall, 2004; Azocar, 2016; Bahrani et al., 2019; and Vazaios et al., 2019), confirming that 2D models (homogeneous or heterogeneous) calibrated to the laboratory properties of intact rock with a UCS of 213 MPa cannot adequately capture the DoF and EDZ around the MBE tunnel.
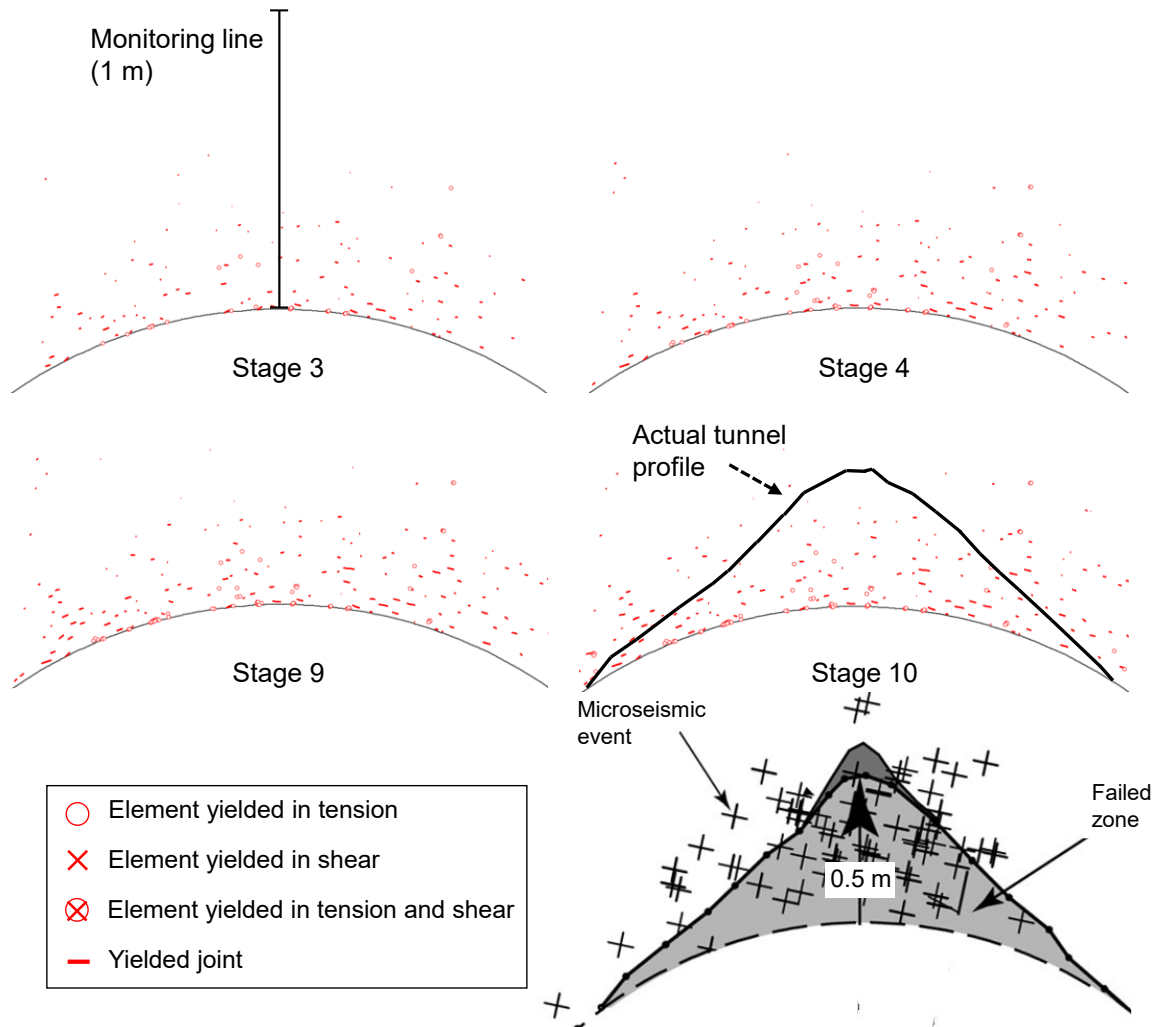
Figure 3-28 MBE tunnel simulated using VTM calibrated to laboratory properties of intact rock in RS2. Shape and extent of failure and micro-seismic events around MBE tunnel (after Hajiabdolmajid et al., 2002) is presented for comparison purposes.

To further investigate whether the block boundary yielding is an indication of damage and not failure, the minor principal stress was plotted along the monitoring line shown in Figure 3-28, and compared with that from the elastic homogenous model (Figure 3-2). This comparison suggests that the stress redistributions in the two models are essentially the same. As mentioned earlier, the stress variation in the heterogeneous model is due to geometric heterogeneity. The slight difference between the results of the two models can be attributed to the random block and block boundary yielding in the heterogeneous model, although they do not result in significant stress changes near the excavation boundary. Therefore, it is concluded that the block boundary yielding around the tunnel represents pre-peak damage rather than failure.
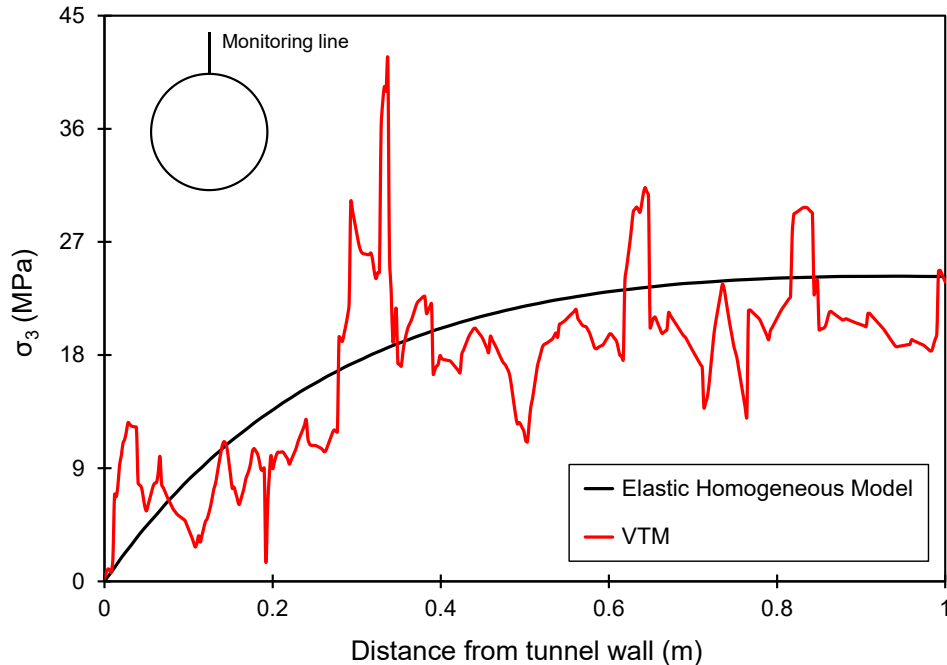
Figure 3-29 σ_3 distribution along the monitoring line following tunnel core excavation obtained from elastic homogeneous and inelastic heterogeneous models

It is concluded that in order to realistically simulate the v-shaped notch failure around the MBE tunnel, the VTM should be calibrated to the rock mass strength rather than the laboratory peak strength. For this purpose, the rock mass strength is estimated in the following chapter and the VTM is calibrated accordingly to simulate the DoF, SoF and EDZ around the MBE tunnel.

3.5   Summary

In this chapter, two-dimensional continuum models were used to simulate the progressive failure of LdB granite under laboratory and field loading conditions. First, elastic stress analyses were conducted to better understand the stress distribution during progressive spalling and slabbing, leading to the v-shaped notch failure near the MBE tunnel. The simulation of the v-shaped notch failure involved several stages of manual slab removal in the homogeneous elastic model. It was found that the magnitudes of the major and minor principal stresses increase near the excavation boundary as the slabs were progressively removed. Once the final geometry of the notch was reached, an increase in localized values of the major principal stress under high confinement was

observed at the notch tip. The results of elastic stress analyses suggest that the final notch geometry provided sufficient confinement above the notch tip that inhibited the propagation of the cracks into the rock mass.

Next, the application of the DISL model (originally developed to capture the DoF and SoF around the MBE tunnel) for simulating brittle rock failure under laboratory loading conditions was investigated. For this purpose, standard rock mechanics laboratory tests such as the BTS, DTS, UCS and confined compression tests were simulated. It was found that all the elements yield simultaneously and immediately in shear once the peak stress is exceeded. This is because the homogeneous model consists of finite elements with the same properties; thus, localized tensile stresses and pre-peak yielding leading to axial splitting in the UCS test and shear band formation in the confined compression tests cannot be captured. It was concluded that for realistically simulating the failure mechanism of brittle rocks, geometric heterogeneities need to be implemented in the numerical model. This would allow the generation of localized tensile stresses and tensile damage prior to the peak stress under different loading conditions.

A 2D continuum-based VTM for LdB granite was developed to consider the heterogeneous nature of the rock. A procedure was proposed to calibrate the model to the laboratory properties of intact rock. To this end, laboratory tests were simulated, and the micro-properties required for the VTM were systematically adjusted. The calibrated VTM was then used to investigate the failure around the MBE tunnel. It was found that the VTM calibrated to the laboratory properties of intact LdB granite does not adequately capture the DoF and EDZ, which is consistent with the results of previous numerical investigations.

Note that using the peak strength of intact rock obtained from laboratory tests is generally the first step when simulating a field-scale excavation in a massive rock mass. In order to realistically simulate the v-shaped notch failure around the MBE tunnel using the VTM, the in situ rock mass strength needs to be first estimated and then used as the target for model calibration. As suggested by other researchers (e.g., Diederichs, 2007), the s-shaped failure envelope with a reduced rock strength would allow the yielding to

initiate around the tunnel boundary and propagate until the observed v-shaped notch failure is captured. The simulation of the v-shaped notch failure around the MBE tunnel using the VTM calibrated to the rock mass strength estimated based on the s-shaped failure criterion will be the focus of the next chapter.

Chapter 4 Simulation of Mine-by Experiment (MBE) Tunnel Using VTM Calibrated to Rock Mass Strength

4.1 Introduction

As reviewed in Chapter 2, various numerical approaches have been developed to investigate the progressive brittle failure around the MBE tunnel (e.g., Hajiabdolmajid et al., 2002; Potyondy & Cundall, 2004; Hazzard & Young, 2004; Diederichs, 2007; Cai & Kaiser, 2014; Vazaios et al., 2019). It was concluded in Chapter 3 that the numerical models need to be calibrated to the strength of the rock mass in order to capture the DoF and SoF around the MBE tunnel. In addition to the DoF and SoF, capturing realistic failure modes and the extent of the EDZ are desirable. Diederichs (1999) and Kaiser et al. (2000) have suggested that an s-shaped failure envelope would allow the yielding to initiate at a lower compressive stress around the tunnel boundary and propagate until the observed v-shaped notch failure is captured.

In this chapter, the RS2-VTM developed in Chapter 3 is first calibrated against the tri-linear strength envelope, which is based on the s-shaped failure criterion proposed by Diederichs (1999; 2003) and Kaiser et al. (2000). This includes simulating the standard rock mechanics laboratory tests, such as the BTS, DTS, unconfined and confined compression tests, and adjusting the micro-properties of the VTM until the model is calibrated. The calibrated VTM is then used to simulate the DoF, EDZ and SoF around the test tunnel.

4.2 Strength of Massive to Moderately Jointed Rock Masses

4.2.1 Hoek-Brown (HB) Failure Criterion

The HB failure criterion is an empirical method proposed by Hoek and Brown (1980) to provide input parameters for the design of underground excavations in jointed rock masses. The generalized HB failure criterion is defined by the following equation:

$$\sigma_1' = \sigma_3' + \sigma_{ci} \left(m_i \frac{\sigma_3'}{\sigma_{ci}} + 1 \right)^{0.5}$$

Equation 4-1

In the above equation, σ_1' and σ_3' are the major and minor effective principal stresses at failure, respectively. σ_{ci} is the uniaxial compressive strength of the intact rock material, and m_i is a material constant for intact rock. In order to estimate the rock mass strength, the generalized HB criterion can be used, given by the following equation:

$$\sigma_1' = \sigma_3' + \sigma_{ci} \left(m_b \frac{\sigma_3'}{\sigma_{ci}} + s \right)^{a}$$

Equation 4-2

In this equation, m_b is a reduced value of the intact material constant m_i, and s and a are constants for rock mass. The HB strength parameters (m_i, s and a) can be calculated using the following equations (Hoek et al., 2002):

$$m_b = m_i \, e^{\left[(GSI-100)/_{28-14D} \right]}$$

Equation 4-3

$$s = e^{\left[(GSI-100)/_{9-3D} \right]}$$

Equation 4-4

$$a = 0.5 + \frac{e^{-GSI/_{15}} - e^{-20/_3}}{6}$$

Equation 4-5

According to Hoek et al. (2002), D is a factor that depends on the degree of disturbance as a result of blast damage. The HB strength parameters are functions of the Geological Strength Index (GSI). Using the GSI system presented in Figure 4-1, the reduction in the strength of a rock mass in a given geological condition from that of intact rock can be estimated (Hoek and Brown, 1997). To this end, the surface quality of the joints in addition to the degree of interlocking between intact rock pieces need to be determined in the field.
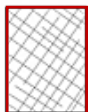
GEOLOGICAL STRENGTH INDEX FOR JOINTED ROCKS

From the lithology, structure and surface conditions of the discontinuities, estimate the average value of GSI. Do not try to be too precise. Quoting a range from 33 to 37 is more realistic than stating that GSI = 35. Note that the table does not apply to structurally controlled failures. Where weak planar structural planes are present in an unfavourable orientation with respect to the excavation face, these will dominate the rock mass behaviour. The shear strength of surfaces in rocks that are prone to deterioration as a result of changes in moisture content will be reduced if water is present. When working with rocks in the fair to very poor categories, a shift to the right may be made for wet conditions. Water pressure is dealt with by effective stress analysis.

STRUCTURE

SURFACE CONDITIONS

DECREASING SURFACE QUALITY →

VERY GOOD — Very rough, fresh unweathered surfaces

GOOD — Rough, slightly weathered, iron stained surfaces

FAIR — Smooth, moderately weathered and altered surfaces

POOR — Slickensided, highly weathered surfaces with compact coatings or fillings or angular fragments

VERY POOR — Slickensided, highly weathered surfaces with soft clay coatings or fillings

DECREASING INTERLOCKING OF ROCK PIECES

INTACT OR MASSIVE - intact rock specimens or massive in situ rock with few widely spaced discontinuities — 90 — 80 — N/A — N/A

BLOCKY - well interlocked undisturbed rock mass consisting of cubical blocks formed by three intersecting discontinuity sets — 70 — 60

VERY BLOCKY- interlocked, partially disturbed mass with multi-faceted angular blocks formed by 4 or more joint sets — 50

BLOCKY/DISTURBED/SEAMY - folded with angular blocks formed by many intersecting discontinuity sets. Persistence of bedding planes or schistosity — 40 — 30

DISINTEGRATED - poorly interlocked, heavily broken rock mass with mixture of angular and rounded rock pieces — 20

LAMINATED/SHEARED - Lack of blockiness due to close spacing of weak schistosity or shear planes — N/A — N/A — 10

Figure 4-1 GSI chart (after Marinos and Hoek, 2000)

4.2.2 S-Shaped and Tri-Linear Strength Envelopes

It is known that the in-situ strength of massive to moderately jointed hard rock masses near underground excavations (i.e., low confinement) is significantly lower than the peak

strength of intact rock obtained from laboratory tests (Bieniawski, 1967; Diederichs, 2003). As an example, the spalling strength at the URL is known to be 30 to 50% of the peak strength of LdB granite obtained from laboratory tests (Martin, 1997). However, conventional approaches used to estimate the rock mass strength, such as the shear-based HB failure criterion with its strength parameters obtained from the GSI system, do not allow the onset of failure to occur at such low stress levels. To overcome this limitation, Diederichs (1999; 2003) proposed an s-shaped strength envelope (see Section 2.5.1.6) in which the rock mass strength under an unconfined condition (i.e., near excavation boundaries) is equal to the crack initiation stress level of intact rock obtained from laboratory UCS tests.

Figure 4-2 shows the typical damage zones around underground openings in hard brittle rock masses and an s-shaped failure criterion for such rock masses. In this figure, the following damage zones around underground excavations are related to the state of induced stress and in situ rock mass strength: 1) Construction Damage Zone (CDZ); 2) Highly Damage Zone (HDZ); 3) Excavation Damage Zone (EDZ); and 4) Excavation Influence Zone (EIZ). Perras and Diederichs (2016) defined the CDZ as a zone in which damage is a function of the excavation method. They described the HDZ as a zone where the development of interconnected macro-fractures is a result of excavation geometry, geological structure and induced stresses. The EDZ contains irreversible micro-damaged rock. Beyond the EDZ is the EIZ where elastic stresses are redistributed from their initial values (i.e., far-field stresses) but with no damage. According to Perras and Diederichs (2016), the CDZ can be eliminated by adjusting or modifying the excavation method while the HDZ and EDZ are inevitable.
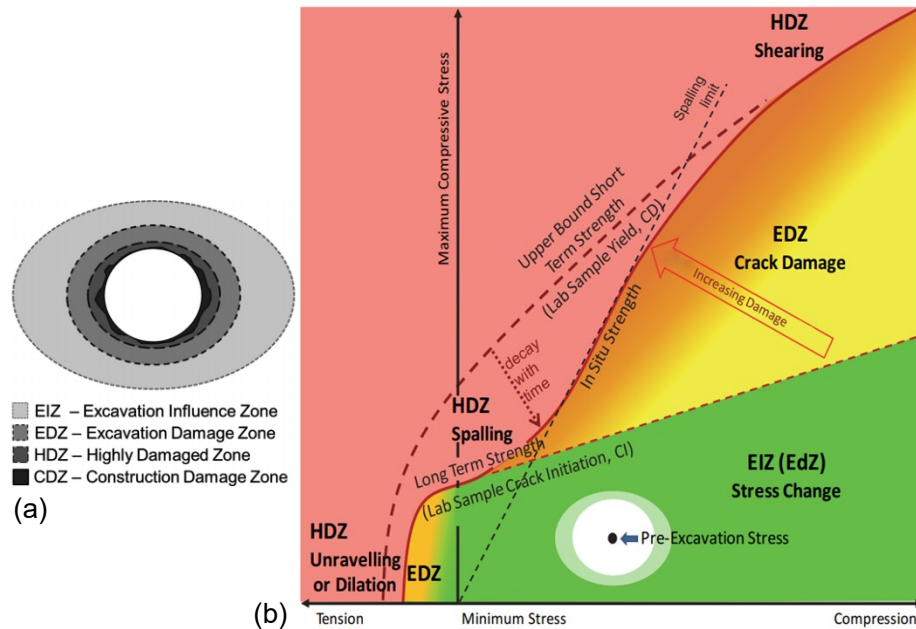
Figure 4-2 a) Damage zones around underground openings (Perras & Diederichs, 2016); and b) in situ strength of hard rocks associated with the state of induced stresses around underground excavations (after Ghazvinian, 2015)

Bewick et al. (2019) proposed the tri-linear strength envelope (Figure 4-3a) based on the s-shaped criterion (Diederichs, 1999; 2003). Bewick et al. (2019) pointed out the changes in the failure process and strength of brittle rocks with increasing confinement and discussed that the rock mass strength envelope for massive to moderately jointed rock masses follow an s- or tri-linear shape (Diederichs, 1999; Diederichs, 2003; Kaiser et al., 2000; Kaiser & Kim, 2015). The proposed envelope along with the HB peak strength envelope obtained from laboratory triaxial tests are shown in Figure 4-3a. According to Bewick et al. (2019), the anticipated range for the rock mass strength starts at the spalling strength obtained from the crack initiation threshold of intact rock at low confinements. The transition in the strength with increasing confinement falls within a spalling limit range, which varies from σ_1/σ_3 = 10 to 20. At higher confinement (i.e., right side of the spalling limit), the confined rock mass strength is approximately 80% of the laboratory peak strength of intact rock.

Bewick et al. (2019) suggested that the tri-linear strength envelope can be approximated by fitting an 'equivalent' HB strength envelope. Figure 4-4b shows this equivalent non-linear fit to tri-linear strength envelope. They suggested that the tri-linear's equivalent HB

strength envelope needs to satisfy the following conditions in terms of the strength of the rock mass: 1) tensile strength of rock mass; 2) unconfined rock mass strength (spalling strength); 3) strength at the spalling limit transition from axial splitting to shear failure; and 4) strength at the transition between shear to ductile where the unstable crack growth suppression limit ($\sigma_1/\sigma_3 = 6$) is exceeded. To be consistent with Bewick et al (2019), the tri-linear's equivalent HB failure criterion is referred to as 'equivalent rock mass strength envelope' in this chapter.
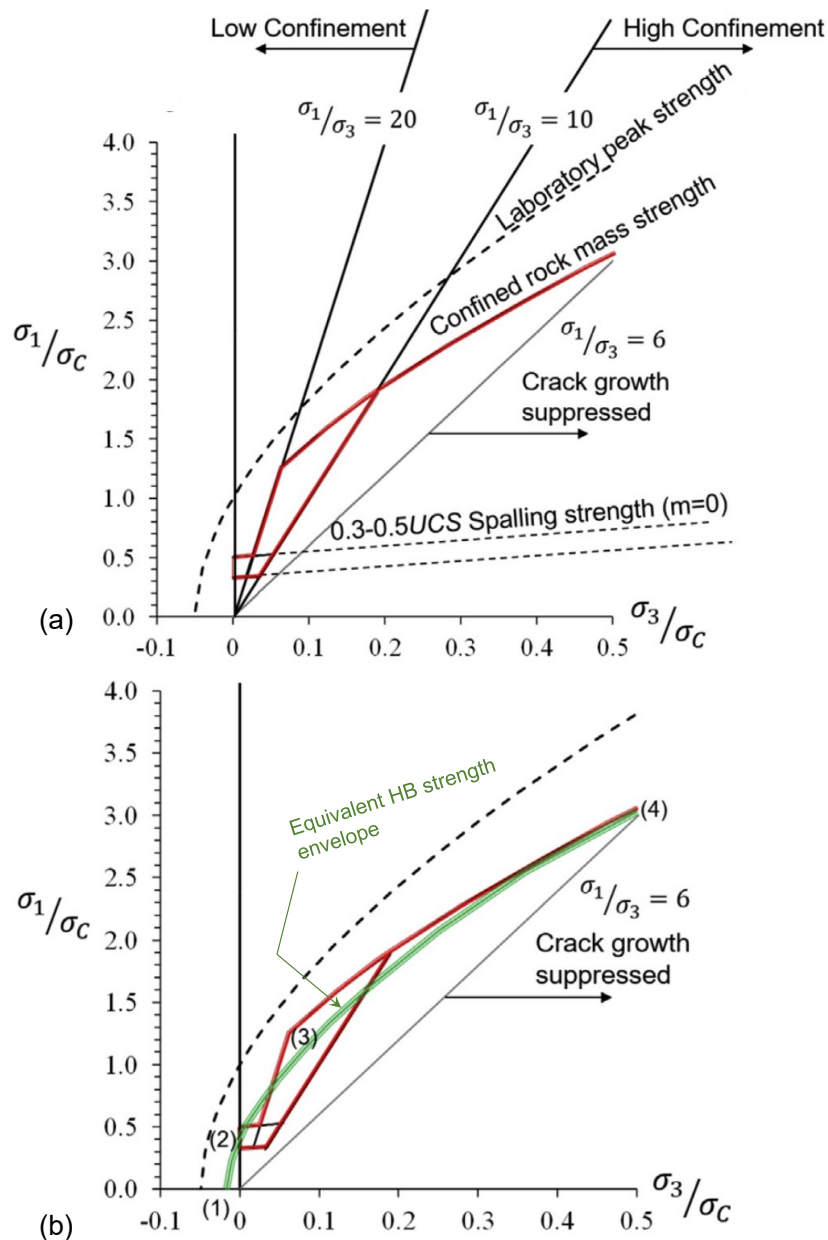
Figure 4-3 a) Tri-linear; and b) equivalent HB (rock mass) strength envelopes (after Bewick et al., 2019)

Figure 4-4a illustrates the tri-linear strength envelope developed for LdB granite showing its higher and lower bounds of the spalling limit. Based on the suggestions of Bewick et al. (2019), the crack initiation threshold of LdB granite as reported by Martin (1993), Martin and Chandler (1994), Martin (1997) and Read et al. (1998) was used to determine the spalling strength. This is followed by the spalling limit which as explained, ranges between σ_1/σ_3 = 10 and 20. To the right of the spalling limit, the long-term strength of LdB granite from Martin (1997) was then used to develop the third component of the tri-linear strength envelope. In addition, the equivalent rock mass strength envelope was developed for LdB granite, which is shown in Figure 4-4b. The following steps adopted from Bahrani and Kaiser (2013) were taken to develop this failure criterion:

1. The intact rock strength envelope obtained from laboratory triaxial test results were used and the GSI value was lowered until the rock mass UCS matched the crack initiation threshold of LdB granite (i.e., first component of the tri-linear strength envelope). The s and a values were determined at this stage.

2. The m_b value was adjusted until the equivalent rock mass strength envelope passes the intersection point of the long-term strength envelope and the crack growth suppression limit.

The equivalent rock mass strength envelope for LdB granite was obtained by applying a GSI of 80 to the intact rock strength envelope. The s and a values were determined to be 0.108 and 0.501, respectively. The m_b value was then adjusted to 11.4. The GSI of 80 was also used to estimate the deformation modulus of the rock mass (i.e., E_{rm} = 57 GPa) using the following equation proposed by Hoek and Diederichs (2006), assuming that D = 0:

$$E_{rm}(MPa) = 100{,}000 \left(\frac{1-\frac{D}{2}}{1+e^{((75+25D)-GSI)/11)}} \right) \qquad \text{Equation 4-6}$$
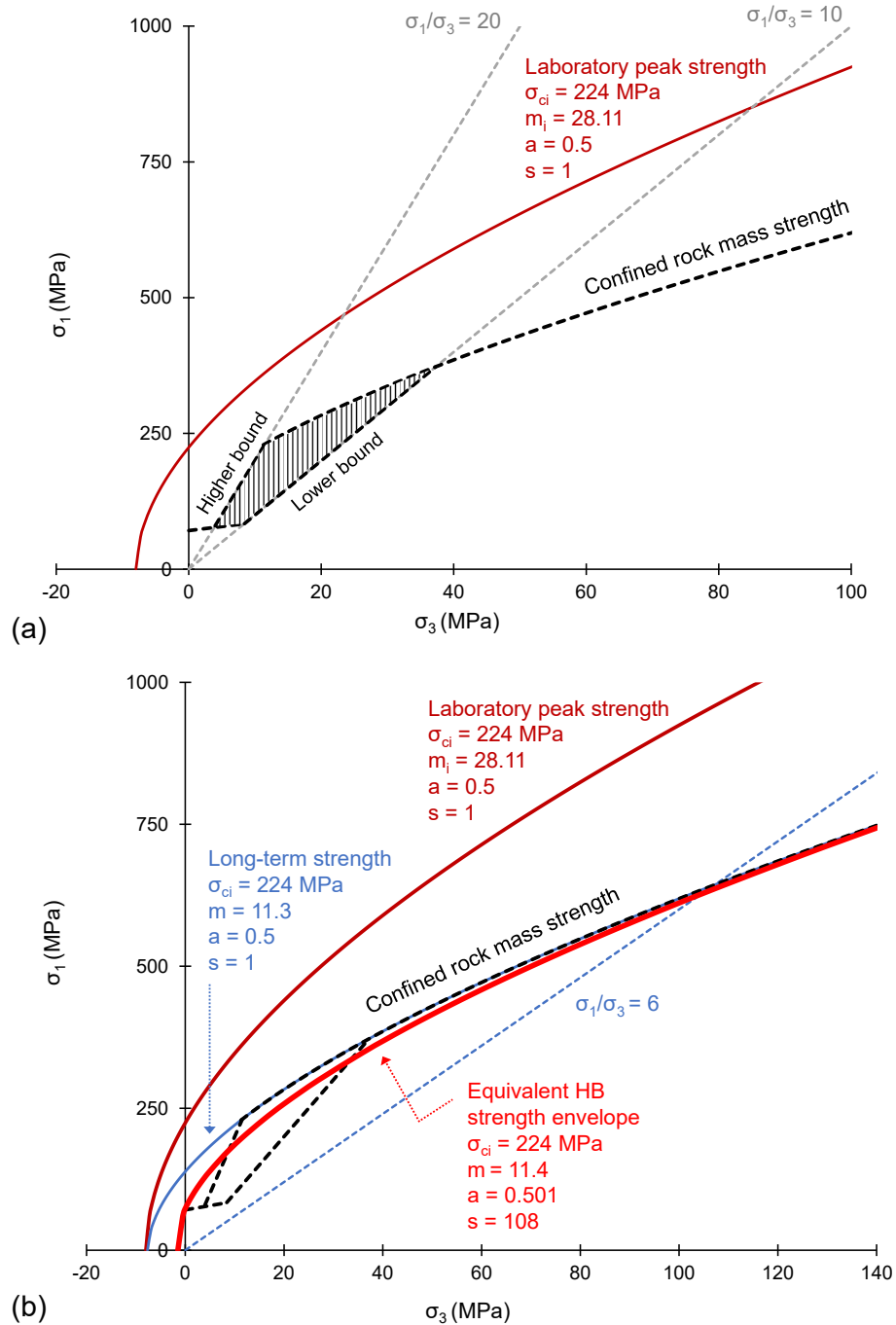
Figure 4-4 a) Tri-linear strength envelope showing upper and lower bounds of spalling limit for LdB granite; and b) equivalent HB (rock mass) strength envelope developed for LdB granite based on Bewick et al. (2019)

In the following sections, the VTM is calibrated against: 1) equivalent HB (rock mass) strength envelope; and 2) tri-linear strength envelope. The calibrated VTMs are then used to simulate the MBE tunnel to evaluate their capabilities in capturing the DoF, EDZ and SoF.

4.3 Simulation of MBE Tunnel Using VTM Calibrated to Tri-Linear's Equivalent HB Rock Mass Strength Envelope

Before calibrating the VTM to the equivalent rock mass strength envelope, the application of homogeneous models with this strength envelope for simulating the v-shaped notch failure was investigated. For this purpose, a homogeneous model of the MBE tunnel was constructed in RS2 and the CS approach was used to mimic the 3D advance of the tunnel face. The excavation stages with the corresponding tunnel core moduli are presented in Table 4-2.

Table 4-1 RS2 stages and corresponding tunnel core Young's moduli used in the simulation of 3D tunnel advance

Stage #	Young's modulus (GPa)	Comment
1	57	Initial stiffness assigned
2	40	
3	30	
4	20	
5	10	
6	5	
7	2	
8	0.5	
9	0.02	
10	0	Core excavated

Since the residual rock mass strength is unknown, four scenarios for post-peak rock mass behaviour, as shown in Figure 4-5, were considered in the simulations: 1) residual rock mass strength equal to its peak strength (i.e., perfectly plastic response); 2) residual rock mass strength equal to 75% of its peak strength; 3) residual rock mass strength equal to 50% of its peak strength; and 4) residual rock mass strength equal to 25% of its peak (equivalent HB) strength envelope.
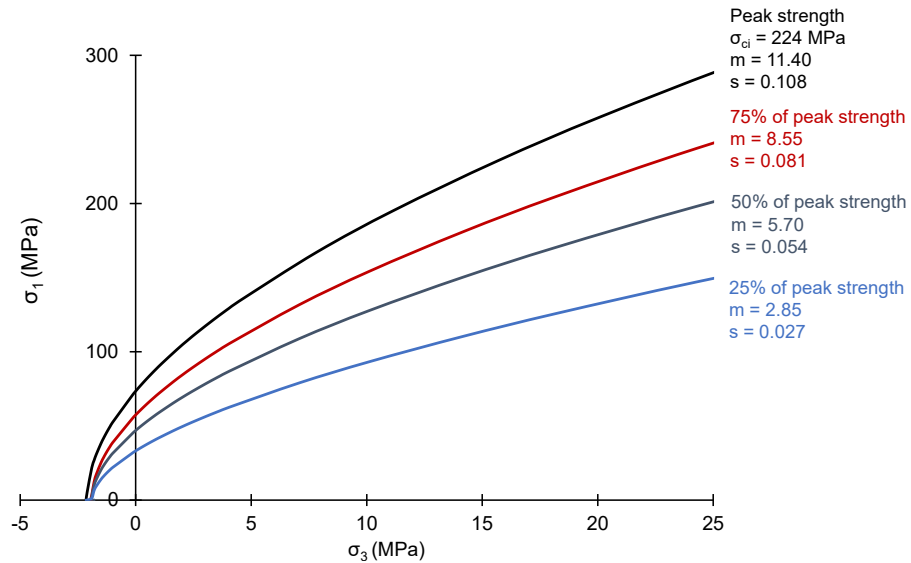
Figure 4-5 Peak and residual HB strengths used in RS2 homogeneous models of MBE tunnel

Figure 4-6 shows that all four scenarios underestimate the DoF at the top and bottom of the URL test tunnel. However, the major concern is the unrealistic lateral extent of the yielded elements; as the residual strength decreases, the extent of yielding increases (Figure 4-6a to d). Furthermore, the failure mechanism captured by this model is not realistic, as the mode of yielded elements around the tunnel is shear. As discussed in the previous chapter, this is due to the fact that homogeneous models do not allow for the generation of localized tensile stresses under compressive loading conditions.
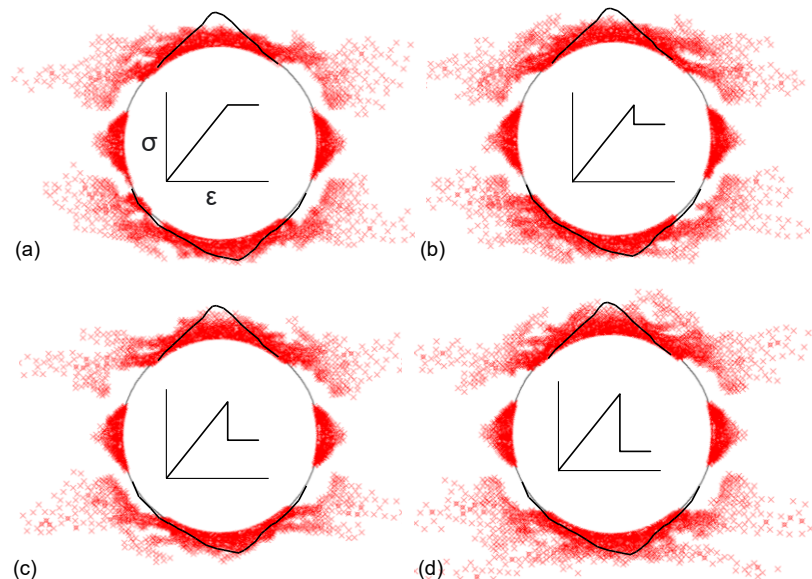
Figure 4-6 Simulated MBE tunnel using RS2 homogeneous models with equivalent rock mass strength envelope with residual strengths equal to: a) peak strength; b) 75% of peak strength; c) 50% of peak strength; and d) 25% of peak strength.

Based on the results of simulations in the previous chapter (i.e., Section 3.4.3), it is expected that the implementation of geometrical heterogeneities into the continuum model would result in capturing realistic failure modes. In the following sections, the equivalent rock mass strength envelope is chosen as the target rock mass strength for the calibration of the VTM and the simulation of v-shaped notch failure around the MBE tunnel.

4.3.1 Calibration Procedure

The micro-properties of the VTM need to be adjusted so that the emergent strength envelope matches the equivalent rock mass strength envelope (Figure 4-4b) for the given range of confinement (i.e., 25 MPa). The assumptions below were made to simplify the calibration procedure and reduce the number of input parameters:

- The Poisson's ratio of the blocks (ν_b) is obtained from laboratory tests. Therefore, $\upsilon_b = 0.25$.

- The Young's modulus of the blocks (E_b) is the same as that of intact rock. Therefore, $E_b = 65$ GPa.

- The joint stiffness ratio (k_n / k_s) is 2.5.

- The peak friction angles of the blocks (ϕ_{pb}) and the block boundaries (ϕ_{pbb}) are equal to the friction angle of intact LdB granite obtained from the results of triaxial tests (i.e., 57°).

- The peak block tensile strength (σ_{tpb}) is the same as that of intact LdB granite obtained from direct tensile tests. Therefore, $\sigma_{tpb} = 6.9$ MPa.

- The residual block and block boundary tensile strength and the residual block boundary cohesion (σ_{trb}, σ_{trbb} and c_{rbb}) were assumed to be 0.1 MPa.

The steps that were taken to calibrate the VTM to the equivalent strength envelope are presented in Figure 4-7.

104
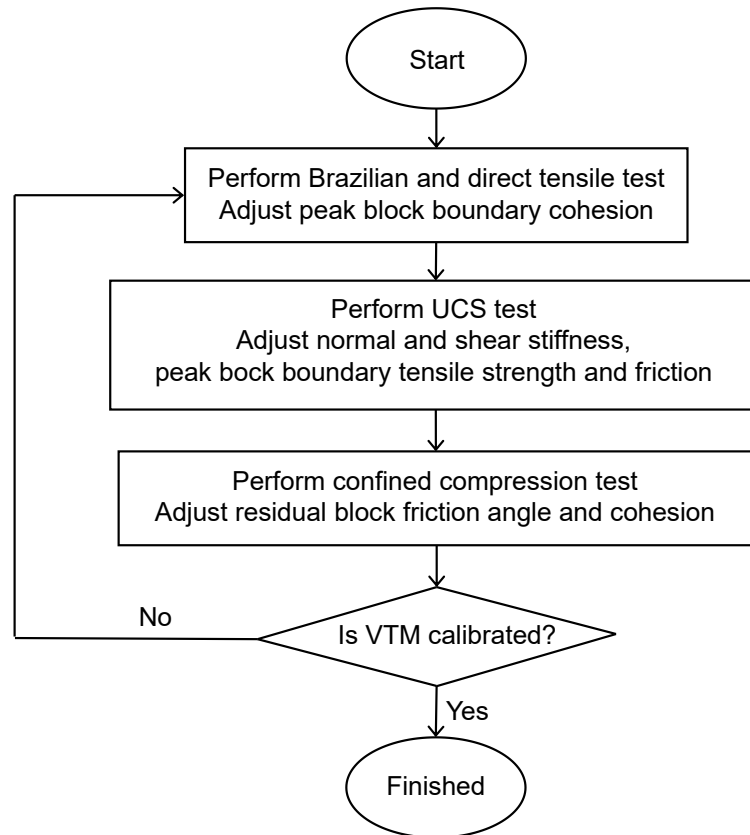
Figure 4-7 Flowchart showing the procedure for calibrating the VTM to equivalent rock mass strength envelope in RS2

The assumptions made to simplify the calibration procedure leave six unknown micro-properties: 1) residual block cohesion (c_{rb}); 2) residual block friction angle (ϕ_{rb}); 3) peak block boundary friction angle (ϕ_{pbb}); 4) peak block boundary tensile strength (σ_{tpbb}); 5 and 6) block boundary normal and shear stiffness (k_n and k_s). Following the procedure presented in Figure 4-7, the BTS and DTS tests were simulated and the c_{pbb} value was adjusted until the tensile strength of the VTM matched the target tensile strength of 2.5 MPa, which is the point where the equivalent rock mass strength envelope intersects the σ_3 axis (see Figure 4-4b). This was followed by performing the UCS test to match the Young's modulus of the VTM to the estimated rock mass deformation modulus (i.e., 57 GPa). For this purpose, the k_n and k_s values were adjusted assuming that k_n/k_s = 2.5. Once the deformation modulus of the VTM was matched to the target value, the confined compression tests were simulated for σ_3 = 5, 10, 15, 20 and 25 MPa. For this purpose, the values of ϕ_{rb} and c_{rb} had to be adjusted. It should be noted that all confined compression tests had to be simulated at the stage of model calibration to ensure that the VTM

strength envelope matches the equivalent rock mass envelope for the entire range of confinement (i.e., up to σ_3 = 25 MPa). The initial micro-properties along with those of calibrated VTM are presented in Table 4-2. The input peak and residual strength envelopes for blocks and block boundaries of the calibrated VTM are illustrated in Figure 4-8.

Table 4-2 Initial and adjusted micro-properties of VTM for calibration against tri-linear's equivalent HB strength envelope

		Micro-properties	Initial value	Adjusted value
Block	Peak strength	Peak cohesion (MPa)	30*	30*
		Peak friction angle (°)	57*	57*
		Peak tensile strength (MPa)	6.9*	6.9*
	Residual strength	Residual cohesion (MPa)	30*	28
		Residual friction angle (°)	57*	50
		Residual tensile strength (MPa)	0.1**	0.1**
	Deformation properties	Young's modulus (GPa)	65*	65*
		Poisson's ratio	0.25*	0.25*
Block boundary	Peak strength	Peak cohesion (MPa)	30*	29
		Peak friction angle (°)	57*	11
		Peak tensile strength (MPa)	6.9*	4
	Residual strength	Residual cohesion (MPa)	0.1**	0.1**
		Residual friction angle (°)	57*	57*
		Residual tensile strength (MPa)	0.1**	0.1**
	Deformation properties	Normal stiffness (MPa/m)	10×10^6	10.5×10^6
		Shear stiffness (MPa/m)	4×10^6	4.1×10^6

* Intact rock properties obtained from laboratory tests (Martin 1993; 1997)
** Assumption (see Section 4.3.1)
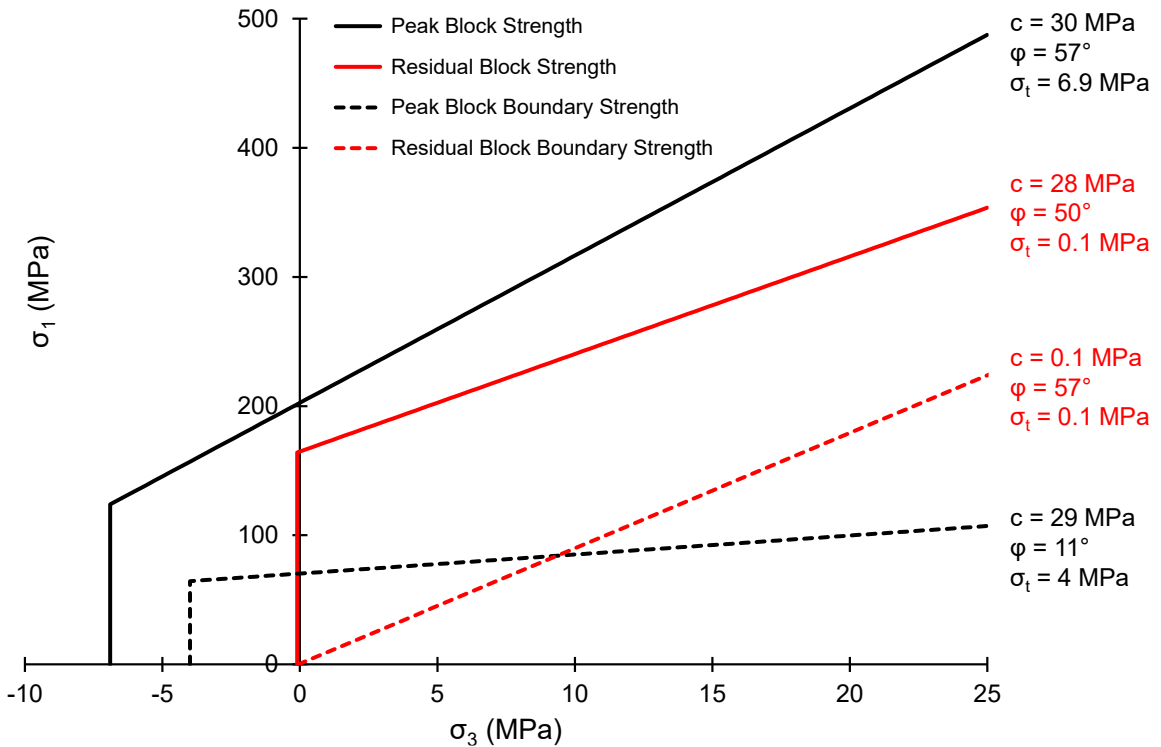
Figure 4-8 Peak and residual strength envelopes for blocks and block boundaries in VTM calibrated to tri-linear's equivalent HB strength envelope

The stress-strain curves of the simulated unconfined and confined compression tests are illustrated in Figure 4-9a. This figure shows that that under an unconfined condition, a sudden stress drop occurs once the peak stress is reached. The drop in the post-peak region occurs at all confining pressures (Figure 4-9a), which is consistent with that of LdB granite (see Figure 2-3). It should be noted that the brittleness in the post-peak region is an emergent behavior of the calibrated VTM and was not considered in the calibration. A comparison between the calibrated VTM and equivalent rock mass strength envelopes are presented in Figure 4-9b, respectively.

Figure 4-10 demonstrates the overall failure modes of the simulated laboratory tests by the calibrated VTM. It can be observed that the simulated macroscopic failure modes are consistent with the VTMs calibrated to the laboratory properties of intact rock (see Figure 3-24).
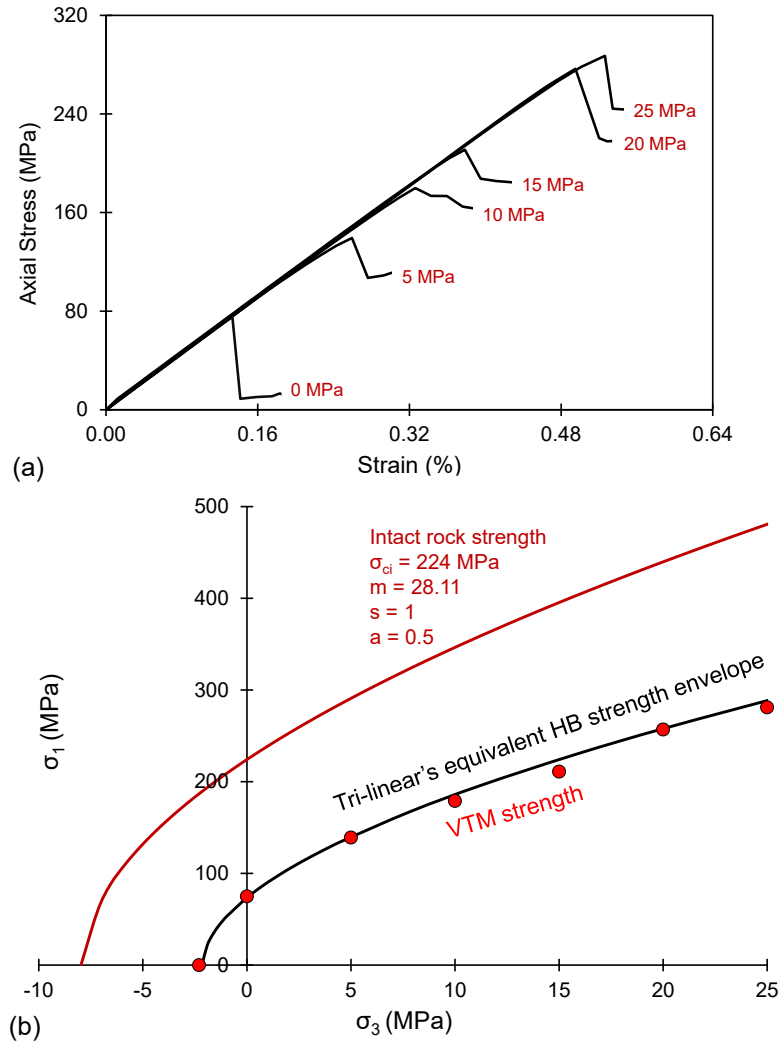
Figure 4-9 a) Stress-strain response of calibrated VTM to tri-linear's equivalent HB strength envelope; and b) strength envelope of calibrated VTM
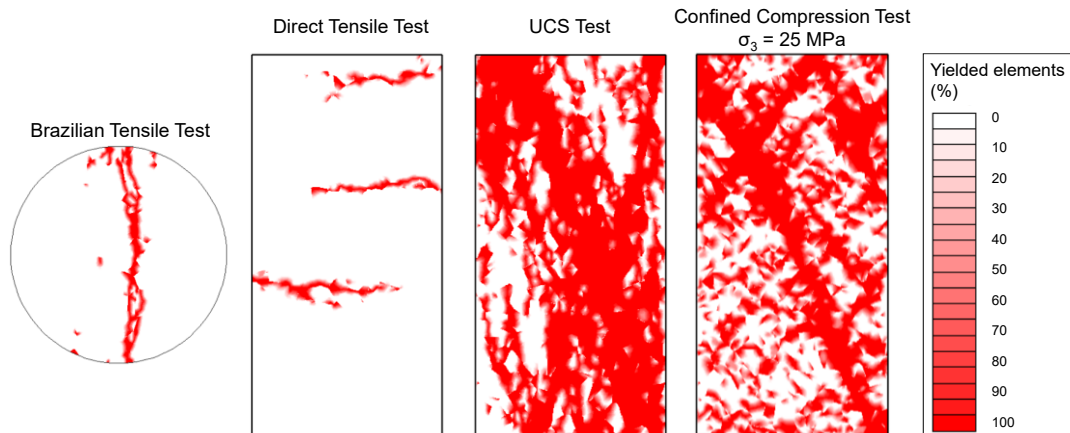
Figure 4-10 Failure modes of simulated laboratory tests using RS2-VTM calibrated to tri-linear's equivalent HB strength envelope

4.3.2 Simulation of V-Shaped Notch Failure

In Chapter 3, the MBE tunnel was simulated with the VTM calibrated to the intact rock properties obtained from laboratory tests (see Figure 3-28). It was demonstrated that the VTM calibrated to the laboratory peak strength of intact rock does not adequately capture the failure and the EDZ around the MBE tunnel. It was discussed that the VTM must be calibrated against the rock mass strength in order to capture the observed failure. In this section, the MBE is simulated using the VTM calibrated to the equivalent rock mass strength envelope.

Figure 4-11 shows the progressive damage leading to failure of the tunnel wall in the VTM calibrated to equivalent rock mass strength envelope. The simulation results indicate that although failure occurs the observed v-shaped notch does not form around the simulated tunnel, and the DoF is underestimated by about 26 cm, compared to the actual depth of failure, which was approximately 53 cm. The extent of failure exceeds the v-shaped notch region, therefore, the SoF is also not captured. Nonetheless, the simulated damage (i.e., block boundary yielding) matches well with the micro-seismic events recorded in the field. This means that the EDZ around the MBE tunnel is captured by the VTM calibrated to equivalent rock mass strength envelope.
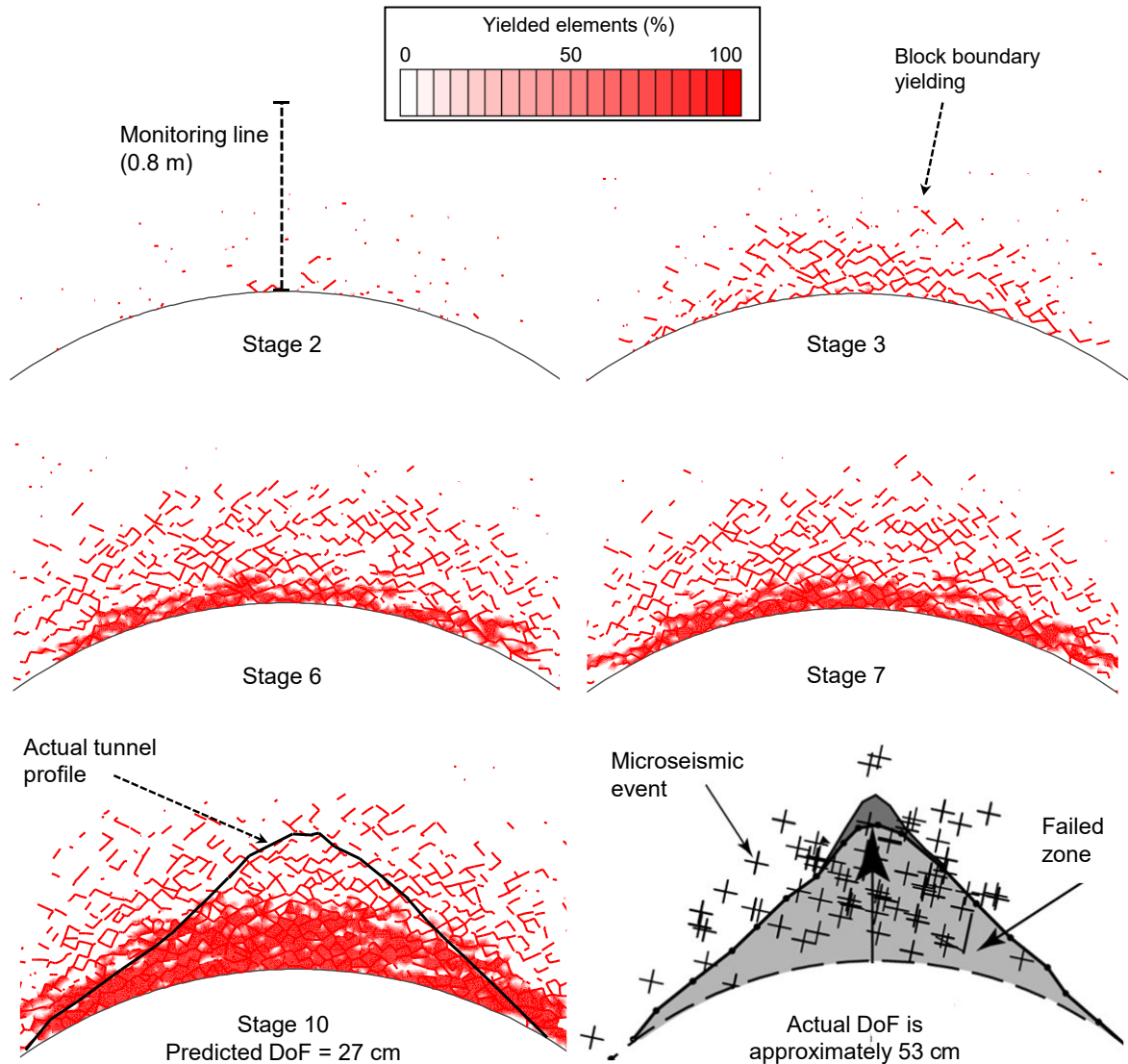
Figure 4-11 Simulation of v-shaped notch failure around MBE tunnel using VTM calibrated to tri-linear's equivalent HB strength envelope in RS2. Actual tunnel profile and recorded micro-seismic events are shown for comparison purposes (after Hajiabdolmajid et al., 2002)

Figure 4-11 shows that the block boundary yielding (i.e., indication of damage) starts at Stage 2. The block yielding (i.e., indication of failure) follows the damage in later stages of the simulation. This figure indicates that the EDZ is replicated by this model as the depth of block boundary yielding is consistent the micro-seismic events recorded in the field. The simulated failure mechanism is demonstrated in Figure 4-12. As can be seen in this figure, the blocks are mainly yielded in tension due to high compressive stresses, which is consistent with field observations.
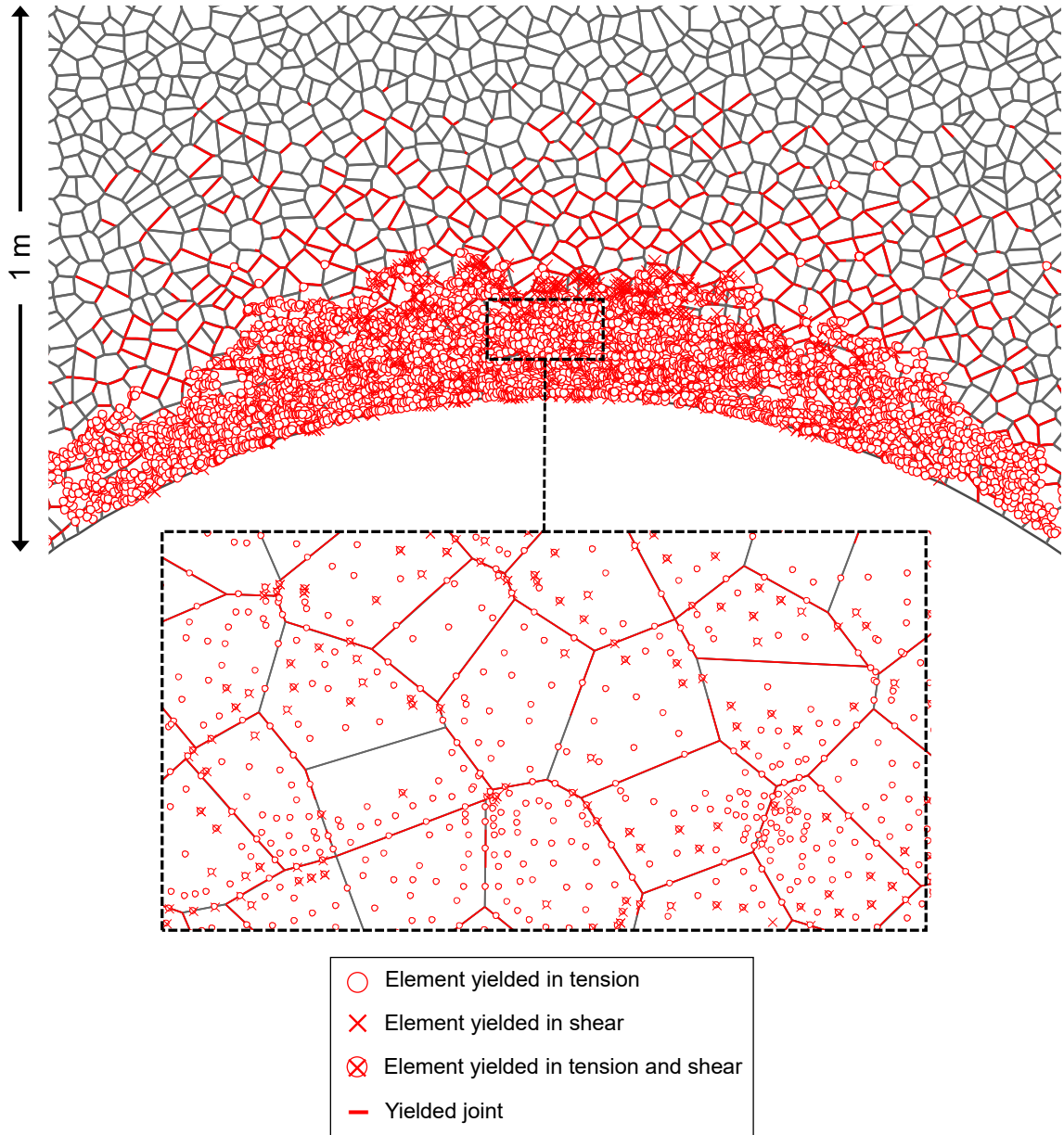
Figure 4-12 Simulated failure mechanism of MBE tunnel in RS2-VTM calibrated to tri-linear's equivalent HB strength envelope

Figure 4-13a and b show the distributions of σ_1 and σ_3 along a vertical monitoring line at the crown of the tunnel obtained from the VTM calibrated to equivalent rock mass strength envelope and a homogeneous elastic model. The comparison between the stresses from these models shows that when there is no block yielding, both σ_1 and σ_3 in the VTM follow the general trend of stresses in the homogenous model; σ_1 and σ_3 decrease as the distance from excavation boundary increases. This figure also shows that the σ_1 and σ_3 values suddenly decrease near the excavation boundary when finite element

yielding occurs. By analyzing the change in the trend of σ_1 and σ_3 in Figure 4-13a and b, it is possible to determine the depth of failure. In Figure 4-13a and b, the DoF around the MBE tunnel, which is approximately 53 cm, is compared with the that predicted by the calibrated VTM, which is about 27 cm. It is therefore concluded that the VTM calibrated to the equivalent rock mass strength envelope underpredicts the DoF by 26 cm.

(a)

(b)
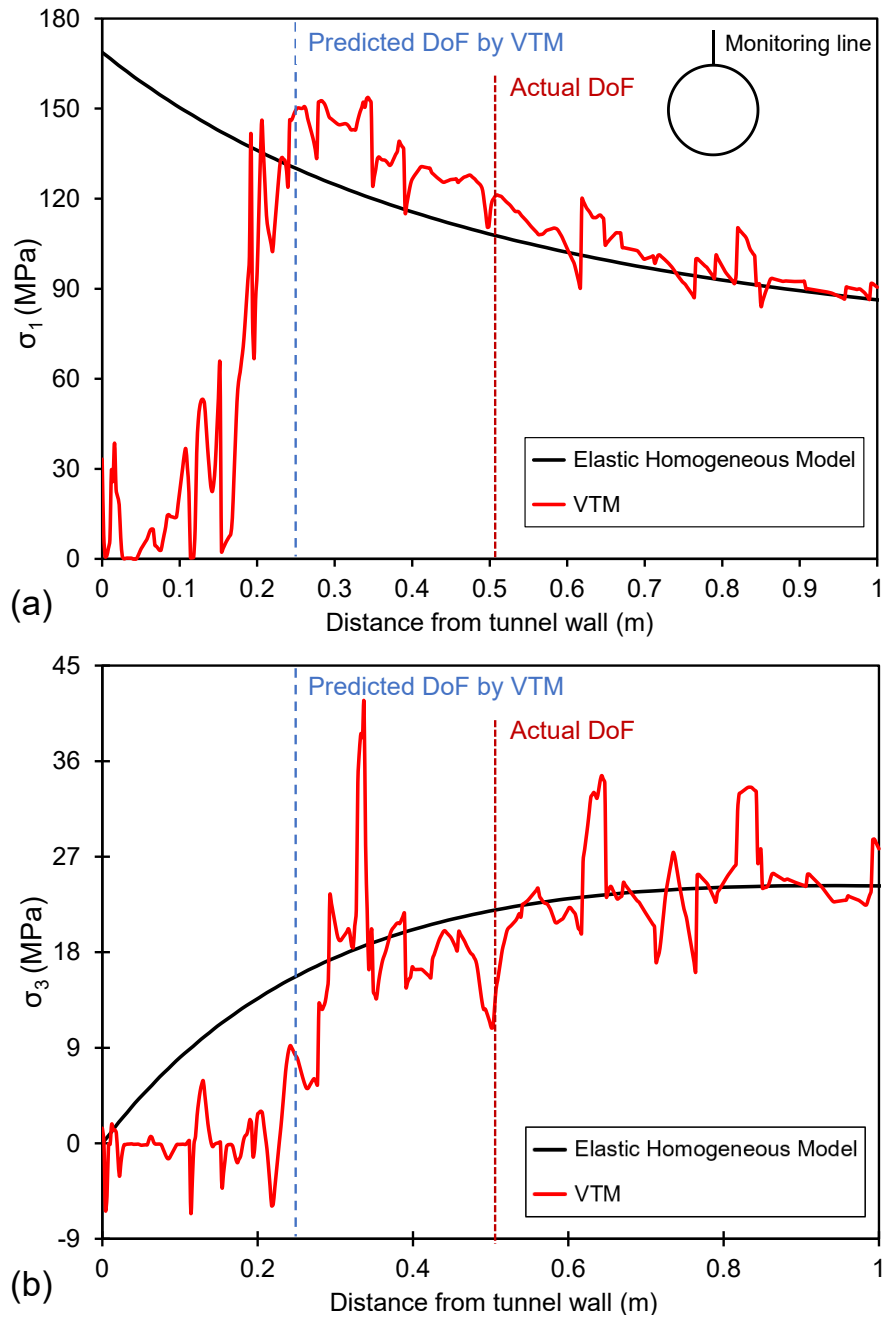
Figure 4-13 Distribution of: a) σ_1; and b) σ_3 along the monitoring line following tunnel core excavation obtained from elastic homogeneous model and VTM calibrated to equivalent rock mass strength envelope

4.4 Simulation of MBE Tunnel Using VTM Calibrated to Tri-Linear Strength Envelope

In the previous section, the VTM was calibrated to the tri-linear's equivalent rock mass strength envelope which led to the underestimation of the DoF and overestimation of the extent of failure. In this section, the VTM is calibrated against the tri-linear strength envelope (see Figure 4-3 and Section 4.2.2) by simulating standard laboratory tests. It is expected that by using a heterogeneous model (i.e., VTM) and adopting proper rock mass strength envelope, the observed EDZ, DoF and SoF should be captured with a realistic failure mode.

4.4.1 Calibration Procedure

As shown in Figure 4-3, the tri-linear strength envelope is essentially a compressive failure criterion. Therefore, the simulation of the BTS and DTS tests for the calibration of the VTM is not necessary. However, the BTS and DTS tests were simulated once the VTM was calibrated to the target strength to estimate the tensile strength of the rock mass. Note that the assumptions made to simplify the calibration are similar to those used for the calibration of VTM to the equivalent rock mass strength envelope (see Section 4.3.1) with the exception of the value of ϕ_{pb} is unknown and therefore needed to be adjusted in the calibration process. The flowchart shown in Figure 4-14 demonstrates the steps that were taken to calibrate the VTM to the tri-linear strength envelope. As can be seen in this figure, the VTM calibration does not require the simulation of BTS and DTS tests, but the MBE tunnel simulation is part of the calibration process.
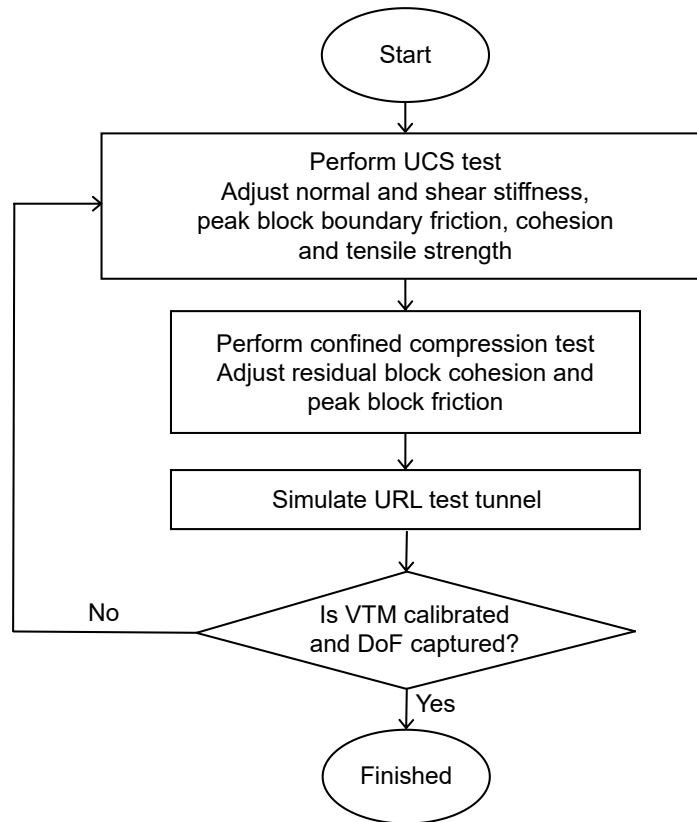
Figure 4-14 Flowchart showing the procedure to calibrate RS2-VTM to tri-linear strength envelope

Considering the assumptions, only seven unknown input parameters had to be adjusted during the calibration process: 1) peak block friction angle (ϕ_{pb}); 2) residual block cohesion (c_{rb}); 3) peak block boundary cohesion (c_{pbb}); 4) peak block boundary friction angle (ϕ_{pbb}); 5) peak block boundary tensile strength (σ_{tpbb}); 6 and 7) block boundary normal and shear stiffness (k_n and k_s). In the first stage of model calibration, the UCS test was simulated and the k_n and k_s values were adjusted until the VTM Young's modulus matched the estimated rock mass deformation modulus (i.e., 57 GPa). Note that the k_n/k_s ratio was assumed to be 2.5, thus, either k_n or k_s had to be adjusted. In the next step, the values of ϕ_{pbb}, c_{pbb} and σ_{tpbb} were adjusted until the VTM was calibrated to the target UCS (see Figure 4-3b). Next, the confined compression tests were simulated, and the remaining unknown parameters (c_{rb} and ϕ_{pb}) were adjusted until the confined strength matched that of the tri-linear strength envelope.

As mentioned earlier, the spalling limit of the rock mass ranges between $\sigma_1/\sigma_3 = 10$ and 20. Since the exact spalling limit of LdB granite is unknown, it had to be back analyzed by

simulating the v-shaped notch failure around the MBE tunnel. Therefore, in the next stage of model calibration, the MBE tunnel was simulated. The simulation results indicated that among the seven unknown parameters, the peak block friction angle (ϕ_{pb}) and the residual block cohesion (c_{rb}) control the DoF and SoF around the MBE tunnel, and therefore, had be re-adjusted with respect to the following conditions: 1) the DoF must match the field observations; and 2) the confined strength of the VTM must match the estimated confined rock mass strength. Once the VTM was calibrated, the BTS and DTS were simulated to estimate the tensile strength of the rock mass.

Figure 4-15 shows the peak and residual strength envelopes for the block and block boundary of the calibrated VTM. It was found that the strain-independent CWFS constitutive law for blocks and block boundaries would lead to an emergent strength envelope for the VTM that follows the s-shaped failure envelope proposed by Diederichs (2003). The initial and adjusted micro-properties of the calibrated VTM are given in Table 4-3.
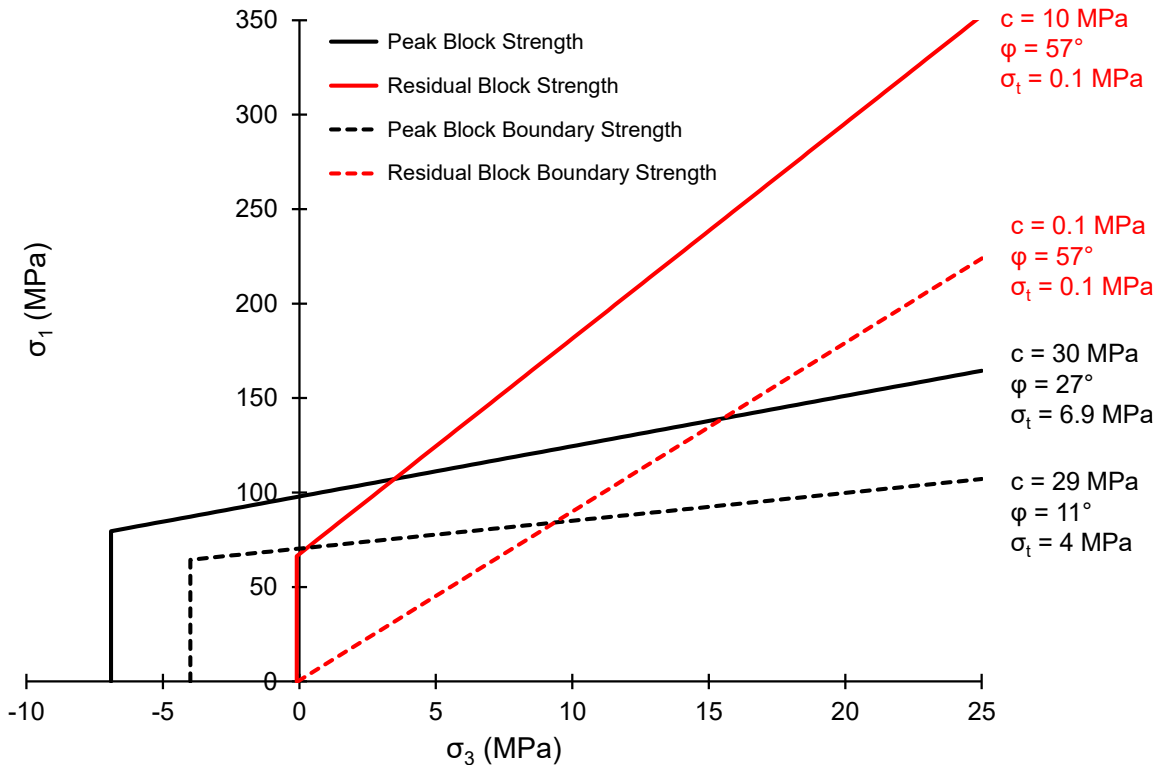
Figure 4-15 Peak and residual strength envelopes of block and block boundaries for VTM calibrated to tri-linear strength envelope

Table 4-3 Initial and adjusted micro-properties of VTM calibrated to tri-linear strength envelope

		Micro-properties	Initial value	Adjusted value
Block	Peak strength	Cohesion (MPa)	30*	30*
		Friction angle (°)	57*	27
		Tensile strength (MPa)	6.9*	6.9*
	Residual strength	Cohesion (MPa)	30*	10
		Friction angle (°)	57*	57*
		Tensile strength (MPa)	0.1**	0.1**
	Deformation properties	Young's modulus (GPa)	65*	65*
		Poisson's ratio	0.25*	0.25*
Block boundary	Peak strength	Cohesion (MPa)	30*	29
		Friction angle (°)	57*	11
		Tensile strength (MPa)	6.9*	4
	Residual strength	Cohesion (MPa)	0.1**	0.1**
		Friction angle (°)	57*	57*
		Tensile strength (MPa)	0.1**	0.1**
	Deformation properties	Normal stiffness (MPa/m)	10×10^6	10.5×10^6
		Shear stiffness (MPa/m)	4×10^6	4.1×10^6

* Intact rock properties obtained from laboratory tests (Martin 1993; 1997)
** Assumption (see Section 4.4.1)

Figure 4-16a presents the stress-strain response of the simulated unconfined and confined compression tests. It shows that the post-peak response of the calibrated VTM is brittle, independent of the confinement. This brittleness is consistent with that of LdB granite (see Figure 2-3a) although, the post-peak behavior was not part of the calibration process. Figure 4-16b demonstrates that the strength envelope follows the crack initiation threshold of LdB granite at low confinements ($\sigma_3 < 5$ MPa) and the spalling limit at higher confinements. Note that the back analyzed spalling limit, falls within the lower and higher bounds of this limit for LdB granite (see Figure 4-3b). The non-linearity in the emergent strength envelope is mainly controlled by the four input strength envelopes for the block and block boundary illustrated in Figure 4-15. As mentioned earlier, once the

VTM was calibrated, the BTS and DTS tests were simulated. It was found that the tensile strength of the calibrated VTM is 3.8 MPa.

(a)

(b)
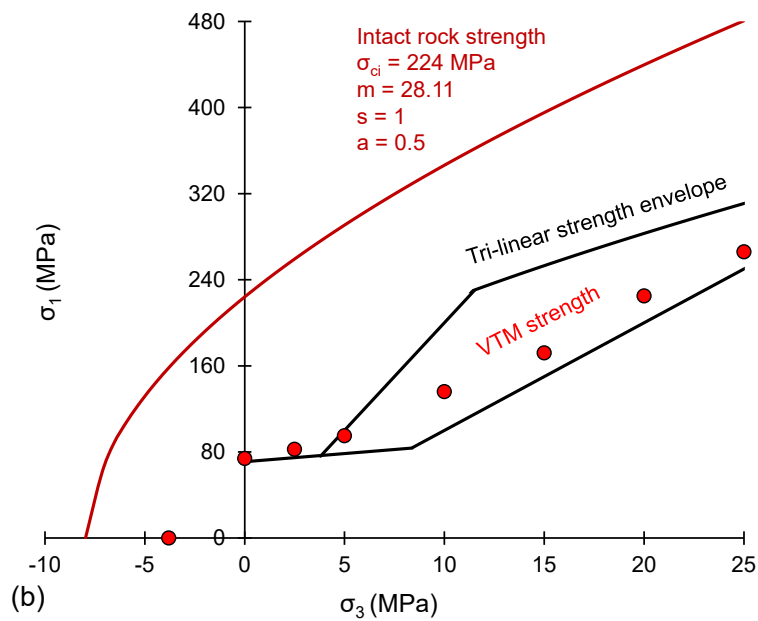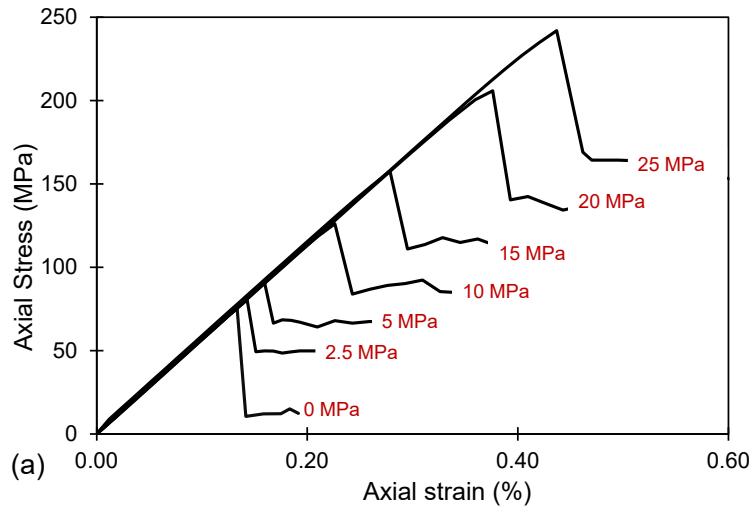
Figure 4-16 a) Stress-strain response of VTM calibrated to tri-linear strength envelope; and b) strength envelope of calibrated VTM

4.4.2 Simulation of V-Shaped Notch Failure

Using the micro-properties of the calibrated VTM (Table 4-3), the MBE tunnel was simulated with the same boundary conditions as those shown in Figure 3-25. Figure 4-17 shows the results of this simulation. It can be seen in this figure that the block boundary

yielding initiates at Stage 2. As a reminder, block boundary yielding was found to be an indication of damage while block yielding corresponds to failure (see Sections 3.4.3.3 and 3.4.5.2). Figure 4-17 shows that the damage is followed by block yielding starting from Stage 3 and accumulates as the core is gradually softened and eventually excavated at Stage 10. The density of block yielding increases with each stage until the v-shaped notch is captured. This figure clearly shows that the depth and shape of failure around the MBE tunnel are well captured by this model. It also illustrates that the extent of block boundary yielding at the final stage is consistent with the micro-seismic events in the field, thus, the EDZ is also captured.
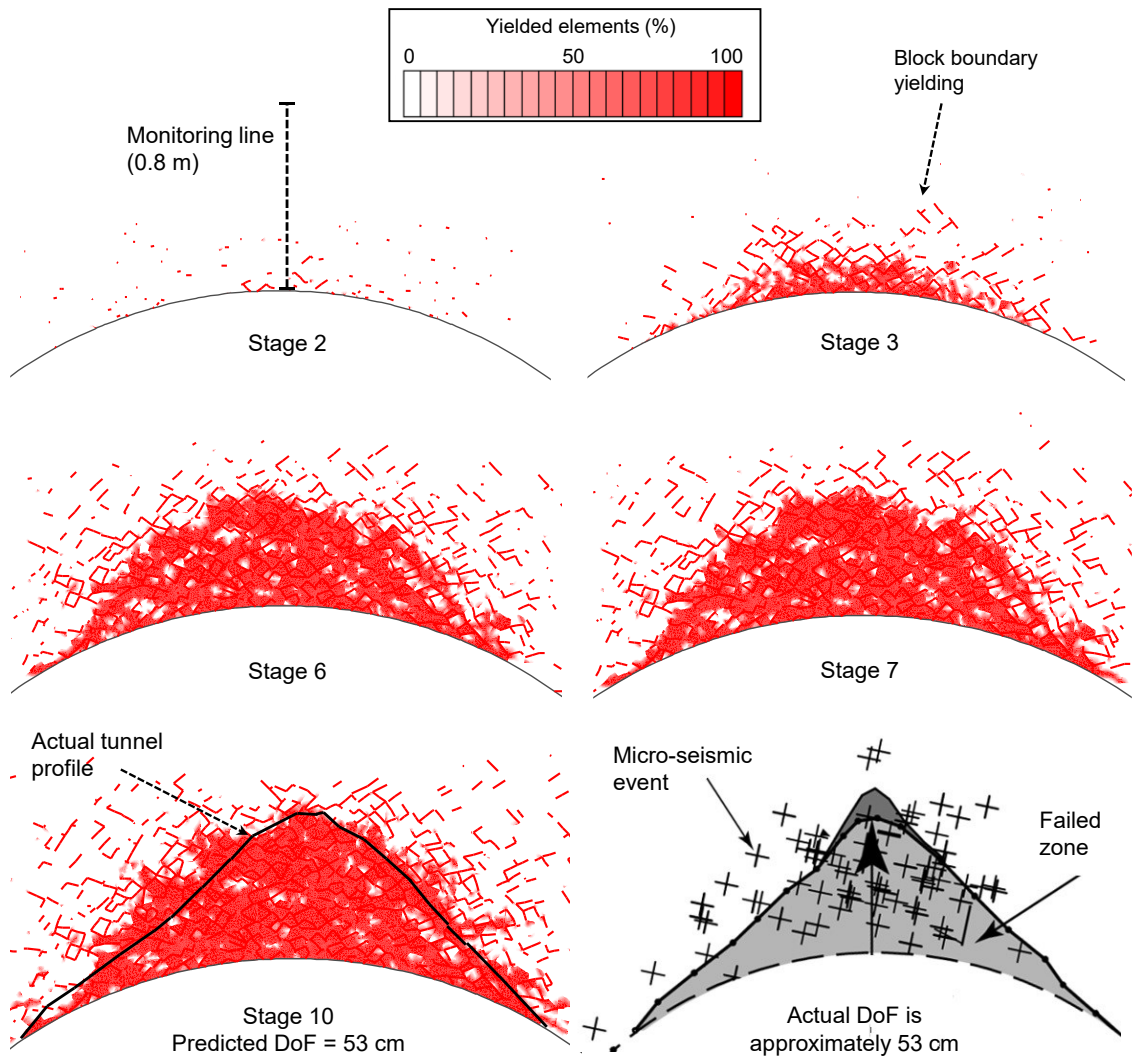
Figure 4-17 Simulation of v-shaped notch failure around MBE tunnel using VTM calibrated to tri-linear envelope in RS2. Actual tunnel profile and recorded micro-seismic events are illustrated for comparison purposes (after Hajiabdolmajid et al., 2002)

Figure 4-18 provides more detailed information about the failure mechanism near the tunnel simulated using the RS2-VTM calibrated to tri-linear strength envelope. Figure 4-18b shows that the failure is dominated by block tensile yielding near the excavation boundary, where maximum tangential stress occurs. With increasing distance from the tunnel boundary (i.e., increasing confinement), the number of elements yielded in shear increases. Therefore, it is concluded that the failure mechanism captured by the calibrated VTM is consistent field observations described by Martin and Chandler (1994) and Martin (1997).
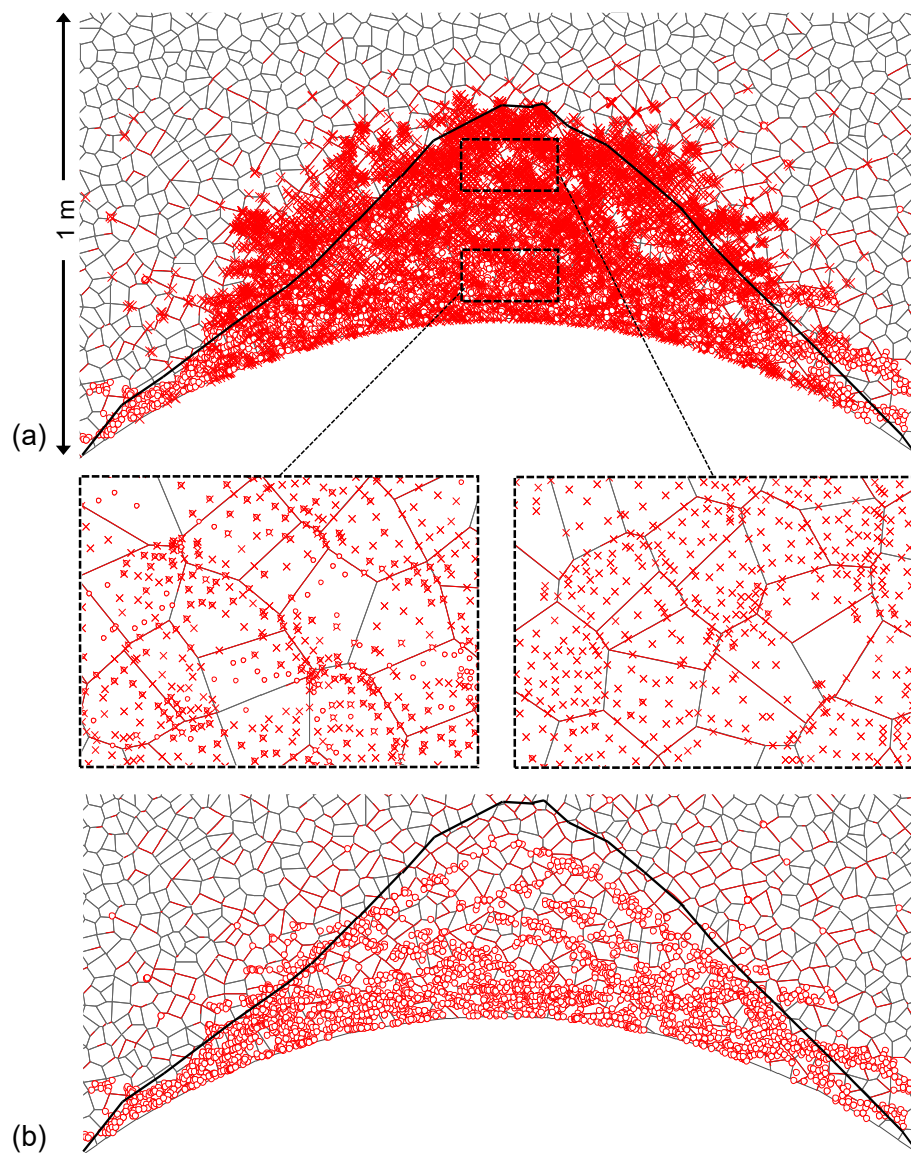
Figure 4-18 a) Simulated failure mechanism of MBE tunnel using VTM calibrated to tri-linear strength envelope in RS2; and b) elements yielded purely in tension near the tunnel

The failure mechanism around the MBE tunnel simulated using the calibrated RS2-VTM (Figure 4-18) is also consistent with other advanced numerical models based on the Distinct Element Method, such as those by Dadashzadeh (2020) and Potyondy and Cundall (2004). Dadashzadeh (2020) calibrated a UDEC-GBM to the laboratory properties of Cobourg limestone and upscaled it to obtain the rock mass properties. The blocks in the UDEC-GBM were assumed to be elastic, thus, the model was calibrated by adjusting the block boundary deformation and strength properties as well as the block deformation properties. Figure 4-19a shows the target strength envelope, which was estimated based on the DISL approach as well as the peak strengths of calibrated UDEC-GBM. In this figure, 'DISL initiation' and 'DISL spalling' correspond to the peak and residual strengths, respectively, which were obtained from the stress-strain curves of triaxial compression test simulations. After upscaling the model, Dadashzadeh (2020) simulated a tunnel to predict the depth and shape of failure, as shown in Figure 4-19b. In this figure, the fractures in the vicinity of the tunnel wall are predominantly developed due to tensile failure. However, further away from the tunnel boundary, the induced fractures are mainly in shear.

(a)

(b)

Figure 4-19 a) Peak laboratory strength envelope for Cobourg limestone, composite in situ strength envelope, and the strength of calibrated UDEC-GBM; and b) simulated damage and v-shaped notch failure around a tunnel using upscaled UDEC-GBM (Dadashzadeh, 2020)

Figure 4-20 shows the redistribution of stresses (σ_1 and σ_3) along a vertical monitoring line at the crown of the tunnel following the excavation from the VTM and the homogeneous elastic model. The trend of stress changes in the VTM is clearly different from that of the homogeneous elastic model. The stress drops (both in σ_1 and σ_3 values) are due to block yielding near the excavation boundary.

121

Figure 4-20 Distribution of: a) σ_1; and b) σ_3 along the monitoring line following tunnel excavation obtained from homogeneous elastic model and VTM calibrated to tri-linear strength envelope

The comparison between the actual DoF and that predicted by the VTM calibrated to the tri-linear strength envelope is shown in Figure 4-20. This figure shows that the actual DoF

around the MBE tunnel (i.e., approximately 53 cm) corresponds to the distance from the tunnel boundary at which the stress drop occurs. The negative σ_3 around the excavation boundary in Figure 4-20b suggests that the rock mass experiences localized tensile stresses due to heterogeneity. The confinement increases promptly above the tip of the v-shaped notch to values higher than those of the homogeneous elastic model. This confinement increase inhibited the propagation of fractures and the extension of failure further into the rock mass above the tunnel.

4.5   Sensitivity Analysis on VTM Micro-Properties

Calibrating the RS2-VTM to the tri-linear strength envelope required adjusting the values of two block and three block boundary parameters (Figure 4-14) from the initial assumed values in Table 4-3. Following a comprehensive sensitivity analysis conducted on the micro-properties of the VTM, it was found that changes in block boundary strength parameters only slightly affect the DoF around the MBE tunnel whereas the block micro-properties significantly impact the emergent strength envelope, and the DoF and SoF around the tunnel. Thus, in this section the results of sensitivity analysis on two block micro-properties of the VTM that were adjusted in the calibration process are presented: 1) peak block friction angle (ϕ_{pb}); and 2) residual block cohesion (c_{rb}). In order to better understand the effects of these input parameters on the shape of the emergent strength envelopes and the depth, shape and extent of failure around the MBE tunnel, systematic sensitivity analyses on these micro-properties were carried out and the results are presented in the following section.

4.5.1   Peak Block Friction Angle

In this section, the influence of ϕ_{pb} on the emergent strength envelope and the depth, shape and extent of failure around the test tunnel was studied. For this reason, the value of this parameter was changed from 20° to 45°. As a reminder, the value of ϕ_{pb} in the VTM calibrated to tri-linear strength envelope is 27° (Table 4-3). Figure 4-21 shows the results of sensitivity analysis on the VTM strength envelope.
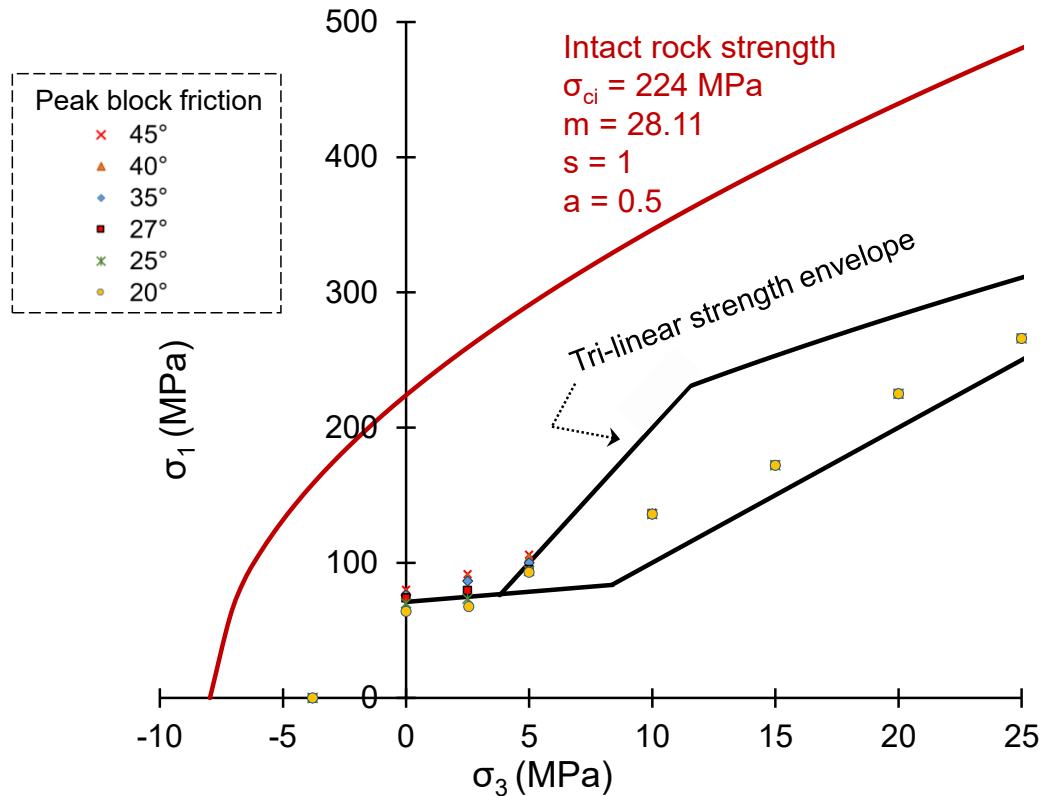
Figure 4-21 Influence of peak block friction angle (ϕ_{pb}) on VTM strength envelope

As illustrated in Figure 4-21, ϕ_{pb} mainly controls the strength of the VTM at low confinement ($\sigma_3 < 5$ MPa) (i.e., the first component of the tri-linear strength envelope, which is equal to the crack initiation threshold of intact rock). It was found that a ϕ_{pb} of 20° results in a UCS of 64 MPa, while a value of 45° for ϕ_{pb} leads to a UCS of 79 MPa. Furthermore, the tensile strength of the VTM was found not to be sensitive to this parameter. The strength at higher confinement (5 MPa < σ_3 < 25 MPa) is also not influenced by ϕ_{pb}. However, as depicted in Figure 4-22, the depth and extent of failure around the test tunnel is sensitive to this parameter. This figure shows that for ϕ_{pb} values greater than 27°, the DoF is underestimated. For ϕ_{pb} values smaller than 27°, the DoF around MBE tunnel is matched but the extent of failure is overestimated.
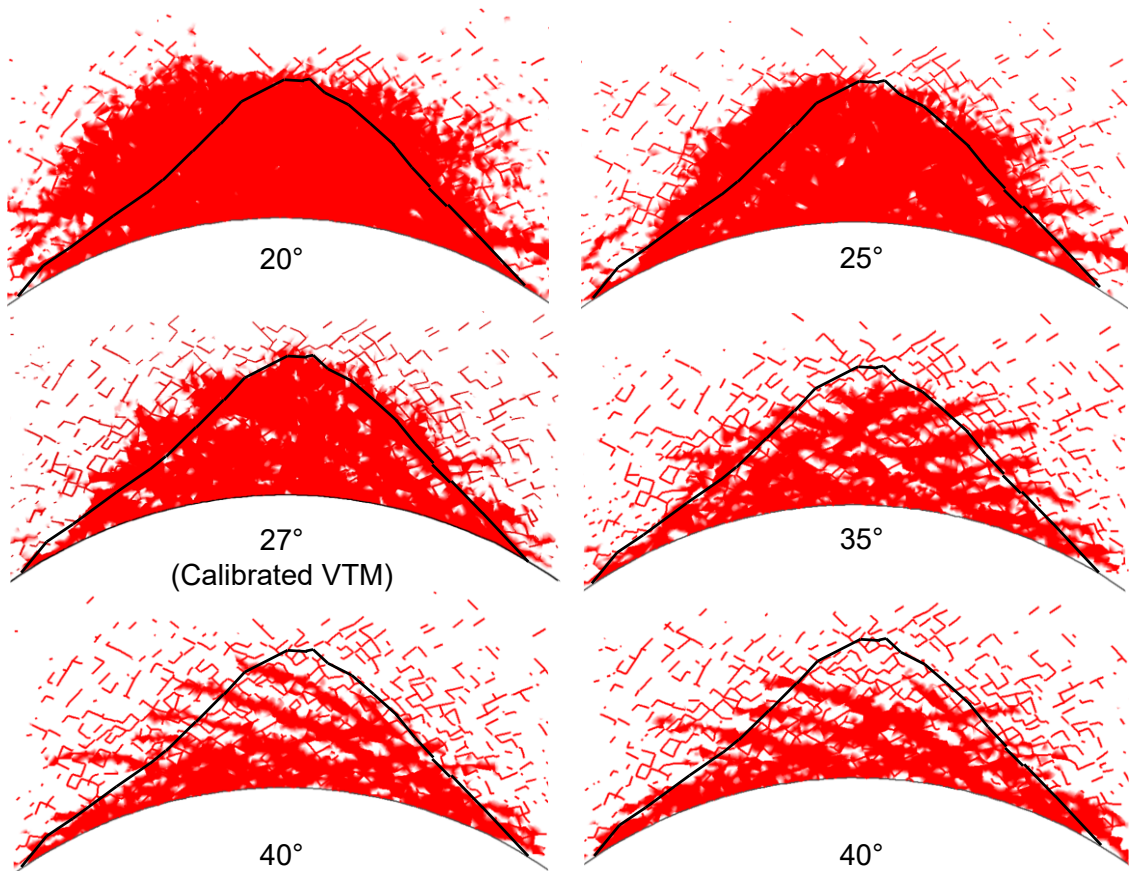
Figure 4-22 Influence of peak block friction angle (ϕ_{pb}) on depth and shape of failure around MBE tunnel

4.5.2 Residual Block Cohesion

In this section, the residual block cohesion (c_{rb}) was varied from 0.1 MPa to 30 MPa (equal to that of intact rock) to assess the influence of this parameter on the VTM strength and the depth, shape and extent of failure around the test tunnel. As a reminder, the value of c_{rb} in the VTM calibrated to tri-linear strength envelope is 10 MPa (Table 4-3). The results of sensitivity analysis on the emergent strength envelope of the VTM are presented in the following figure.
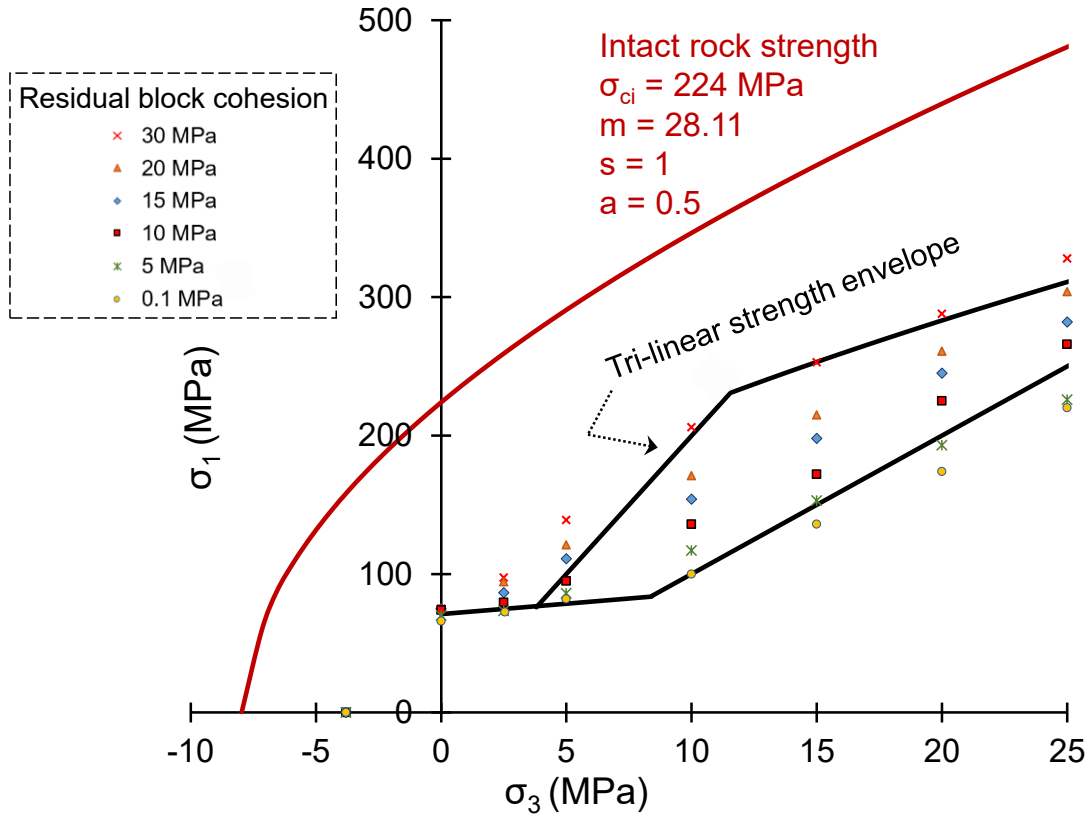
Figure 4-23 Influence of residual block cohesion (c_{rb}) on VTM strength envelope

Figure 4-23 shows that c_{rb} controls the emergent VTM strength for the entire range of confinement (5 MPa < σ_3 < 25 MPa). As expected, the VTM tensile strength is not sensitive to this parameter, as it is mainly controlled by the block and block boundary tensile strength. Figure 4-24 demonstrates how the large-scale failure mode is influenced by c_{rb} value. This figure shows that both the DoF and SoF are sensitive to this parameter. For the c_{rb} values smaller than 10 MPa, the DoF is overestimated while for values greater than 10 MPa, the DoF is underestimated.
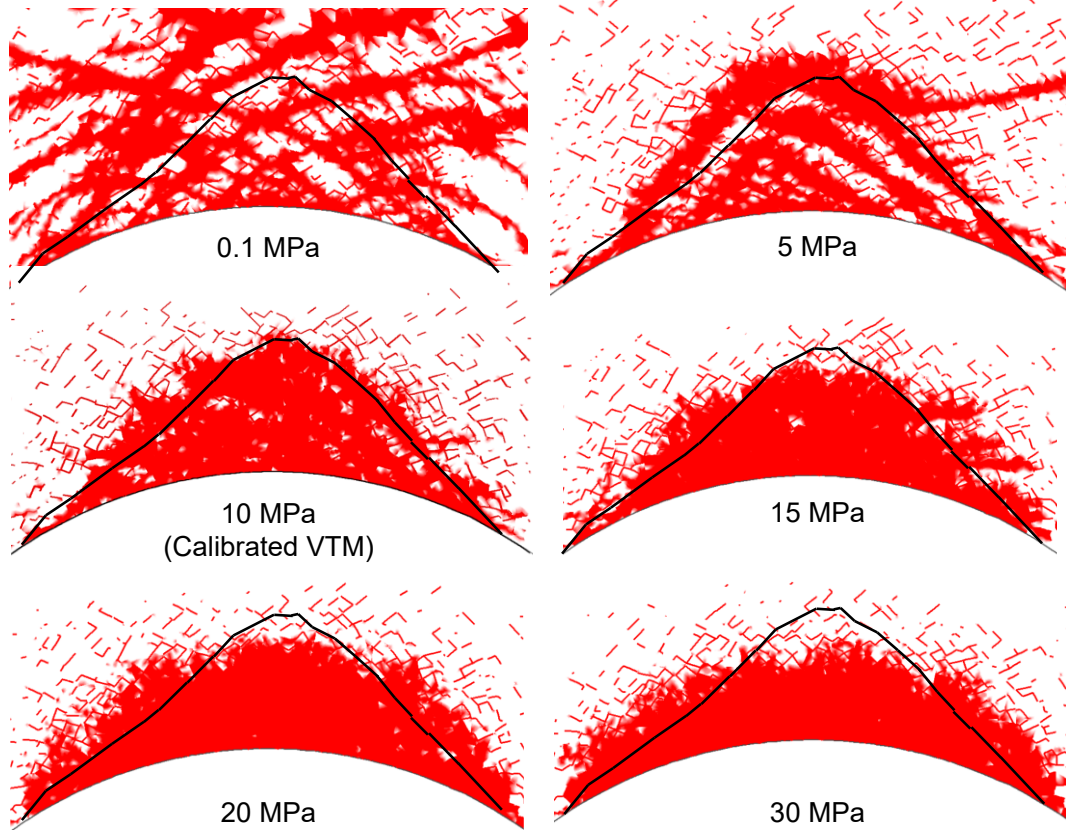
Figure 4-24 Influence of residual block cohesion (c_{rb}) on depth and shape of failure around MBE tunnel

4.6 Discussion

The maximum level of confinement around the MBE tunnel following the excavation of the tunnel obtained from homogeneous elastic analysis is about 25 MPa (see Figure 3-3 and Section 3.3.1). Therefore, the VTM was calibrated against the target strength envelope for this confinement range (i.e., σ'_{3max} = 25 MPa). It was shown that the use of the strain-independent CWFS model for blocks and block boundaries makes it possible to generate an s-shaped strength envelope.

In order to better understand the shape of the strength envelope for the calibrated VTM beyond the 25 MPa of confinement, additional triaxial compression tests were simulated up to a confining pressure of 60 MPa. Figure 4-25 shows that within the confining range of 25 MPa and up to approximately 45 MPa, the VTM follows the tri-linear strength

envelope. This non-linear behavior, similar to that of s-shaped failure criterion proposed by Diederichs (1999) allows for capturing the transition in the failure mode from axial splitting to shear failure with increasing confinement (see Section 4.4.2 and Figure 4-18). However, beyond a confining pressure of 45 MPa, the VTM tends to overestimate the tri-linear strength envelope. Therefore, further investigation is recommended to improve model calibration and better understand the behavior of the VTM at high confinements.
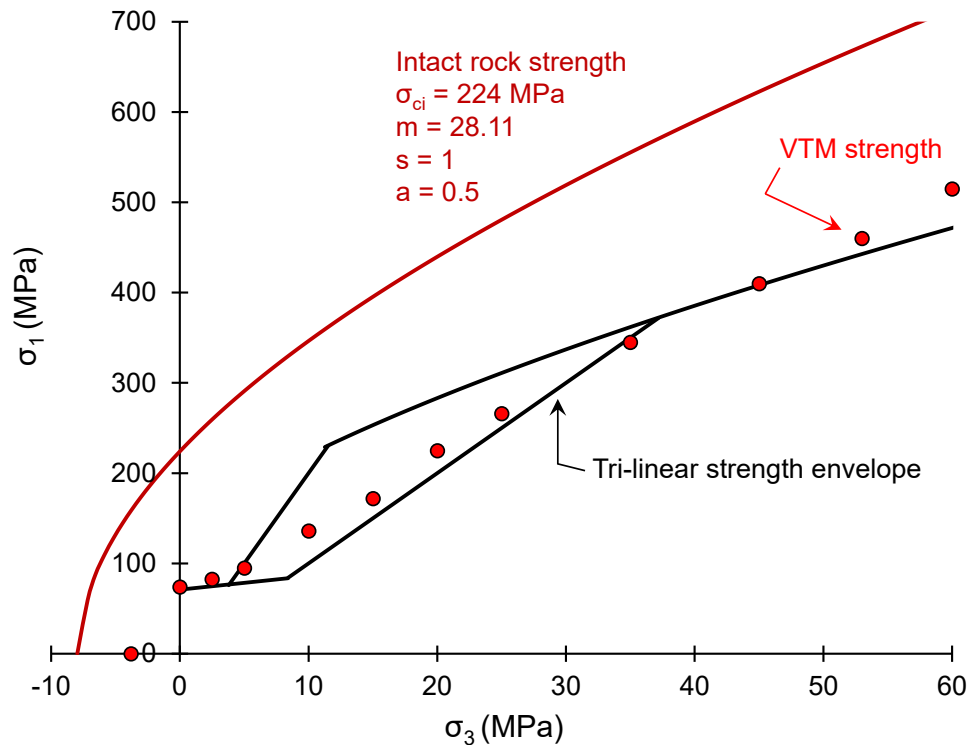
Figure 4-25 Strength envelope of intact LdB granite obtained from laboratory tests, tri-linear strength envelopes of LdB granite and peak strengths of VTM calibrated to tri-linear strength envelope up to a confining pressure of 60 MPa

4.7 Summary

In this chapter, an RS2-VTM was used to capture the v-shaped notch formation and EDZ around the MBE tunnel at the 420 m Level of the URL. To this end, the rock mass strength was estimated using two approaches: 1) tri-linear's equivalent HB (rock mass) strength envelope; and 2) tri-linear strength envelope. Systematic calibration procedures for each method were proposed.

By simulating standard rock mechanics laboratory tests including the BTS and DTS, unconfined and confined compression tests, the VTM was calibrated against the two target strength envelopes. The micro-properties of the calibrated models were then used to simulate the failure and damaged zone around the MBE tunnel.

It was found that the VTM calibrated to the equivalent rock mass strength envelope underestimates the DoF, although it captures the EDZ. However, the VTM calibrated to the tri-linear strength envelope captures the DoF, SoF and EDZ around the MBE tunnel. Furthermore, the failure mechanism captured by the VTM is realistic and consistent with other advance numerical modeling approaches and field observations, i.e., tensile yielding near the tunnel wall and shear yielding away from the tunnel boundary near the notch tip where the confinement is relatively high.

The emergent strength envelope of the VTM calibrated to the tri-linear envelope was found to be similar to the s-shaped criterion proposed by Diederichs (2003). The non-linearity of this strength envelope is due to the use of strain independent CWFS constitutive law used for both blocks and block boundaries. The VTM strength envelope follows the crack initiation threshold of the intact rock at low confinement ($\sigma_3 < 5$ MPa) and the spalling limit ($\sigma_{1/}\sigma_3 = 10 - 20$ MPa) at high confinement.

A series of sensitivity analyses were conducted on two adjusted block parameters of the VTM calibrated to the tri-linear strength envelope. For this purpose, the effects of peak block friction angle and residual block cohesion on the emergent strength envelope and the depth, shape and extent of failure around the MBE tunnel were investigated. It was found that the peak block friction angle mainly controls the VTM strength envelope at low confinement ($\sigma_3 < 5$ MPa) and directly affects the DoF and SoF around the tunnel. The sensitivity analysis on the residual block cohesion indicated that the emergent strength envelope for the entire range of confinement in addition to the DoF and SoF around the tunnel are sensitive to this parameter.

Chapter 5 Summary, Conclusions and Recommendations

5.1   Summary

In this research, a 2D heterogeneous model, called Voronoi Tessellated Model (VTM), was developed using the finite element program RS2 to simulate the behavior of Lac du Bonnet (LdB) granite under laboratory and field-scale loading conditions. The VTM was primarily developed to implement geometrical heterogeneities (i.e., grains and grain boundaries) of a crystalline rock into a continuum model. LdB granite was chosen for numerical simulations, as this granite has been extensively studied by numerous researchers and sufficient data on its behavior at different scales and under different loading conditions is available.

Brittle rock failure is a progression of events, including crack initiation, accumulation, propagation, coalescence and rupture. Reviewing previous numerical simulations of LdB granite in Chapter 2 reveals that the implementation of heterogeneities into numerical models leads to a more realistic simulation of these processes compared to conventional continuum models in which rock is considered as a homogenous material.

In Chapter 3, using the built-in discrete fracture network generator in RS2, a VTM was developed to simulate Canada's Mine-By Experiment (MBE) tunnel at the 420 m Level of the Underground Research Laboratory (URL). Disk- and a rectangular-shaped numerical specimens were 'carved' from the larger, heterogeneous domain of the MBE tunnel model. The disk-shaped VTM was used to simulate the Brazilian tensile test and the rectangular-shaped VTM was used to simulate the direct tensile, unconfined and confined compression tests. In these simulations, displacement boundaries were used to load the specimens. The VTM was calibrated against the laboratory properties of intact (undamaged) LdB granite through a systematic calibration process. The calibrated VTM was then used to simulate the MBE tunnel.

In Chapter 4, the rock mass strength was first estimated and then used as a target to calibrate the VTM and capture the failure and damage zone around the MBE tunnel. To

this end, the tri-linear and corresponding equivalent HB (rock mass) strength envelopes were established for LdB granite. After model calibration and the simulation of the v-shaped notch failure, a series of sensitivity analyses were conducted on selected VTM micro-properties to better understand their influence on the shape of the strength envelope as well as the depth, shape and extent of failure around the test tunnel.

5.2   Conclusions

Spalling, which leads to the formation of v-shaped notch failure in the vicinity of tunnel walls, is usually associated with tensile mechanisms. It was shown and discussed in Chapter 2 that even the homogeneous continuum models that capture the v-shaped notch failure (e.g., DISL and CWFS models) do not replicate the complete brittle failure process, including crack initiation and propagation, and the failure mode captured by these models is solely in shear. Therefore, based on the review of previous work and the results of research presented in this document, it is concluded that integrating geometrical heterogeneities into the continuum models is necessary to capture the brittle failure process and overall failure mode various loading conditions.

In Chapter 3, before simulating the MBE tunnel via the VTM, a homogeneous elastic model of this tunnel was constructed. In this model, the progressive detachment of rock slabs observed in the field was simulated by manually 'excavating' them in RS2. It should be noted that similar studies have been conducted by Martin (1997), who used the factor of safety as an indicator of failure around the tunnel. In this study, the progressive changes in the distribution of σ_1 and σ_3 were monitored near the tunnel. It was found that after each round of slab removal, the magnitudes of σ_3 and σ_1 gradually increase. A rapid increase in σ_3 was observed after the final geometry of the v-shaped notch was formed. It is concluded that this sudden increase in σ_3 inhibited the propagation of fractures observed above the notch tip.

In order to reduce the complexity of the calibration process in discontinuum models (e.g., UDEC-GBM), blocks are usually assumed to be elastic. In such models, blocks can detach when block boundaries fail, resulting in the redistribution of stresses (e.g., stress drop).

Markus (2019) found that RS2-VTMs with elastic blocks do not result in a stress drop in the post-peak region. This is attributed to the fact that the detachment of blocks due to block boundary yielding does not occur in RS2-VTMs. Therefore, in this research, the RS2-VTM was constructed with inelastic blocks to simulate standard rock mechanics laboratory tests and the failure around the MBE tunnel. It is concluded from the results presented in Chapters 3 and 4 that realistic simulations of failure modes and post-peak response (i.e., stress drop) in RS2-VTMs can be achieved only when the blocks are assigned inelastic properties.

In the simulations of the BTS and DTS tests, block boundary yielding initiated at approximately 80% of the peak stress, which was followed by a sudden tensile yielding of the blocks causing a rapid stress-drop in the post-peak region. In the UCS test simulations, vertical and sub-vertical block boundary yielding initiated at around 30% of the peak stress. The general mode of failure was found to be axial splitting due to the pattern of block yielded elements which were mostly in tension. Numerical simulations of the confined compression tests demonstrated a transition from axial splitting to shear failure with increasing confinement; the dominant failure mode was tensile yielding at low confinement (i.e., $\sigma_3 < 5$ MPa), a combination of tensile and shear yielding at medium confinement (i.e., $\sigma_3 = 5$ to 10 MPa), and solely shear yielding at high confinement (i.e., $\sigma_3 > 15$ MPa). It is concluded the VTM is properly calibrated, as its stress-strain curves, including the post-peak response, and the simulated failure modes of different laboratory tests, are comparable with those of LdB granite.

As described above, block boundary yielding in the BTS, DTS, UCS and confined compression tests initiated at early loading stages prior to the peak stress. By monitoring the stress-strain curves obtained from each test, it was observed that block boundary yielding does not affect the stress-strain curve, whereas block yielding results in a sudden drop in the stress level in the post-peak region. Hence, block and block boundary yielding in RS2 are indications of failure and damage, respectively. This was further investigated by monitoring the stress changes around the MBE tunnel. It was observed that block boundary yielding does not significantly redistribute σ_1 and σ_3 around the tunnel.

However, once the blocks start to yield, both σ_1 and σ_3 experience a drop in their magnitudes. It is concluded from this finding that in RS2-VTM, block boundary yielding should be considered as damage, while block yielding should be treated as an indication for failure.

The MBE tunnel has been simulated by various researchers using different numerical methods, including homogeneous and heterogeneous, continuum, discontinuum and hybrid models. From the review of the past attempts to simulate the v-shaped notch failure and EDZ around this tunnel (Chapter 2), it is concluded that regardless of the numerical method, the DoF around the MBE tunnel is underestimated if the model is calibrated to the intact rock strength (i.e., UCS ≥ 200 MPa). Furthermore, it was demonstrated in Chapter 3 that the RS2-VTM calibrated to the laboratory properties of intact rock does not adequately simulate the v-shaped notch failure. The calibrated VTM only showed random block and block boundary yielding around the tunnel, which, as discussed above, is an indication of damage. Nonetheless, the extent of EDZ was partially captured due to the presence of heterogeneities, which led to the generation of localized tensile stresses around the tunnel and, therefore, sparse block boundary yielding. Therefore, from the results of previous research and those presented in Chapter 3, it is concluded that the in situ rock mass strength needs to be first estimated and then used as a target for model calibration to realistically capture the depth and shape of failure around the MBE tunnel.

In Chapter 4, the tri-linear's equivalent HB (rock mass) strength envelope was developed for LdB granite based on the approach proposed by Bewick et al. (2019). First, an inelastic homogeneous model of the MBE tunnel was constructed in RS2. Since the post-peak response of the proposed rock mass strength envelope is not known, four scenarios for the residual strength were considered; residual strength equals 100%, 75%, 50% and 25% of the peak strength. None of these homogeneous models could adequately capture the observed shape nor the depth of failure. Furthermore, the mode of yielded elements was found to be shear. Next, the VTM was calibrated to the equivalent rock mass strength envelope. The MBE tunnel was then simulated, and the results were compared to the

field observations. It is concluded from the simulation results that the VTM calibrated to the equivalent rock mass failure envelope underpredicts the DoF but overestimates the lateral extent of failure. Nonetheless, the extent of the EDZ is well captured when compared to the location of micro-seismic events recorded in the field.

The VTM was also calibrated to the tri-linear (or s-shaped) strength envelope. It was concluded that in order for the VTM to conform to a characteristic s-shaped strength envelope, the input parameters need to follow a strain-independent CWFS behavior (i.e., instantaneous transition from peak to residual). It is concluded from the simulation results that the VTM calibrated to the tri-linear failure envelope adequately captures the DoF, SoF and EDZ around the MBE tunnel. An advantage of this modeling approach over conventional continuum approaches (e.g., CWFS and DISL) is that not only it adequately simulates the v-shaped notch failure, but it also captures realistic failure mechanisms including the transition from tensile to shear failure with increasing distance from the excavation boundary (i.e., increasing confinement).

Throughout the calibration process, it was found that two block micro-properties (i.e., peak friction angle and residual cohesion) mainly affect the shape of the emergent strength envelope and the depth and shape of failure around the MBE tunnel. From the results of sensitivity analysis, it is concluded that the peak block friction angle controls the emergent VTM strength at low confinement (σ_3 < 5 MPa). However, it does not affect the strength at higher confinements (5 MPa < σ_3 < 25 MPa). Nonetheless, both the DoF and SoF around the tunnel are affected by this micro-property. The residual block cohesion was found to affect the shape of the strength envelope for the entire range of confinement, especially for σ_3 > 5 MPa and the depth and shape of failure around the tunnel.

The results of this research support the earlier work by Li and Bahrani (2021a and b), who suggested that RS2-VTM can be used as a powerful tool to simulate the behavior of brittle rocks at different scales and under various loading conditions. An important finding in the research presented in this document is that various shapes of rock mass strength envelope (e.g., non-linear and s-shaped) can be captured by the RS2-VTM with linear peak

and residual strength envelopes for blocks and block boundaries. This further suggests that RS2-VTM, when properly calibrated, can be used as a design tool for a wide range of applications, such as tunnels, pillars and slopes. Furthermore, RS2-VTM, with the approach presented in Chapter 4, can be used to back-calculate the strength of massive to moderately jointed rock masses around underground openings and the magnitude of in situ stresses from the depth and shape of breakouts in deep boreholes. However, determining the spalling limit in the s-shaped failure criterion, which is essential for both applications, remains a challenge and therefore deserves further research.

5.3   Recommendations for Future Work

As discussed in Chapter 4, the VTM calibrated to the tri-linear strength envelope overestimated the strength at high confinement (σ_3 > 45 MPa). This can be attributed to the fact that the linear Mohr-Coulomb strength envelope was used for both blocks and block boundaries. The non-linear HB envelope could potentially be used for blocks instead of the linear Mohr-Coulomb criterion in order to match the target strength envelope at high confinement, where the third component of the tri-linear strength envelope (i.e., long-term strength) dominates the behavior.

The confinement around underground excavations such as tunnels is relatively low ($\sigma_3 \leq$ 25 MPa). It was shown that for such applications, the VTM calibrated to the tri-linear strength envelope can realistically simulate field observations (i.e., v-shaped notch failure). However, it is not known how this approach could impact the design of wide pillars at great depths where the confinement at the pillar core is relatively high ($\sigma_3 \gg 25$ MPa). Thus, it is recommended that future research would be focused on the application of the proposed VTM to high confinement problems, such as wide pillars with width-to-height ratios greater than 2.

The influence of 3D stress paths on the DoF has been studied by various researchers as reviewed in Chapter 2. It was discussed that 2D models compromise the potential effects of 3D stress changes ahead of an advancing tunnel on rock mass weakening. An underground excavation is indeed a 3D problem. Therefore, it is recommended that

further simulations of DoF around MBE tunnel would be carried out using a 3D continuum-based VTM (e.g., RS3-VTM). The capabilities of the continuum-based VTM documented in this thesis, in addition to the realistic redistribution of 3D stresses might lead to a better representation of the brittle failure process around the MBE tunnel.

A common assumption when simulating underground excavations is to disregard the excavation-induced irregularities, which was the case throughout this research. The literature shows that using the intact rock strength leads to the underestimation of DoF around the MBE tunnel and in order to adequately capture the failure as observed in the field, the UCS of the rock needs to be reduced to around its crack initiation threshold (i.e., 71 MPa for LdB granite) for the yielding to initiate. However, Cai and Kaiser (2014) were able to capture the v-shaped notch failure around the MBE tunnel using a homogenous continuum model with 'as-built' wall geometry and the long-term strength of LdB granite (i.e., 175 MPa) as the rock mass UCS. They discussed that by considering the tunnel boundary irregularities caused by the excavation method, the UCS of the rock mass can be as high as the crack damage threshold of intact rock. It is recommended that the tunnel wall irregularities would be integrated into the VTM around the MBE tunnel boundary. It is speculated that by using the VTM with tunnel wall irregularities, the failure could be simulated with a rock mass UCS close to that of intact LdB granite obtained from laboratory tests (i.e., UCS ≥ 200 MPa).

Predicting the bulking-induced displacement due to brittle failure around tunnels is important for ground support system design. Investigating the bulking-induced displacement around the MBE tunnel was beyond the scope of this research. It is recommended that the displacement simulated by the VTM could be investigated and compared to analytical and empirical methods as well as more advanced numerical models such as the DEM. For this purpose, the influence of block dilation angle and residual Young's modulus on bulking-induced displacements could be investigated with the calibrated VTM.

The systematic calibration procedures proposed in this research reduce the amount of time needed to calibrate the VTMs to target strength envelopes. The sensitivity analyses

presented in Chapter 4 were specifically focused on the influence of selected block properties on the shape of the strength envelope and the DoF around the MBE tunnel (i.e., peak block friction angle and residual block cohesion). It is recommended that systematic sensitivity analyses should be conducted to investigate the influence of different micro-properties on the emergent strength envelope, the DoF, SoF, EDZ, failure modes and displacements around excavations.

References

Azocar KD. 2016. Investigation the mesh dependency and upscaling of 3D grain-based model for the simulation of brittle fracture process in los-porosity crystalline rock. MASc thesis, Queen's University.

Bahrani N. & Hadjigeorgiou J. 2018. Influence of stope excavation on drift convergence and support behavior: insights from 3D continuum and discontinuum models. *Rock Mechanics and Rock Engineering*, 51 (8): 2395-2413.

Bahrani N. & Kaiser PK. 2013. Strength degradation of non-persistently jointed rockmass. *International Journal of Rock Mechanics and Mining Sciences*, 62: 28-33.

Bahrani N. & Kaiser PK. 2017. Estimation of confined peak strength of crack-damaged rocks. *Rock Mechanics and Rock Engineering*, 50 (2): 309–326.

Bahrani N. Kaiser PK. & Valley B. 2014. Distinct element method simulation of an analogue for a highly interlocked, non-persistently jointed rockmass. *International Journal of Rock Mechanics and Mining Sciences*, 71: 117-130.

Bahrani N. Valley B. & Kaiser PK. 2019. Influence of stress path on stress memory and stress fracturing in brittle rocks. *Canadian Geotechnical Journal*, 56 (6): 852-867.

Bewick R, Valley B, Kaiser P. 2012. Effect of grain scale geometric heterogeneity on tensile stress generation in rock loaded in compression. In: *46th US Rock mechanics/geomechanics symposium. American Rock Mechanics Association*.

Bewick RP. Kaiser PK. & Amann F. 2019. Strength of massive to moderately jointed hard rock masses. *Journal of Rock Mechanics and Geotechnical Engineering*, 11: 562-575.

Bieniawski ZT. 1967. Mechanism of brittle fracture of rock, part II - fracture in tension and under long-term. *International Journal of Rock Mechanics and Mining Sciences & Geomechanics Abstracts*, 4 (4): 425e6.

Bobet A. Fakhimi A. Johnson S. Morris J. Tonon F. & Ronal Yeung. 2009. Numerical Models in Discontinuous Media: Review of Advances for Rock Mechanics Applications. *Journal of Geotechnical and Geoenvironmental Engineering*, 135 (11): 1547-1561.

Brady BGH. & Brown ET. 2006. Rock Mechanics for Underground Mining. Third edition, Springer.

Cai M. & Kaiser PK. 2014. In-situ rock spalling strength near excavation boundaries. *Rock Mechanics and Rock Engineering*, 47 (2): 659-675.

Cai M. Kaiser PK. Tasaka Y. Maejima T. Morioka H. & Minami M. 2004. Generalized crack initiation and crack damage stress thresholds of brittle rock masses near underground excavations. *International Journal of Rock Mechanics and Mining Sciences*, 41(5): 833-847.

Chandler NA. 2003. Twenty years of underground research at Canada's URL. *Waste Management, Energy Security and a Clean Environment*, Tucson, Arizona.

Dadashzadeh N. 2020. Reliability of stress induced damage predictions in hard rocks with continuum and discontinuum numerical modelling approaches. PhD thesis, Queen's University, Ontario, Canada.

Diederichs MS. 2003. Rock fracture and collapse under low confinement conditions. *Rock Mechanics and Rock Engineering,* 36 (5): 339-381.

Diederichs MS. 1999. Instability of hard rockmasses, the role of tensile damage and relaxation. PhD thesis, University of Waterloo.

Diederichs MS. 2007. The 2003 Canadian Geotechnical Colloquium: Mechanistic interpretation and practical application of damage and spalling prediction criteria for deep tunnelling. *Canadian Geotechnical Journal,* 44: 1082-1126.

Eberhardt E. Stead D. Stimpson B. & Read RS. 1997. Identifying crack initiation and propagation thresholds in brittle rock. *Canadian Geotechnical Journal*, 35 (2): 222-233.

Everitt R. McMurray J. Brown A. & Davison D. 1996. Geology of the Lac du Bonnet batholith, inside and out: AECK's Underground Research Laboratory, Southeastern Manitoba – Field Trip Guidebook B5; *Geological Association of Canada/Mineralogical Association of Canada Annual Meeting*, Winnipeg, Manitoba.

Everitt RA. & Lajtai EZ. 2004. The influence of rock fabric on excavation damage in the Lac de Bonnet granite. *International Journal of Rock Mechanics & Mining Sciences*, 41: 1277–1303.

Fang Z. Harrison JP. 2002. Application of a local degradation model to the analysis of brittle fracture of laboratory scale rock specimens under triaxial conditions. *International Journal of Rock Mechanics and Mining Sciences*, 39 (4): 459-476.

Fang Z. Harrison JP. 2003. Numerical analysis of progressive fracture and associated behaviour of mine pillars by use of a local degradation model. *International Journal of Rock Mechanics and Mining Sciences,* 111 (1): 59-72.

Gao F. Stead D. & Elmo D. 2016. Numerical simulation of microstructure of brittle rock using a grain-breakable distinct element grain-based model. *Computers and Geotechnics*, 78: 203-217.

Gao FQ. & Stead D. 2014. The application of a modified Voronoi logic to brittle fracture modelling at the laboratory and field scale. *International Journal of Rock Mechanics and Mining Science*, 68: 1–14.

Geomechanica Inc. 2017. Irazu 2D Geomechanical Simulation Software, version 3.0.

Ghazvinian E. 2015. Fracture Initiation and Propagation in Low Porosity Crystalline Rocks: Implications for Excavation Damage Zone (EDZ) Mechanics. PhD thesis, Queen's University.

Ghazvinian E. Diederichs MS. & Quey R. 2014. 3D random Voronoi grain-based models for simulation of brittle rock damage and fabric-guided micro-fracturing. *Journal of Rock Mechanics and Geotechnical Engineering*, 6: 506-521.

Hajiabdolmajid V. Kaiser PK. & Martin CD. 2002. Modeling brittle failure of rock. *International Journal of Rock Mechanics and Mining Science*s, 39: 731-741.

Hazzard JF. & Young RP. 2004. Dynamic modelling of induced seismicity. International *Journal of Rock Mechanics and Mining Science*, 41: 1365-1376.

Hoek E. & Brown ET. 1980. Empirical strength criterion for rock masses. *Journal of Geotechnical and Environmental Engineering*, 106: 1013-1035.

Hoek E. & Brown ET. 1997. Practical estimates of rock mass strength. *International Journal of Rock Mechanics and Mining Sciences and Geomechanics Abstracts*; 34 (8): 1165-1186.

Hoek E. & Brown ET. 2019. The Hoek-Brown failure criterion and GSI - 2018 edition. *Journal of Rock Mechanics and Geotechnical Engineering*, 11 (3): 445-463.

Hoek E. & Diederichs MS. 2006. Empirical estimation of rock mass modulus. *International Journal of Rock Mechanics & Mining Sciences,* 43: 203-215.

Hoek E. Carranza-Torres C. & Corkum B. 2002. Hoek-Brown criterion edition. In: Hammah R, Bawden W, Curran J, Telesnicki M, editors. *Mining and tunnelling innovation and opportunity, proceedings of the 5th North American rock mechanics symposium and 17th tunnelling association of Canada conference*. Toronto, Canada. Toronto: University of Toronto, 267-273.

Hoek E. Grabinsky MW. & Diederichs MS. 1991. Numerical modelling for underground excavation design. Trans. *Instn. Min. Metall*. (Sect. A: Min. Industry): A22-A30.

Hoek E. Kaiser. P & Bawden WF. 1995. Support of underground excavations in hark rock. Rotterdam, Netherlands: A.A. Balkema.

Homand-Etienne F. Hoxha D. & Shao JF. A continuum damage constitutive law for brittle rocks. *Computers and Geotechnics*, 22 :135–151.

ISRM 1979. Suggested methods for determining the uniaxial compressive strength and deformability of rock materials, *International Journal of Rock Mechanics and Mining Sciences*. 16 (2): 135-140.

Itasca Consulting Group Inc. 1995. PFC (Particle Flow Code), Version 1.0. Minneapolis, Minnesota.

Itasca Consulting Group Inc. 1996. UDEC (Universal Distinct Element Code), version 4.0. Minneapolis, Minnesota.

Itasca Consulting Group Inc. 1999. PFC2D/3D (Particle Flow Code in 2/3 Dimensions), Version 2.0. Minneapolis, Minnesota.

Itasca Consulting Group Inc. 2000. FLAC (Fast Lagrangian Analysis of Continua), Minneapolis, Minnesota.

Itasca Consulting Group Inc. 2009. FLAC3D (Fast Lagrangian Analysis of Continua in 3 Dimensions), Version 4.00. Minneapolis, Minnesota.

Itasca Consulting Group Inc. 2014. UDEC (Universal Distinct Element Code), Version 6.0. Minneapolis, Minnesota.

Jing L. & Hudson JA. 2002. Numerical methods in rock mechanics. *International Journal of Rock Mechanics and Mining Sciences*, 39: 409–427.

Kaiser PK. & Kim B. 2014. Characterization of strength of intact brittle rock considering confinement-dependent failure processes. *Rock Mechanics and Rock Engineering*, 48 (1): 107-119.

Kaiser PK. Diederichs MS. Martin CD. Sharp J. & Steiner W. Underground works in hard rock tunnelling and mining. Keynote lecture in proceedings of GeoEng2000, Melbourne, 841-926.

Kirsch 1898. Die Theorie der Elastizität und die Bedürfnisse der Festigkeitslehre. Zeitschrift des Vereines deutscher Ingenieure, 42: 797-807.

Lan H. Martin CD. & Hu B. 2010. Effect of heterogeneity of brittle rock on micromechanical extensile behavior during compression loading. *Journal of Geophysics Research,* 115: B01202.

Li X. Kim E. & Walton G. 2019. A study of rock pillar behaviors in laboratory and in-situ scales using combined finite-discrete element method models. *International Journal of Rock Mechanics and Mining Sciences*, 118: 21-32.

Li Y. & Bahrani N. 2021a. A continuum grain-based model for intact and granulated Wombeyan marble. *Computers and Geotechnics,* 129: 103872.

Li Y. & Bahrani N. 2021b. Strength and failure mechanism of highly interlocked jointed pillars: insight from upscaled continuum grain-based models of a jointed rock mass analogue. *Computers and Geotechnics,* 137: 104278.

Marinos P. & Hoek E. 2000. The Geological Strength Index (GSI): A characterization tool for assessing engineering properties of rock masses. *International Conference on Geotechnical and Geological Engineering*, Melbourne, 1422-1446.

Markus S. 2019. A stepwise approach to verification of the combined finite-discrete element method for modelling instability around tunnels in brittle rock. MASc thesis, Queen's University.

Martin CD. & Chandler NA. 1994. The progressive fracture of Lac Du Bonnet granite. *International Journal of Rock Mechanics and Mining Sciences and Geomechanics Abstracts*, 31 (6): 643-659.

Martin CD. 1990. Characterizing in situ stress domains at the AECL Underground Research Laboratory. *Canadian Geotechnical Journal*, 27 (5): 631-646.

Martin CD. 1993. Strength of massive Lac du Bonnet granite around underground openings. PhD thesis, University of Manitoba, Alberta.

Martin CD. 1997. The effect of cohesion loss and stress path on brittle rock strength. *Canadian Geotechnical Journal*, 34: 698-725.

Martin CD. Kaiser PK. & McCreath DR. 1999. Hoek-Brown parameters for predicting the depth of brittle failure around tunnels. *Canadian Geotechnical Journal*, 36: 136-151.

Martin CD. Read RS. & Martino JB. 1997. Observations of brittle failure around a circular test tunnel. *International Journal of Rock Mechanics and Mining Sciences*, 34 (7): 1065-1073.

Martino JB. & Chandler NA. 2004. Excavation-induced damage studies at the Underground Research Laboratory. *International Journal of Rock Mechanics and Mining Sciences,* 41 (8): 1413-1426.

Mortazavi A. & Molladavoodi H. 2012. A numerical investigation of brittle rock damage model in deep underground openings. *Engineering Fracture Mechanics,* 90: 101-120.

Ohta MM. & Chandler NA. 1997. AECL's underground research laboratory: technical achievements and lessons learned. *Atomic Energy of Canada Limited*, AECL--11760.

Pande GN. Beer G. & Williams JR. 1990. Numerical Methods in Rock Mechanics. Chichester, Wiley.

Perras M. & Diederichs M. 2016. Predicting excavation damage zone depths in brittle rocks. *Journal of Rock Mechanics and Geotechnical Engineering,* 8 (1): 60-74.

Potyondy DO. & Cundall PA. 2004. A bonded-particle model for rock. *International Journal of Rock Mechanics and Mining Science,* 41: 1329-1364.

Qi S. Lan H. Martin CD. & Huang X. 2019. Factors controlling the difference in Brazilian and direct tensile strengths of the Lac du Bonnet granite. *Rock Mechanics and Rock Engineering,* 53 (3): 1005–1019.

Rafiei Renani H. & Martin CD. 2018. Cohesion degradation and friction mobilization in brittle failure of rocks. *International Journal of Rock Mechanics and Mining Sciences,* 106: 1-13.

Read RS. & Chandler NA. 1996. AECL's excavation stability study – summary of observations. *Atomic Energy of Canada Limited,* AECL-11582, COG-96-193.

Read RS. & Martin CD. 1991. Mine-by experiment final design report. *Atomic Energy of Canada Limited,* AECL--10430.

Read RS. & Martin CD. 1996. Technical summery of AECL's Mine-by Experiment phase 1: excavation response. AECL-11311, COG-95-171.

Read RS. 1994. Interpreting excavation-induced displacements around a tunnel in highly stressed granite. Ph.D. thesis, University of Manitoba.

Read RS. 2004. 20 years of excavation response studies at AECL's Underground Research Laboratory. *International Journal of Rock Mechanics and Mining Sciences,* 41 (8): 1251-1275.

Read RS. Chandler NA. & Dzik EJ. 1998. In situ strength criteria for tunnel design in highly stressed rock masses. *International Journal of Rock Mechanics and Mining Sciences*, 35 (3): 261-278.

Riahi A. Hammah ER. & Curran JH. 2010. Limits of applicability of the finite element explicit joint model in the analysis of jointed rock problems. 44th US Rock Mechanics Symposium - 5th US/Canada Rock Mechanics Symposium.

Rocscience. 2005. Phase^2. Version 6.001. 2-dimensional elasto-plastic finite element program.

Rocscience. 2021. RS2 v. 11.008.

Shin SW. 2010. Excavation disturbed zone in Lac Du Bonnet granite. PhD thesis, University of Alberta.

Sinha S. & Walton G. 2020. A study on Bonded Block Model (BBM) complexity for simulation of laboratory-scale stress-strain behavior in granitic rocks. *Computers and Geotechnics*, 118: 103363.

Tang CA. & Kaiser PK. 1998. Numerical simulation of cumulative damage and seismic energy release during brittle rock failure—Part I: Fundamentals. *International Journal of Rock Mechanics and Mining Sciences,* 35: 113–121.

Tatone BSA. & Grasselli G. 2015. A calibration procedure for two-dimensional laboratoryscale hybrid finite–discrete element simulations. *International Journal of Rock Mechanics and Mining Sciences,* 75: 56–72.

Tsang C. Bernier F. & Davies C. 2005. Geohydromechanical processes in the excavation damaged zone in crystalline rock, rock salt, and indurated and plastic clays - in the context of radioactive waste disposal. *International Journal of Rock Mechanics and Mining Science*, 42: 109-125.

Valley B. Suorineni FT. & Kaiser PK. 2010. Numerical analyses of the effect of heterogeneities on rock failure process. *American Rock Mechanics Association, 44th US Rock Mechanics Symposium and 5th U.S.-Canada Rock Mechanics Symposium*, Salt Lake City.

Vazaios N. Vlachopoulos N. & Diederichs MS. 2019. The Mechanical Analysis and Interpretation of the EDZ Formation around Deep Tunnels within Massive Rockmasses Using a Hybrid Finite-Discrete Element Approach: The case of the AECL URL Test Tunnel. *Canadian Geotechnical Journal*, 56 (6): 852-867.

Vlachopoulos N. & Diederichs MS. 2014. Appropriate uses and practical limitations of 2D numerical analysis of tunnels and tunnel support response. *Geotechnical and Geological Engineering,* 32 (2): 469-488.

Wang QZ. Jia XM. Kou SQ. Zhang ZX. & Lindqvist PA. 2004. The flattened Brazilian disc specimen used for testing elastic modulus, tensile strength and fracture toughness of brittle rocks: analytical and numerical results. *International Journal of Rock Mechanics and Mining Sciences*, 41: 245–253.

Wang X. & Cai M. 2018. Modeling of brittle rock failure considering inter- and intra-grain contact failures. *Computers and Geotechnics*, 101: 224-244.